

NATIONAL & INTERNATIONAL SCIENTIFIC EVENTS

IEEE 40th International Conference on Consumer Electronics

Venue: Tuscany Suites and Casino
Location: Las Vegas, USA

Begins: January 07, 2022
Ends: January 09, 2022

12nd International Conference on Power Energy and Electrical Engineering (CPEEE 2022)

Venue: Biwako-Kusatsu Campus of Ritsumeikan University
Location: Shiga, Japan

Begins: February 25, 2022
Ends: February 27, 2022

16th European Conference on Antennas and Propagation (EuCAP 2022)

Venue: IFEMA Palacio Municipal
Location: Madrid, Spain

Begins: March 27, 2022
Ends: April 01, 2022

20th International Conference on Soil Mechanics and Geotechnical Engineering (ICSMGE 2022)

Venue: International Convention Centre Sydney
Location: Sydney, Australia

Begins: May 01, 2022
Ends: May 05, 2022

8th European Congress on Computational Methods in Applied Sciences and Engineering

Venue: Norway Convention Center
Location: Oslo, Norway

Begins: June 05, 2022
Ends: June 09, 2022

The 75th IIW Annual Assembly and International Conference

Venue: Grand Nikko Tokyo Daiba
Location: Tokyo, Japan

Begins: July 17, 2022
Ends: July 22, 2022

The 35th International Conference on Micro Electro Mechanical Systems

Venue: Tokyo International Forum
Location: Tokyo, Japan

Begins: January 09, 2022
Ends: January 13, 2022

16th International Conference on Martensitic Transformation (ICOMAT 2022)

Venue: Ramada Plaza Jeju Hotel
Location: Jeju, Korea

Begins: March 13, 2022
Ends: March 18, 2022

27th International Conference on Database Systems for Advanced Applications (DASFAA-2022)

Venue: Online Conference
Location: Hyderabad, India

Begins: April 11, 2022
Ends: April 14, 2022

The 31st IEEE International Symposium on Industrial Electronics (IEEE ISIE 2022)

Venue: Dena'ina Center/Egan Center
Location: Alaska, USA

Begins: June 01, 2022
Ends: June 03, 2022

39th IAHR World Congress

Venue: IAHR World Congress
Location: Granada, Spain

Begins: June 19, 2022
Ends: June 24, 2022

26th International Conference on Pattern Recognition

Venue: Palais des congrès de Montréal
Location: Montréal, Canada

Begins: August 21, 2022
Ends: August 25, 2022



Abstracted & Indexed in:

TR Dizin Mühendislik ve Temel Bilimler Veri Tabanı | CrossRef | Google Scholar | MIP Database | StuartxChange | ResearchBib | Scientific Indexing Services (SIS)

HITIT
UNIVERSITY

HITTITE

JOURNAL OF SCIENCE & ENGINEERING

HJSE Official Journal of Hitit University Volume 8, Issue 4, 2021 dergipark.org.tr/en/pub/hjse



HJSE Official Journal of Hitit University Volume 8, Issue 4, 2021 dergipark.org.tr/en/pub/hjse

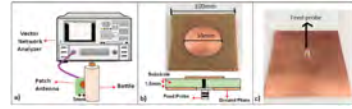
Volume 8, Issue 4, 2021

dergipark.org.tr/en/pub/hjse

A New Approach for Liquid Scanners to Determine Flammable Liquid Concentration in Solutions 279-285

Ebru Efeoglu and Gurkan Tuna

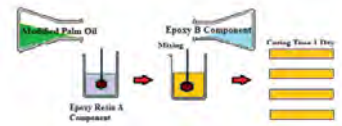
In this study, a machine learning based liquid control system that can be used in airports, railway stations and shopping malls as well as in places with high fire probability is proposed.



Production and Characterization of Palm Oil Based Epoxy Biocomposite by RSM Design 287-297

Hakan Sahal and Ercan Aydogmus

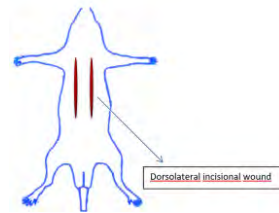
In this research, some physical and chemical properties of the biocomposite obtained from synthesized epoxy modified palm oil (MPO) and epoxy resin have been characterized.



Effect of Fibroblast Growth Factor (FGF) on Some Serum Oxidative Parameters in Hyperglycemic Rats 299-305

Esra Oguz and Sule Coskun Cevher

In the present study, we aimed to investigate exogenous effect bFGF supplementation on serum TBARS, RSH and NOx levels in hyperglycemic rats.



Evaluation of the Cytotoxic Effects of Ultrasonic Extracts of Tribulus Terrestris L. on MCF-7 Cell Line by MTT Assay 307-312

Giray Bugra Akbaba, Fureya Elif Ozturkkan and Mustafa Sertcelik

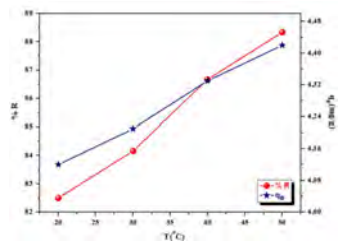
In this study, ethanol, ethyl acetate and methanol extracts of Tribulus terrestris L. plant, which is used by local people as one of these medicinal plants in Kars province (Turkey), were obtained by ultrasound assisted extraction method.



Bioadsorbent Efficiency in Heavy Metal Removal from Aqueous Solutions: Adsorption Kinetics, Isotherm, and Thermodynamics 313-320

Cigdem Oter

This study aimed to remove Hg (II) ions from wastewater by using ground rice grains as adsorbents.



Computational Analysis Of Potential Key Genes Associated With Dopamine Neurotransmission In Pheochromocytoma And Paraganglioma 321-328

Orcun Avsar

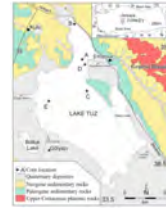
In the present study, it was determined that COMT gene was significantly less expressed in LPCPG than in normal tissue and COMT gene showed a remarkable relationship between differential expression with shorter overall survival among the individuals with PCPG (HR=1, p=0.011).



Mineralogy and Geochemistry of Sediments from Lake Tuz 329-338

Mehmet Yavuz Huseyinca and Suayip Kupeli

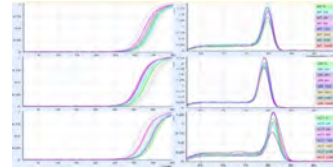
In this study, mineralogical and geochemical features of the lake sediments sampled by core drillings were investigated.



Expression analysis of Some Stress-Related Genes Induced by Cadmium on Tomato (Solanum lycopersicum L.) Plants 339-345

Ekrem Bolukbas

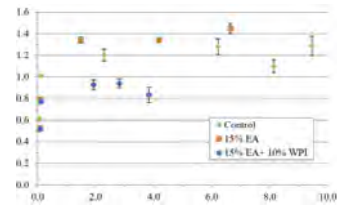
In this study, it was aimed to determine gene expression changes in tomato plant under Cd stress.



Foam-mat Drying of Carrot Juice and Thin Layer Modeling of Drying 347-354

Hulya Cakmak and Vasiye Hazal Ozyurt

In this study, the effects of foam-mat drying at 50, 60 and 70°C on the drying behavior of carrot juice with the addition of 15% egg albumen (EA) and 15% egg albumen+ 10% whey protein isolate (WPI) as foaming agents and thin-layer modeling of the foams at different thicknesses was evaluated.



Owner

Prof. Dr. Ali Osman ÖZTÜRK on
behalf of Hitit University

Editor-in-chief

Prof. Dr. Ali KILIÇARSLAN

Associate Editors

Prof. Dr. D. Ali KÖSE

Assoc. Prof. Dr. Öncü AKYILDIZ

Production

Assoc. Prof. Dr. Kazım KÖSE

Res. Asst. Dr. Erhan ÇETİN

Res. Asst. Mustafa Reşit HABOĞLU

Res. Asst. Harun Emre KIRAN

Res. Asst. Ömer Faruk TOZLU

Lect. Tugrul YILDIRIM

Editor's Office

Tel: +90 364 227 45 33 / 12 36

Fax: +90 364 227 45 35

Email: alikilicarslan@hitit.edu.tr

Subscription Service:

Tel: +90 364 227 45 33 / 12 82

Fax: +90 364 227 45 35

Email: hjse@hitit.edu.tr

EDITORIAL BOARD

Prof. Dr. İftikhar AHMAD

Prof. Dr. Mike BECKETT

Prof. Dr. İbrahim DİNÇER

Prof. Dr. Ali ELKAMEL

Prof. Dr. Mohamad S QATU

Prof. Dr. Saffa RIFFAT

Prof. Dr. Thanos SALIFOLOU

Prof. Dr. Yuehong SU

Dr. Wojciech NOGALA

Prof. Dr. Yusuf AYVAZ

Prof. Dr. Adil DENİZLİ

Prof. Dr. Ali GENÇER

Prof. Dr. Metin GÜRÜ

Prof. Dr. Murat HOŞÖZ

Prof. Dr. Sadık KAKAÇ

Prof. Dr. Tarık Ömer OĞURTANI

Prof. Dr. Ender SUVACI

Prof. Dr. Ali TOPÇU

Prof. Dr. Kazım Savaş BAHÇECİ

Prof. Dr. Cengiz BAYKASOĞLU

Prof. Dr. Naki ÇOLAK

Prof. Dr. Vedat DENİZ

Prof. Dr. Hakan GÜNGÜNEŞ

Prof. Dr. Bülent KABAK

Prof. Dr. Ali KILIÇARSLAN

Prof. Dr. Dursun Ali KÖSE

Prof. Dr. İrfan KURTBAŞ

Prof. Dr. İbrahim SÖNMEZ

Assoc. Prof. Dr. Seyfi ŞEVİK

Prof. Dr. Dilber Esra YILDIZ

University of Malakand, Chakdara, Pakistan

Bangor University, Bangor, United Kingdom

Uoit Ontario University, Ontario, Canada

University of Waterloo, Ontario, Canada

Central Michigan University, Michigan, United States

The University of Nottingham, United Kingdom

Aristotle University of Thessaloniki, Thessaloniki, Greece

The University of Nottingham, United Kingdom

Polish Academy of Sciences, Poland

Suleyman Demirel University, Turkey

Hacettepe University, Turkey

Ankara University, Turkey

Gazi University, Turkey

Kocaeli University, Turkey

TOBB University, Turkey

Middle East Technical University, Turkey

Anadolu University, Turkey

Hacettepe University, Turkey

Hitit University, Turkey

Hitit University, Turkey

Hitit University, Turkey

Hitit University, Turkey

Hitit University, Turkey

Hitit University, Turkey

Hitit University, Turkey

Hitit University, Turkey

Hitit University, Turkey

Hitit University, Turkey

Hitit University, Turkey

Hitit University, Turkey

Journal Name : HITTITE JOURNAL OF SCIENCE AND ENGINEERING
 Year : 2021
 Managing Editor : Prof. Dr. Ali KILIÇARSLAN
 Managing Office : Hitit University Faculty of Engineering
 Managing Office Tel : +90 364 227 45 33 / 12 36
 Publication Language : English
 Publication Type : Peer Reviewed, Open Access, International Journal
 Delivery Format : 4 times a year (quarterly)
 Print ISSN : 2149-2123
 Online ISSN : 2148-4171
 Publisher Address : Hitit Üniversitesi Kuzey Kampüsü Çevre Yolu Bulvarı
 19030 Çorum / TÜRKİYE
 Publisher Tel : +90 364 227 45 33/1236



This new issue of Hittite Journal of Science and Engineering contains ten manuscripts from the disciplines of chemistry, molecular biology and genetics, bioengineering, chemical engineering, computer engineering, geological engineering and food engineering. These manuscripts was first screened by Section Editors using plagiarism prevention software and then reviewed and corrected according to the reviewer's comments.

I would like to express my gratitude to all our authors and contributing reviewers of this issue. I would like to thank to the new President of Hitit University, Prof. Dr. Ali Osman Öztürk, for his

support and interest in HJSE and also to the Section Editors of HJSE, namely Prof. Dr. Dursun Ali Kose and Assoc. Prof. Dr. Oncu Akyıldız, as well as our Production Editors Assoc. Prof. Dr. Kazim Kose, Mustafa Reşit Haboğlu, Dr. Erhan Çetin, Tugrul Yıldırım, Harun Emre Kıran and Ömer Faruk Tozlu for their invaluable efforts in making of the journal.

It's my pleasure to invite the researchers and scientists from all branches of science and engineering to join us by sending their best papers for publication in Hittite Journal of Science and Engineering.

Prof. Dr. Ali Kiliçarslan

Editor-in-Chief

A New Approach for Liquid Scanners to Determine Flammable Liquid Concentration in Solutions

Ebru Efeoğlu¹  Gürkan Tuna² 

¹Kutahya Dumlupınar University, Department of Software Engineering, Kutahya, Turkey

²Trakya University, Department of Computer Programming, Edirne, Turkey

ABSTRACT

Strong liquid explosives were obtained by mixing some chemical liquids and these explosives were used in many terrorist attacks in crowded places such as airports, railway stations and shopping malls. They were also used to cause sabotage to facilities that produce, store or use hazardous chemicals in their processes. For this reason, it is very important to take the necessary measures to prevent sabotage and terrorist attacks that may occur in such places in order to ensure public and environmental safety. In this study, a machine learning based liquid control system that can be used in airports, railway stations and shopping malls as well as in places with high fire probability is proposed. The difference of the proposed system from traditional liquid scanner systems is that it can detect the hazardous liquid concentration in the solutions as well as the detection of pure flammable liquids. Linear Discriminant Analysis and Quadratic Discriminant Analysis are used as classifiers and the performances of these techniques are compared. The results show that Quadratic Discriminant Analysis offers higher accuracy and lower error rates compared to Linear Discriminant Analysis.

Keywords:

Security; Liquid classification; Scattering parameter; Linear discriminant analysis; Quadratic discriminant analysis; Accuracy; Performance metrics

INTRODUCTION

Fire pools can be formed by mixing hazardous chemical liquids; on the other hand, mixing incompatible chemicals can cause exothermic oxidation [1]. Fires involving self-incineration may accelerate depending on the nature of the first spilled liquid and its proximity to the surrounding material. Hazardous chemical reactivity events have been conducted and lessons learned from these cases as presented in [2]. In most cases, oxidisers have caused these fires to start or have contributed to the increasing coverage of the fires [3]. The mixing of incompatible liquids during the use of chemical liquids found in small containers with open covers showed that accidents and fires occurred as a result of accidental spillage and contamination [4]. Therefore, classification of liquids plays an important role in ensuring fire safety [5]. Considering this, fire and explosion hazards of some flammable liquid mixtures were estimated [6].

Most of the deaths in fires are caused by the inhalation of toxic gases produced during combustion, since it creates a complex toxic environment that includes fire, flame, heat, oxygen depletion, smoke and toxic gases [7].

Researchers have provided methods for assessing life safety hazards in fires and understanding the effects of smoke, heat and toxic fire wastes on humans [8]. The use of machine learning techniques for process safety has been heavily investigated. For example, by considering aerosolisation liquid flammability levels were predicted using machine learning techniques [9]. Performance estimation of suspension freezing crystallization was made for the treatment of hazardous liquid wastes with machine learning methods [10]. In addition, machine learning was used to predict flammability leading properties for liquid aerosol safety [11], to predict hazardous properties of chemical mixtures [12], to set a hazard index for logistics warehouses [13]. Classification of diesel and biodiesel mixtures was carried out using the electronic nose and Linear Discriminant Analysis (LDA) and Quadratic Discriminant Analysis (QDA) techniques [14]. A combustion risk index was developed for flammable liquids based on unsupervised clustering algorithms [15]. Microwave measurement method is fast and is not sensitive to environmental conditions [16] and it is generally used to determine the relative perme-

Article History:

Received: 2021/04/23

Accepted: 2021/12/04

Online: 2021/12/31

Correspondence to: Gürkan Tuna,
Department of Computer Programming,
Trakya University, Edirne, Turkey
Tel: +90 284 224 02 83
E-Mail: gurkantuna@trakya.edu.tr

ability values of liquids. Microwave measurement methods were used to measure the permeability of thin-layer materials [17] and to measure parameters of silicon [18]. Although there are many microwave measurement methods, the most frequently used one is the open-ended coaxial probe (OECF) method. In this method, liquid measurement is carried out by immersing a probe in the liquid. The complex permeability of glucose / water and water / fluoride solutions was estimated using OECF and artificial neural networks [19],[20].

In the past, X-ray safety systems were used for the detection of hazardous liquids [21] and low energy X-ray transmission technique was one of the techniques employed for this purpose [22]. As well as the low energy X-ray transmission technique, spectral droplet analysis was used for the same purpose [23]. However, since these methods cannot accurately detect some flammable liquids, in other words, the false alarm rate is high, two-stage control consisting of the combination of electronic nasal odour recognition technology and x-ray method has been proposed [24]. In this study, unlike the literature, a liquid identification system with high accuracy, fast and cheaper than other systems is proposed. This proposed system is capable of detecting even a mixture containing 10% hazardous liquid. Also, thanks to this system, unlike other systems, the hazardous liquid concentration in the mixtures can be determined. The measurement system presented in the study can analyse the liquid remotely without any intervention to the liquid and without opening the lid of the bottle / container filled with liquid, as well as measuring by immersion in the liquid.

MATERIALS AND METHODS

Discriminant Analysis Methods

In the following subsections LDA and QDA are reviewed.

LDA

LDA is a simple and useful classification technique that gives good results in solving complex problems. It performs the separation of classes by searching for the linear combination of variables. The discriminant function is the weighted average of the values of the independent variables. These weights are chosen to divide observations into groups. The discriminant function (L) is given in Eq. (1).

$$L = a_1x_1 + a_2x_2 + \dots + a_nx_n \quad (1)$$

In (1), x_1, x_2, \dots, x_n represent the variables and a_1, a_2, \dots, a_n represent the weights, model coefficients. The weights are calculated using (2).

$$a = c^{(-1)}(b_1 - b_2) \quad (2)$$

where c represents covariance matrix, b_1 and b_2 are mean vectors.

The discriminant function is obtained from previously known units of group membership, and then this function is used to determine which group will be assigned to new units with unknown group membership. Using a score function defined by the algorithm, linear coefficients that give the highest values in the function are found (3). The aggregated covariance matrix is given in (4).

$$S(a) = \frac{a^T b_1 - a^T b_2}{a^T c a} \quad (3)$$

$$c = \frac{1}{n_1 + n_2} (n_1 c_1 + n_2 c_2) \quad (4)$$

The Mahalanobis distance is used to determine the best discriminate. The probability that the algorithm has classified correctly determines the value of this distance. A value less than 3 means that the probability of correct classification is high. The Mahalanobis distance between the two groups is given in (5).

$$d^2 = a^T (b_1 - b_2) \quad (5)$$

In order to end the classification process, the condition given in (6) must be met.

$$a^T \left(x \left(\frac{b_1 + b_2}{2} \right) \right) > \log \left(\frac{P(c_1)}{P(c_2)} \right) \quad (6)$$

Here p shows class probabilities.

QDA

QDA has quadratic decision limits. Using it, data can be classified into two or more class datasets. It is generally used when the data show normal distribution and the variance-covariance matrices between groups are different. While applying this technique, it should be taken into consideration that the number of observations in each group should be more than the number of variables. The difference of QDA from LDA is that it estimates the covariance matrix for each class. The function specified in (7) is used.

$$L_k(x) = -\frac{1}{2}(x - b_k)^T c_k^{-1}(x - b_k) - \frac{1}{2} \ln |c_k| + \ln P(c_k) \quad (7)$$

where c_k is the covariance matrix for class k , c_k^{-1} is the inverse of the covariance matrix, and $|c_k|$ is the determinant of the covariance matrix, $P(c_k)$ is the previous probability of class k . Here, the aim is to find the class with the highest L value.

Experimental Setup and Methodology

The schematic representation of the single-port measurement system with the test setup is shown in Fig. 1. The arrangement consists of a 10 cm x 10 cm square-shaped antenna, vector network analyser (VNA) and 50 Ohm SubMiniature version A (SMA) coaxial cable to feed the system. Electromagnetic waves are transmitted by the transmitting antenna and reflected signals are collected after the electromagnetic radiation interacts with the liquid. These signals collected by a single-port measuring system are called scattering parameters (S11-parameter). The antenna patch was designed to be 55 mm in diameter and the antenna resonant frequency is calculated using (8) and (9). The design of the antenna was constructed on a FR4 based dielectric substrate with 1.6 mm height, 4.4 relative permittivity.

$$F = \frac{8,791 \times 10^9}{f_r \sqrt{\epsilon_r}} \quad (8)$$

$$a = \left\{ 1 + \frac{F}{\pi \epsilon_r F \left[\ln \left(\frac{\pi F}{2h} \right) + 1,7726 \right]^{1/2}} \right\} \quad (9)$$

where ϵ_r is relative permittivity of the substrate, f_r is the resonant frequency, h is the height of the substrate, a is the radius of the patch.

The implementation of this method is easy and fast. Since there is an air gap between the measured liquid and the antenna, measurements should be performed by keeping the antenna as close as possible to the liquid container in order to make more accurate measurements. Liquid measurements can be carried out in closed containers, without opening the lid, non-destructively and by approaching the container filled with liquid 4-5mm. In the study, measurements were made between 1-3 GHz and the S-parameter of each liquid in this frequency band was measured. The measurements were made at room temperature and in the same type of containers. Antenna-liquid distance was 5 mm. Flammable liquids should not be stored in the same place

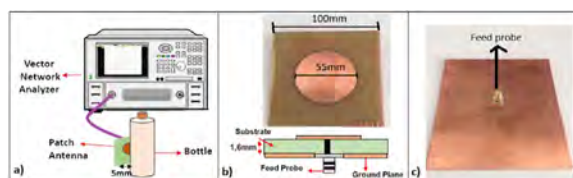


Figure 1. Experimental setup a) The measurement system b) Front view and structure of the antenna c) Back view of the antenna.

with oxidising liquids, and their mixing as a result of any impact should be prevented. Because oxidising liquids enter into exothermic reactions with flammable liquids and cause fires and explosions. For this reason, the hazardous liquid recognition system we recommend consists of 3 stages. It makes the S-parameter measurement using a liquid measurement system of unknown type and at the first stage, from this measurement, it decides whether there is a hazardous liquid such as flammable or oxidant in the liquid. It tells you that the liquid is safe if there is no hazardous liquid concentration in the liquid. In step 2, if there is a hazardous liquid concentration in the liquid content, it decides the type of the liquid, i.e. whether it is flammable or oxidant (oxidiser). In the third stage, if the liquid is a flammable liquid, it finds the type of liquid (Methanol, ethanol, 1-propanol and Isopropanol) and % of the flammable concentration in the liquid. The steps of the algorithm are given in Fig. 2.

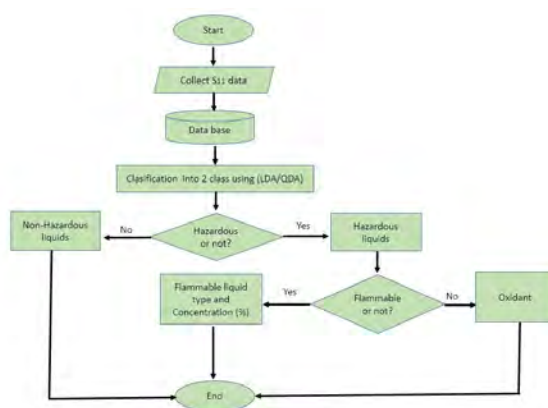


Figure 2. Flowchart of the classification phase

For liquid identification, predictions were made for a total of 49 liquids, 41 hazardous and 8 non-hazardous liquids. In this prediction, 2 different algorithms were used to select the most successful algorithm and the performances of the algorithms were compared. The types of the liquids tested are given in Table 1.

Table 1. Liquid types.

	Hazardous liquids		Non-hazardous liquids
	Inflammable	Oxidant	
Pure	Impure		
Ethanol	Ethanol-water (10%-90%)	Hydrogen peroxide	Cola
Methanol	Methanol-water (10%-90%)		Liquid Soap
1-propanol	1-propanol-water (10%-90%)		Shampoo
Isopropanol	Isopropanol-water (10%-90%)		Milk
			Body lotion
			Buttermilk
			Ice-tea
			Cherry juice

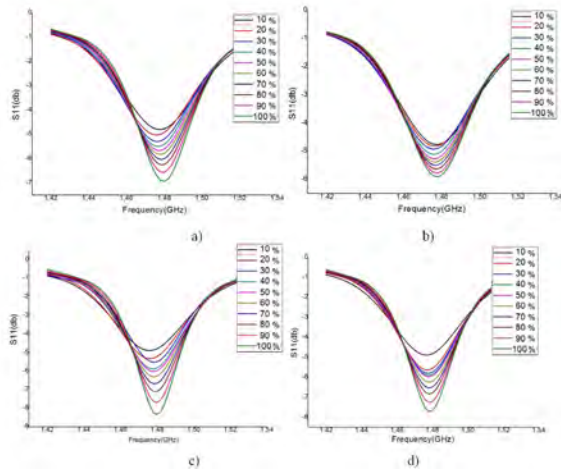


Figure 3. S_{11} parameters of the water- flammable liquids solutions of different flammable liquid concentrations a) Ethanol b) Methanol c) 1-Propanol, d) Isopropanol.

RESULTS AND DISCUSSION

The proposed microwave measurement system was used to measure all liquids. S parameter measurement of pure (100% flammable liquids) and their aqueous solutions containing 10-90% flammable liquid by volume are given in Fig. 3 and the measurement of other liquids are given in Fig. 4.

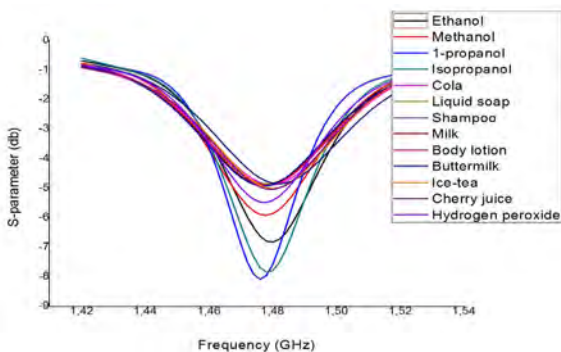


Figure 4. S-parameter measurement of different liquids

Performance Metrics

There are some performance metrics used to compare the classification performance of algorithms. These metrics indicate which classification algorithm performs better in the given setting. One of the performance metrics used in the study is the accuracy criterion, which gives the total sample rate of correctly classified samples. The accuracy rate of the classification algorithm is calculated using (10).

$$\text{Accuracy} = \frac{TP + TN}{TP + TN + FP + FN} \quad (10)$$

where, TP (True positive) is positive test result when actual state is positive, FP (False positive) is positive test result when actual state is negative, TN (True negative) is negative test result when actual state is negative, and FN (False negative) is negative test result when actual state is positive.

Precision and Recall values are also among the performance metrics used and it is accepted that a classifier with high Precision and high Recall values makes a good classification. Precision (P) is the number of TP over the number of TP plus the number of FP (11).

$$P = \frac{TP}{TP + FP} \quad (11)$$

Recall (R) is the number of TPs over the number of TP plus the number of FN (12).

$$R = \frac{TP}{TP + FN} \quad (12)$$

Another commonly used performance metric is Kappa and is calculated using (13). P(a) represents the algorithm's accuracy, P(e) represents the weighted average of the expected accuracy of the algorithm, which makes random predictions in the same dataset. If a classification is successful, precision and recall values become close to 1.

$$K = \frac{P(a) - P(e)}{1 - P(e)} \quad (13)$$

One of the indicators of how many errors occurred during classification is Root Mean Square Error (RMSE) value and it is calculated using (14).

$$RMSE = \sqrt{\frac{(a_1 - b_1)^2 + \dots + (a_n - b_n)^2}{n}} \quad (14)$$

where a represents the estimated values and b represents the actual values. Confusion matrices are used to measure the success of the algorithm and contain the most descriptive information about the classification results.

Overall Results

The recall precision, Kappa and RMSE values obtained from the classification made using LDA and QDA are given in Fig. 5(a) and (b) in order to compare their performances. As can be seen in Fig. 5(a) the RMSE of QDA was 0.008 but the RMSE of LDA was 0.075. The low RMSE value indicates that QDA classified with fewer errors. While the accuracy of LDA was 92%, the accuracy of QDA was 98%. Recall, Precision and Kappa value also indicate the success of QDA. The Precision value of LDA in classifications was 0.97, the Recall and Kappa values were 0.96 and 0.91, respectively. The higher of these values (precision 1, recall 0.99 and Kappa 0.99) indicates that

Table 2. Accuracy of the proposed approach for different liquids

Type of liquids	Tested liquids	LDA		QDA		
		Correctly predicted liquids	Incorrectly predicted liquids	Correctly predicted liquids	Incorrectly predicted liquids	
Non-hazardous liquids	Cola	Cola		Cola	---	
	Soap	Soap		Soap	---	
	Shampoo	Shampoo		Shampoo	---	
	Milk	Milk	Buttermilk	Milk	---	
	Body lotion	Body lotion		Body lotion	---	
Hazardous Liquids	Buttermilk	Buttermilk		Buttermilk	---	
	Ice-tea (peach)	Ice-tea (peach)		Ice-tea (peach)	---	
	Cherry juice	Cherry juice		Cherry juice	---	
	Ethanol (10, 20, 30, 40, 50, 60, 70, 80, 90, 100)%	Ethanol (20, 30, 40, 50, 60, 70, 80, 90, 100)%	Ethanol %10	Ethanol (10, 20, 30, 40, 50, 60, 70, 80, 90, 100)%	----	
	Methanol (10, 20, 30, 40, 50, 60, 70, 80, 90, 100)%	Methanol (20, 30, 40, 50, 60, 70, 80, 90, 100)%	Methanol %10	Methanol (10, 20, 30, 40, 50, 60, 70, 80, 90, 100)%	----	
2nd Step	1-Propanol (10, 20, 30, 40, 50, 60, 70, 80, 90, 100)%	1-Propanol (10, 20, 30, 40, 50, 60, 70, 80, 90, 100)%		1-Propanol (10, 20, 30, 40, 50, 60, 70, 80, 90, 100)%	----	
	Isopropanol (10, 20, 30, 50, 60, 70, 80, 90, 100)%	Isopropanol (10, 20, 30, 40, 50, 60, 70, 80, 90, 100)%		Isopropanol (10, 20, 30, 50, 60, 70, 80, 90, 100)%	----	
	Oxidising liquid	Hydrogen peroxide	Hydrogen peroxide	---	Hydrogen peroxide	---
	3rd Step	Detect flammable liquids concentration	Ethanol (10, 20, 30, 40, 50, 60, 70, 80, 90, 100)%	Ethanol (10, 20, 30, 40, 50, 60, 70, 80, 90, 100)%	Ethanol (10, 20, 30, 40, 50, 60, 70, 80, 90, 100)%	----
		Methanol (10, 20, 30, 40, 50, 60, 70, 80, 90, 100)%	Methanol (10, 20, 30, 40, 50, 60, 70, 80, 90, 100)%	Methanol (10, 20, 30, 40, 50, 60, 70, 80, 90, 100)%	----	
		1-Propanol (10, 20, 30, 40, 50, 60, 70, 80, 90, 100)%	1-Propanol (10, 20, 30, 40, 50, 60, 70, 80, 90, 100)%	1-Propanol (10, 20, 30, 40, 50, 60, 70, 80, 90, 100)%	----	
		Isopropanol (10, 20, 30, 50, 60, 70, 80, 90, 100)%	Isopropanol (10, 20, 30, 50, 60, 70, 80, 90, 100)%	Isopropanol 40%	Isopropanol (10, 20, 30, 50, 60, 70, 80, 90, 100)% Isopropanol 40%	

QDA was more successful.

Information including all liquid recognition experiments and techniques used are given in Table 2. In liquid recognition, the LDA algorithm predicted that buttermilk, which is actually a non-hazardous liquid, was a hazardous liquid, and the hazardous liquid 10% Ethanol and 10% Methanol aqueous solutions were predicted as non-hazardous liquids. It could not accurately predict a total of 3 types of liquids. While the algorithm was estimating the liquid concentration, it predicted the isopropanol-water solution with an isopropanol concentration of 40% as a hazardous liquid, but could not accurately predict its concentration. It can be seen that QDA correctly predicted all liquid types. On the other hand, although it correctly predicted the type of isopropanol-water solution with an isopropanol concentration of 40%, it could not predict the concentration correctly.

CONCLUSION

Fire safety and liquid controls play a key role in preventing loss of life and property that may occur as a result of terrorist attacks and sabotage. In this study, a system for liquid classification using S-parameter measurements and discriminant analysis of liquids in the microwave frequency band is proposed. The false alarm rate of the system is very low, it is a system with a high accuracy rate and can detect even a hazardous liquid with a concentration of 10% in its content. Another advantage of this proposed system is that while other systems only detect liquid, this system can determine both the type of hazardous liquid and the proportion of the hazardous liquid concentration in the liquid. Moreover, this quick identification system is cheaper than other systems. LDA and QDA algorithms were used to select the best algorithm for liquid recognition on the data set obtained.

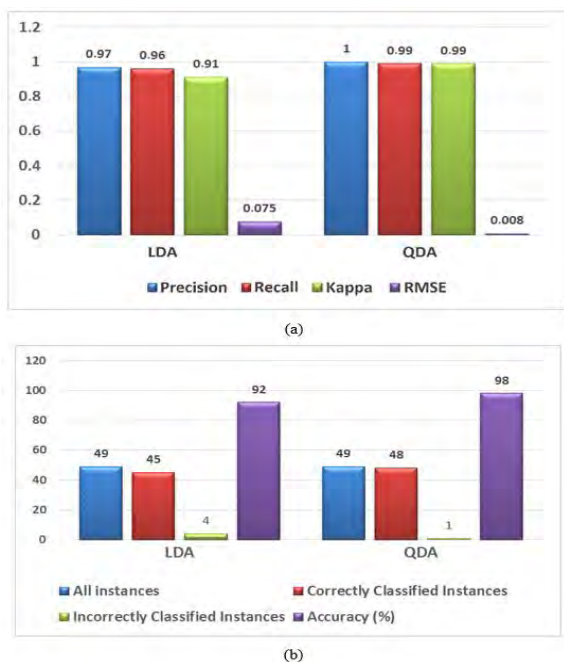


Figure 5. Performance metrics of LDA and QDA algorithms (a) Accuracy related metrics, (b) accuracy rate of LDA and QDA.

ned from microwave measurements and the performances of these algorithms were compared. The results show that QDA can detect liquids with lower RMSE values and higher accuracy rates compared to LDA. A prototype system that integrates the overall process proposed in this study and the experimental setup and uses QDA for liquid classification is under development. After a group of field tests, it can be used for liquid classification at security checkpoints.

CONFLICT OF INTEREST

Authors approve that to the best of their knowledge, there is not any conflict of interest or common interest with an institution/organization or a person that may affect the review process of the paper.

AUTHOR CONTRIBUTION

All the work in this study were performed equally by the authors.

REFERENCES

- Prugh, R.W. Life-safety concerns in chemical plants. *Process Safety Progress*. 35(1) (2016) 18-25.
- Cox, B.L., Carpenter, A.R., Ogle, R.A. Lessons learned from case studies of hazardous waste/chemical reactivity incidents. *Process Safety Progress*. 33(4) (2014) 395-398.
- Morrison, D.T., Stern, M., Osorio-Amado, C.H. Waste solvents to trash haulers: lessons learned from hazardous waste accidents. *Process safety progress*. 37(3) (2018) 427-41.
- Ness, A., Gibson, R. Handling chemicals in small containers. *Process safety progress*. 24(4) (2005) 299-302.
- Alexeev, S., Smirnov, V., Barbin, N., Alexeeva, D.Y. Evolution of the classification of flammable and combustible liquids in Russia. *Process safety progress*. 37(2) (2018) 230-36.
- DaCunha, S., Gerbaud, V., Shcherbakova, N., Liaw, H.J. Classification for ternary flash point mixtures diagrams regarding miscible flammable compounds. *Fluid Phase Equilibria*. 466 (2018) 110-23.
- Stefanidou, M., Athanasis, S., Spiliopoulou, C. Health impacts of fire smoke inhalation. *Inhalation toxicology*. 20(8) (2008) 761-66.
- Purser, D.A., McAllister, J.L. Assessment of hazards to occupants from smoke, toxic gases, and heat. *SFPE handbook of fire protection engineering*. Springer; 2016. p. 2308-428.
- Yuan, S., Zhang, Z., Sun, Y., Kwon, JS-I., Mashuga, C.V. Liquid flammability ratings predicted by machine learning considering aerosolization. *Journal of hazardous materials*. 386 (2020) 121640.
- Yuan, W., Lv, W., Wang, H., Ma, Li, S. H. Performance prediction of suspension freeze crystallization for the treatment of liquid hazardous wastes via machine learning methods, *Journal of Cleaner Production*, (2021) 129629.
- Yuan, Ji, C., Jiao, S., Huffman, Z., El-Halwagi, M., Wang, M.M., Q., Predicting flammability-leading properties for liquid aerosol safety via machine learning, *Process Safety and Environmental Protection*, 148 (2021) 1357-1366.
- Jiao, Z., Ji, C., Yuan, S., Zhang, Z., Wang, Q. Development of machine learning based prediction models for hazardous properties of chemical mixtures, *Journal of Loss Prevention in the Process Industries*, 67 (2020) 104226.
- Zhang, Z., Yuan, S., Yu, M., Mannan, M.S., Wang, Q., A hazard index for chemical logistic warehouses with modified flammability rating by machine learning methods, *ACS Chemical Health & Safety*, 27 (2020) 190-197.
- Mahmodi, K., Mostafaei, M., Mirzaee-Ghaleh, E. Detection and classification of diesel-biodiesel blends by LDA, QDA and SVM approaches using an electronic nose. *Fuel*. 258 (2019) 116114.
- Ji, C., Jiao, Z., Yuan, S., El-Halwagi, M.M., Wang, Q., Development of novel combustion risk index for flammable liquids based on unsupervised clustering algorithms, *Journal of Loss Prevention in the Process Industries*, 70 (2021) 104422
- Li, Z., Haigh, A., Soutis, C., Gibson, A., Sloan, R. Microwaves sensor for wind turbine blade inspection. *Applied Composite Materials*. 24(2) (2017) 495-512.
- Borisov, V., Karpenko, A. Using of the Michelson microwave interferometer for the measurement of permittivity of thin-layer materials. *Russian journal of nondestructive testing*. 37(8) (2001) 597-99.
- Yurchenko, A.V., Novikov, A., Kitaeva, M.V. A resonator microwave sensor for measuring the parameters of Solar-quality silicon. *Russian Journal of Nondestructive Testing*. 48(2) (2012) 109-14.
- Mathur, P., Thakur, A., Kurup, D.G. An artificial neural network-based non-destructive microwave technique for monitoring fluoride contamination in water. *Journal of Electromagnetic Waves and Applications*. 34(5) (2020) 612-22.
- Turgul, V., Kale, I. Permittivity extraction of glucose solutions through artificial neural networks and non-invasive microwave glucose sensing. *Sensors and Actuators A: Physical*. 277 (2018) 65-72.
- Sulaiman, N., Srisatit, S. Development of x-ray imaging technique for liquid screening at airport. *AIP Conference Proceedings: AIP Publishing LLC*; 2016. p. 030006.
- Orachorn, P., Chankow, N., Srisatit, S. An Alternative Method for Screening Liquid in Bottles at Airports Using Low Energy X-ray Transmission Technique. *Radiation environment and medicine: covering a broad scope of topics relevant to environmental and*

- medical radiation research. 8(2) (2019) 77-84.
23. Chen, H., Hu, Z., Wang, P., Xu, W., Hou Y. Application of spectral droplet analysis method in flammable liquids identification. Paper presented at 2019 International Conference on Optical Instruments and Technology: Optical Sensors and Applications: International Society for Optics and Photonics, pp. 1143609, 2020.
 24. Sun, L. Liquid dangerous goods detection based on electronic nose odor recognition technology. Paper presented at International Symposium on Photoelectronic Detection and Imaging 2013: Infrared Imaging and Applications: International Society for Optics and Photonics, pp. 890721, 2013.

Production and Characterization of Palm Oil Based Epoxy Biocomposite by Response Surface Methodology Design

Hakan Sahal¹  Ercan Aydogmus² 

¹Munzur University, Department of Food Processing, Tunceli, Turkey

²Firat University, Department of Chemical Engineering, Elazig, Turkey

ABSTRACT

In this research, some physical and chemical properties of the biocomposite obtained from synthesized epoxy modified palm oil (MPO) and epoxy resin have been characterized. The experimental study plan is made according to Response Surface Methodology (RSM) and biocomposites with different MPO rates are obtained. The chemical bond structure of MPO and epoxy biocomposite has been evaluated with Fourier Transform Infrared Spektrofotometre (FTIR). The experimental and RSM model results obtained, the density of the biocomposite rise as the MPO rate increases. It is determined that the Shore D hardness of the biocomposite is inversely proportional to the MPO rate by mass. As the MPO ratio (wt.%) increases in the biocomposite, the thermal conductivity coefficient and thermal stability also raise. In the thermal decomposition experiments of the obtained biocomposite, it is observed that the thermal stability of the composite goes up as the MPO rate rises. Activation energies are calculated using the Flynn Wall Ozawa, Kissinger, and Coats Redfern models. The activation energies calculated for the 9th, 2nd, and 13th experiments according to the Flynn Wall Ozawa method are approximately 139.65, 143.56, and 145.28 kJ/mol, respectively. The function ($f = (1 - \alpha)^{1.273}$) with the highest R^2 value has been determined according to the Coats Redfern method, and the deviation in Flynn Wall Ozawa and Kissinger model results was below 7%.

Keywords:

Biocomposite; Modified palm oil; Sulfonamide; Characterization; Thermal decomposition.

INTRODUCTION

Today, social awareness of the environmental impacts of plastics is increasing, and therefore environmentally friendly materials are sought for the plastics industry [1–4]. For this reason, in addition to being environmentally friendly, the tendency towards natural fibers is increasing due to their low cost, easy processing, low density, good corrosion resistance, and high strength in wide industrial applications [5–8, 9–14]. Moreover, natural fibers become an alternative to glass fibers by being applied to reinforced polymer composites and natural-based resins, as they contain hydrogen bonds and other bonds that reinforce the structure [15,16]. The use of bio-fibers as substitutes for synthetic fibers (carbon, and glass) as fillers in the development of polymer matrix composites has attracted much attention [17].

There is increased awareness about the properties of natural fiber-based epoxy composites to meet engi-

neering requirements [18]. The use of epoxy composite materials reinforced with natural fibers is increasing strongly in many industrial areas, especially in the automotive sector [19–23], in civil construction [20], and marine production [21] due to their low cost of processing. German carmakers, soon followed by other manufacturers, took the lead in introducing natural fiber composites for interior and exterior applications; parcel shelves, door panels, mirror casing, backrests, voltage stabilizer cover, seat cushions, dashboard parts, projector cover helmet, roof linings, etc. In the civil construction area, they can be used for; beams, building panels, roofing products, autoclaved cement composite, and water tanks. For shipbuilding, the adoption of green composites can potentially represent a valid substitute for fiberglass. These include both purposely grown and harvested fibers, as well as those recovered from agricultural waste. Thanks to their recyclability and renewability, biocomposites allow them to comply with more and more

Article History:

Received: 2021/06/24

Accepted: 2021/11/30

Online: 2021/12/31

Correspondence to: Hakan Sahal,
Munzur University, Food
Processing, Tunceli, TURKEY
E-Mail: hakansahal@munzur.edu.tr

stringent environmental protection regulations [24,25] improving also the cost-effectiveness [26]. Increasing the mechanical performance of these materials is a mandatory task to spread their use not only in non-structural applications but also in semi and proper structural applications limited by their failure mechanisms [27].

Vijaya Ramnath et al. [28] conducted a study on the evaluation of mechanical properties of abaca–jute–glass fiber reinforced epoxy composite and revealed that abaca fiber had the highest flexural strength compared to jute fiber, with the values of 12.5 and 11.9 MPa, respectively, since its strength increased with improved interfacial adhesion. Besides that, Abaca exhibited more strength when it absorbed moisture.

Szolnoki et al. [29] reinforced twill woven hemp fabric with epoxy composites and discovered that the modification of the fabrics led to decreased flammability of the reference matrix composites, characterized with increased limiting oxygen index values and reduced heat release rate by 25%. Moreover, composites of modified fabric showed improvements in static and dynamic mechanical properties.

Pickering et al. [30] experimented on aligned short harakeke fiber (New Zealand flax) mats impregnated with epoxy resin. The result showed that these composites were found to possess significantly higher tensile properties at 46% fiber loading, than planar random-oriented short fiber composites, with the values of 136 MPa and 76.2 MPa, respectively. The epoxy resin is a feasible polymer, which has effective strength, good toughness, and appreciable resilience. It has good resistance to moisture and chemical attack. It also has great electrical insulating properties and is devoid of volatile matter [31].

Abu Bakar et al. [32], through their study, reported that one of the flaws of natural fibers is poor compatibility with its matrix. Moreover, studies done by Hassan et al. [33] showed that the recyclability of natural fiber within the automotive component had reduced the automotive weight. The use of biocomposite helped in a 25% reduction of vehicle weight, which consequently contributed to saving 39.45 trillion of crude oil [33]. Besides that, this material can be used for the composite frame in electromobility vehicles, as it will reduce energy consumption [9]. Currently, natural fibers are used as fillers to replace glass fiber in polymer composites [34].

The incompatibility and poor adhesion of natural fiber in a polymer matrix are usually addressed by fiber treatment and modification to enhance effective wetting and uniform dispersion. The primary techniques used for fiber treatment and modification can be grouped into fiber pretreat-

ment, surface coating modified with coupling agents, and in situ compatibilization during processing depending on the practical applications. Mercerization, a chemical treatment using alkali, is widely used to fibrillate and purify fibers (partially removing oil, wax, pectin, hemicellulose, and lignin) before composite fabrication.

For example, Rihayat et al. [35] and Wang et al. [36] have reported that biocomposites treated with alkaline solutions and silane fusing agents have twice the tensile strength of composites without temporary treatment. Mahmoud et al. [37], Kang and Kim [38] reported an increase in tensile strength, modulus of elasticity, and moisture resistance of biocomposites with the coupling agent in the composite matrix. Alkalisiation refers to the treatment of fibers in an alkaline solution by dissolving some unstable fiber components such as hemicellulose, lignin, pectin, and other impurities so that the surface of the fiber becomes cleaner and rougher, which results in better mechanical interlocking between the fiber and the polymer. Lee and Wang [39], and Fan [40] have found that bamboo fibers treated at 6% NaOH produce the highest tensile properties of single fibers and matrix adhesion strength. Similar studies on other natural fibers using 5% NaOH concentration revealed comparable results, with higher NaOH concentrations causing a decrease in mechanical properties.

In many studies in the literature, vegetable oils have been modified and used in the synthesis of composites. Especially, biocomposite production can be made as a result of the epoxidation of triglyceride structures found in vegetable oils [41]. For example, when palm oil is modified by various processes, a biopolymer can be easily obtained by a chemical reaction [42]. It is known that the synthesized biocomposite, in which palm oil is used in the production of polyester composites, improves some of the thermophysical properties [43]. Evaluation of such similar sources in the production of biocomposites with epoxy resin is becoming more and more common. Because the epoxidation of triglyceride structures in vegetable oils easily offers many options for the development of bio-epoxy composites as raw materials. The advantages of the synthesized bio-epoxy composites such as being environmentally friendly, more thermally stable, and easy to process make such studies important [44].

The original aspect of this research is the synthesis of biocomposite using the modified epoxy palm oil. Unlike studies in the literature, palm oil has been modified that functional epoxy and hydroxyl structures are bonded for the production of biocomposite.

This study aims to treatment fiber with alkali where had effects on the mechanical properties improvement of natural fiber such as increased cellulose content and the

degree of crystallinity, which is indicative of higher fiber strength and stiffness; increased surface roughness topography for better mechanical interlocking between the fiber and matrix; increased cellulose exposure for increased bonding/reaction sites on the fiber surface; and increased surface energy for better wetting and compatibility. Treatment with a mild alkaline condition is typically sufficient to remove fiber impurities with minimal impact on the fiber texture and structure whereas higher alkaline concentration can lead to excessive removal of lignin and fiber damage. Furthermore, according to the study, the use of cellulosic fiber as reinforcement can reduce the material cost and at the same time raising strength to weight ratios [28].

MATERIALS AND METHODS

Materials

All chemicals used for the biocomposite production and analysis have been supplied from Merck and used without purifications. Epoxy raw material and hardener components are procured from Polisan (Turkey). Experimental studies use ethyl acetate (99.5%), ortho-phosphoric acid (85%), ethanol (99.5%), hydrochloric acid (37%), methanol (99.5%), and hydrogen peroxide (35%). Palm oil with a density of 904 kg/m³ and a viscosity of 77 cP is supplied from commercial companies.

Methods Used in The Experimental Study

In the experimental study, firstly palm oil (100 g) is mixed with acetic acid (45 g), ethyl acetate (10 g), and hydrogen peroxide (90 g). Phosphoric acid (0.02 g) is added to the mixture and stirred at 500 rpm and 60°C for 6 hours. After this process is completed, the light phase is recovered using a vacuum rotary evaporator. Then methanol (70 ml), ethanol (30 ml), and distilled water (100 ml) are added to the system. HCl (0.02 g) is dropped into the mixture and the aqueous and organic phases are separated after being mixed at 500 rpm and 70°C for 12 hours. The oil phase is washed with warm water until the pH is neutral. The modified epoxy palm-oil-based raw material (MPO) is obtained by removing impurities (methanol, ethanol, and water) with a vacuum rotary evaporator.

In the second stage, 5 g of MPO and 0.5 g of 4-(2-aminoethyl)benzene sulfonamide were placed in a flask. It was reacted in reflux state for 2 hours by adding 10 mL of ethanol. Then, the reaction temperature was brought to 60°C and the reaction was continued for 72 hours. At the end of the period, the second stage was passed. MPO was added to commercial epoxy medium according to the ratios indicated in 0-10 wt.% and mixed at 500 rpm for 15 minutes

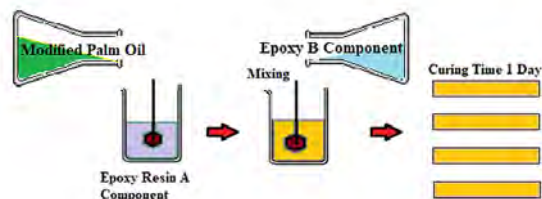


Figure 1. Experimental working schema for the biocomposite production.

to ensure the homogenization of the composite. Then, the hardener part was added to the medium and mixed at the same mixing speed for 15 minutes. At the end of the period, the solvent was removed with the evaporator and quickly transferred to the standard molds. It was left to cure for 24 hours at room conditions. Commercial epoxy resin has approximately 5/8 main components and 3/8 hardener components by mass. Biocomposite production was carried out according to the order in the schema in Fig. 1.

The chemical bond structure of the bio-epoxy composite has been analyzed with an FTIR spectrophotometer. The FTIR spectrum of each sample has been determined as transmittance (%) in the wavelength range of 600 cm⁻¹ to 4000 cm⁻¹. FTIR measurements have been made using Shimadzu QATR-S (IR Spirit S1102SC). The FTIR spectrum of biocomposites has been investigated by ATR method directly in solid powder form without making potassium bromide (KBr) pellets. Besides, the thermal decomposition of the biocomposite with the proportional integral derivative (PID) system, its hardness with the Shore D test, and its thermal conductivity coefficient (Thermtest TLS-100) with the thermal conductivity measuring device have been determined.

Thermal decomposition kinetics of biocomposites in an inert environment (nitrogen) have been investigated with the PID-controlled system. In this system, the temperature increase of 10 K/min from 25°C to 605°C is studied in non-isothermal conditions. The PID system has a total diameter of 19.5 cm, and a height of 21.5 cm. It is made of perlite-reinforced insulated mortar (5 cm thick), rock wool (1.5 cm thick), and aluminum plate (1 mm thick). The drying cell was placed in the cylindrical space (approximately inner diameter 6 cm) in the inner center of the reactor. The cylindrical drying cell has a diameter of 3.5 cm, a height of 3 cm, and a porous side surface area (nearly porous diameter 1-3 mm). The drying cell made of galvanized steel plate (1 mm thick) is placed in the center of the PID system. In this system, temperatures can be controlled very precisely with the help of thermocouples. A certain amount of sample (1 gram) can be taken and the temperature can be easily distributed on all surfaces to the conductive and porous cell.

Thermal Decomposition Kinetics and Modeling

In model equations: M_t is the mass at time t , M_i is the initial mass and M_f is the final mass. α is the conversion ratio, β is the temperature rise ratio, $k(T)$ is the temperature-dependent function and $f(\alpha)$ is the conversion-dependent function. $k(T)$ expresses the thermal decomposition rate constant, it is also a function that changes depending on the temperature. In experiments, the temperature increase in non-isothermal conditions changes the thermal decomposition rate constant over time. $f(\alpha)$ is a function depending on the conversion ratio and is defined as a special mathematical function that expresses the variation of the conversion ratio with time or temperature. The $g(\alpha)$ function corresponds to the function found by integrating $d\alpha/f(\alpha)$ [41-44].

$$\alpha = \frac{M_t - M_f}{M_i - M_f} \tag{1}$$

$$k(T) = A \exp\left(-\frac{E}{RT}\right) \tag{2}$$

$$\frac{d\alpha}{dt} = k(T)f(\alpha) \tag{3}$$

$$f(\alpha) = (1 - \alpha)^n \tag{4}$$

$$\ln\left(\frac{g(\alpha)}{T^2}\right) = \ln \frac{AR}{E\beta} - \frac{E}{RT} \tag{5}$$

$$\ln(\beta) = \ln\left(\frac{AE}{g(\alpha)R}\right) - 5.3305 - 1.052\left(\frac{E}{RT}\right) \tag{6}$$

$$\ln\left(\frac{\beta}{T^2}\right) = \ln \frac{AR}{g(\alpha)E} - \frac{E}{RT} \tag{7}$$

The activation energy (E), Arrhenius constant (A), and R (8.314 J/mol-K) values are expressed from the model equations. In Eq. 3, it can be solved by writing Arrhenius Equation instead of $k(T)$. Coats Redfern (Eq. 5), Flynn Wall Ozawa (Eq. 6), and Kissinger (Eq. 7) models are shown in the above equations. Here, the activation energy values of the biocomposite have been calculated using Coats Redfern, Flynn Wall Ozawa, and Kissinger methods. According to Coats Redfern method, if the activation energy is plotted $1/T$ versus $\ln(g(\alpha)/T^2)$, the slope gives $-E/R$. In the Flynn Wall Ozawa method, if $1/T$ versus $\ln(\beta)$ is plotted on the graph, the slope is found

Table 1. Proximate analyses result of the experimental samples.

Experiments	Moisture (%)	Ash (%)	Others (%)
Run No: 9	5.87	1.56	92.57
Run No: 2	6.12	1.75	92.13
Run No: 13	6.59	1.92	91.49

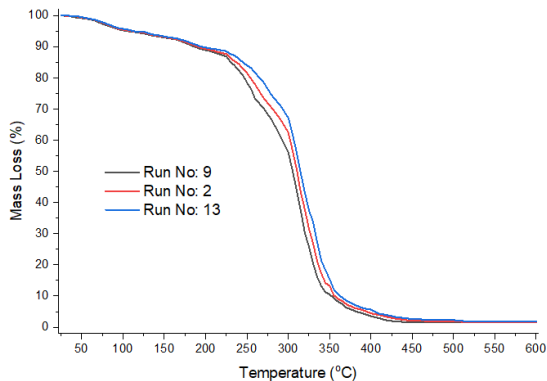


Figure 2. The effect of MPO content in the biocomposite for the thermal decomposition.

by the expression $-1.052E/R$. In the Kissinger method, if $1/T$ versus $\ln(\beta/T^2)$ is plotted, the slope is found as $-E/R$ [45-50].

RESULTS AND DISCUSSIONS

Proximate Analysis of The Biocomposites

Thermal degradation of biocomposites results is interpreted for specific experiments in Fig. 2 and Table 1. In thermal degradation experiments, physical decompositions (such as water, moisture) occurred in the first region, while chemical decompositions occurred in the second and third regions. It is possible to divide the chemical degradation of biocomposites into two in general. Weak structures that can chemically decompose at low temperatures degrade primarily in the composite, while groups with stronger thermal strength decompose slowly at higher temperatures [43-48].

RSM Results for The Biocomposite

According to the RSM experimental study plan, the rate of epoxy components (wt.%) was kept constant in the production of the bio-epoxy composite. The mass percent values of epoxy resin and MPO have been entered into the program as the input data of RSM. RSM outputs are determined by the density of the obtained biocomposite, Shore D hardness, and thermal conductivity results. In Table 2, the experimental plan and response values arranged according to the RSM design are given.

In experimental studies, the results have been evaluated using analysis of variance (ANOVA) and RSM. When the obtained model equations are checked in ANOVA analysis, it is seen that the Quadratic Power model is suitable for this design. Also, R^2 values are found to be quite high and other error functions are also low.

According to the RSM results in Fig. 3, it is aimed to obtain maximum efficiency with the minimum economy

Table 2. The experimental study and RSM of the bio-epoxy composites.

Run No	Epoxy Resin (wt.%)	MPO (wt.%)	Density (kg/m ³)	Shore D Hardness	k (W/m-K)
1	94.74	5.26	1164.27	74.39	0.097
2	95.00	5.00	1161.96	74.46	0.096
3	95.00	5.00	1161.97	74.47	0.096
4	95.00	5.00	1161.98	74.48	0.096
5	95.00	5.00	1161.96	74.46	0.096
6	95.24	4.76	1159.89	74.55	0.095
7	90.48	9.52	1201.47	73.02	0.111
8	92.03	7.97	1187.92	73.52	0.106
9	100.00	0.00	1118.30	76.07	0.079
10	98.42	1.58	1132.07	75.57	0.084
11	98.54	1.46	1131.09	75.60	0.084
12	95.00	5.00	1161.97	74.47	0.096
13	91.46	8.54	1192.84	73.34	0.108

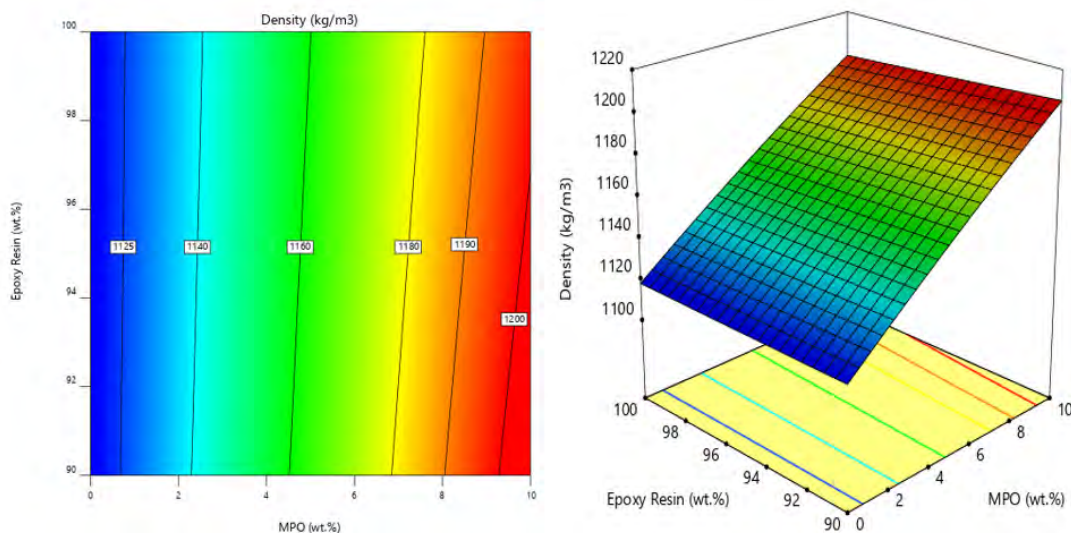


Figure 3. Effect of MPO (wt.%) rate on the density of biocomposite.

under optimum conditions in experimental studies. This method will save both time and raw material spent. With this method, 13 experiments are performed in the experimental study plan of RSM and theoretically, at least 100 compatible results are found. In Fig. 3, it can be stated that the density of the biocomposite increases depending on the MPO rate. The density of the composite can vary according to the polymer matrix structure, pore distribution, additives, and fillers [51,52].

In Fig. 4, experimental data and RSM model results have been evaluated by statistical analysis. The distribution of the actual values and the predicted data within the 95%

confidence interval is compared. In Eq. 8, the RSM polynomial function for density is expressed (A: MPO wt.%, and B: Epoxy Resin wt.%).

$$\begin{aligned} \rho = & +1160.36113 + 16.65252 \cdot A \\ & - 0.853011 \cdot B - 0.078989 \cdot A \cdot B \\ & - 0.083227 \cdot A^2 + 0.004319 \cdot B^2 \end{aligned} \quad (8)$$

It is seen in Fig. 5 that the Shore D hardness decreases as the rate of MPO by mass increases in the biocomposite. Fig. 6 shows the agreement between statistical analysis and experimental data and RSM model values. According to the power model in the RSM central composite method, the Shore D polynomial function is expressed in Eq. 9.

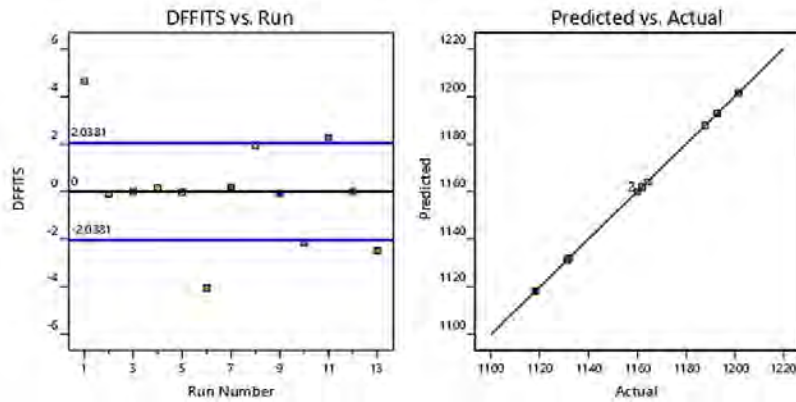


Figure 4. Comparison of experimental data and RSM model for the density of biocomposite.

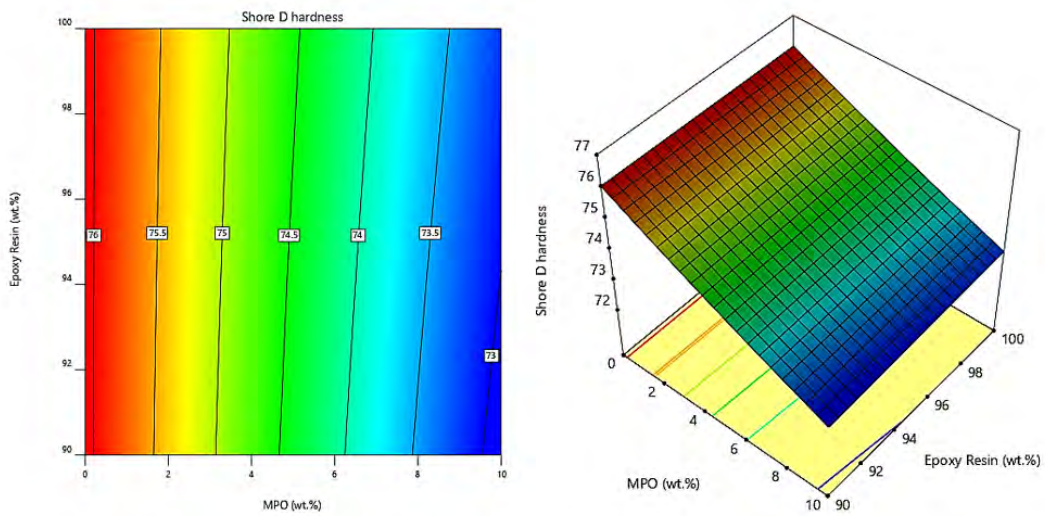


Figure 5. Effect of MPO (wt.%) rate on Shore D hardness of the biocomposite.

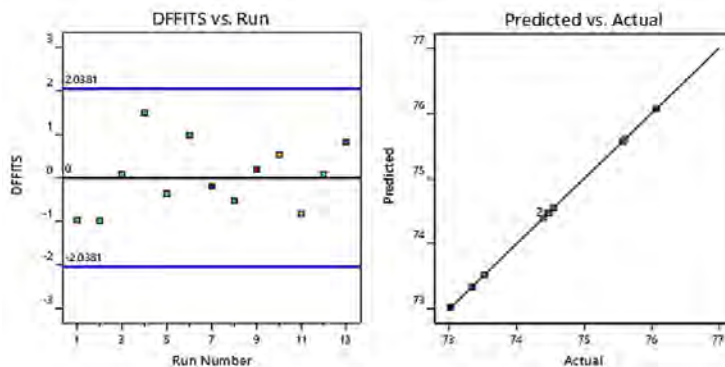


Figure 6. Comparison of experimental data and RSM model for Shore D hardness.

$$\begin{aligned}
 ShoreD = & +76.39007 - 0.620282 \cdot A \\
 & - 0.007175 \cdot B + 0.003000 \cdot A \cdot B \\
 & + 0.003040 \cdot A^2 + 0.000040 \cdot B^2
 \end{aligned}
 \tag{9}$$

The effect of the MPO ratio on the thermal conductivity coefficient of the biocomposite is compared in Fig. 7, and the compatibility of the experimental data with the theoretical model is evaluated in Fig. 8. The polynomial

function expression of the thermal conductivity coefficient according to the RSM power model is expressed in Eq. 10.

$$\begin{aligned}
 k = & +0.098413 + 0.006392 \cdot A \\
 & - 0.000399 \cdot B - 0.000030 \cdot A \cdot B \\
 & - 0.000032 \cdot A^2 \\
 & 2.03223 \cdot 10^{-6} \cdot B^2
 \end{aligned}
 \tag{10}$$

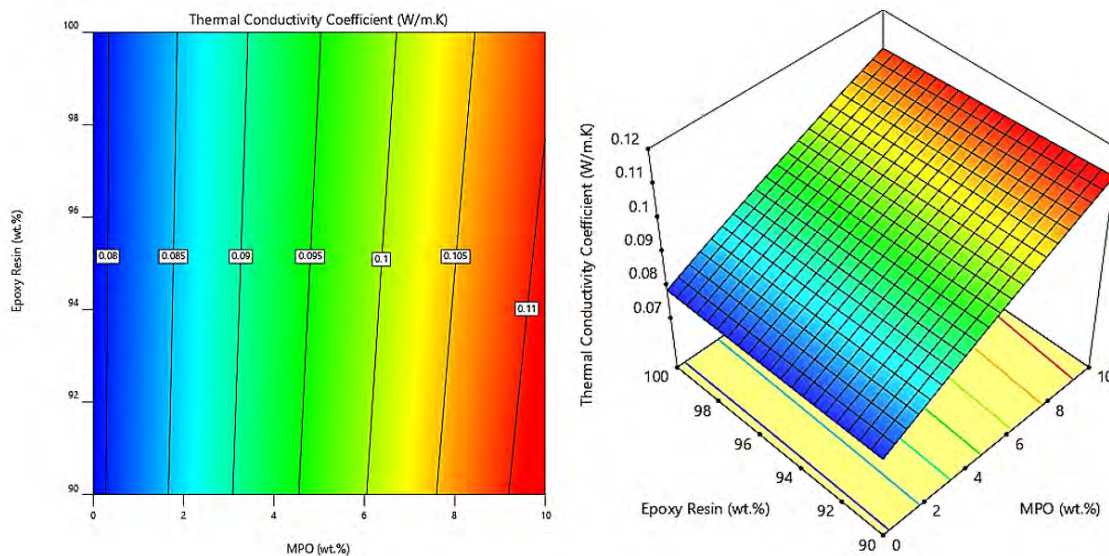


Figure 7. Effect of MPO (wt.%) rate on the thermal conductivity of the biocomposite.

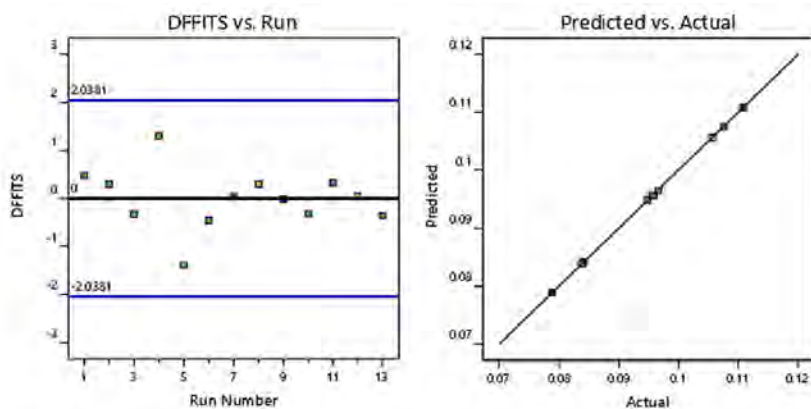


Figure 8. Comparison of experimental data and RSM model for the thermal conductivity.

Table 3. Statistical (ANOVA) evaluation of RSM results for the biocomposites.

Parameters	Source	P-value	SST	Std. Dev.	C.V.%	R ²	Adj. R ²
ρ (kg/m ³)	Quadratic	< 0.01	7.78	0.0399	0.0134	0.9989	0.9976
Shore D	Quadratic	< 0.01	1.13	0.0165	0.0120	0.9991	0.9985
k (W/m.K)	Quadratic	< 0.01	0.64	0.0087	0.0901	0.9982	0.9973

Statistical (ANOVA) evaluation for density, Shore D hardness, and coefficient of thermal conductivity is given in Table 3. High R^2 and adjusted R^2 values, good RSM model significance values (P -value<0.01), low error function (SST), and low standard deviation indicate that the theoretical model is successful according to the experimental results [53-57].

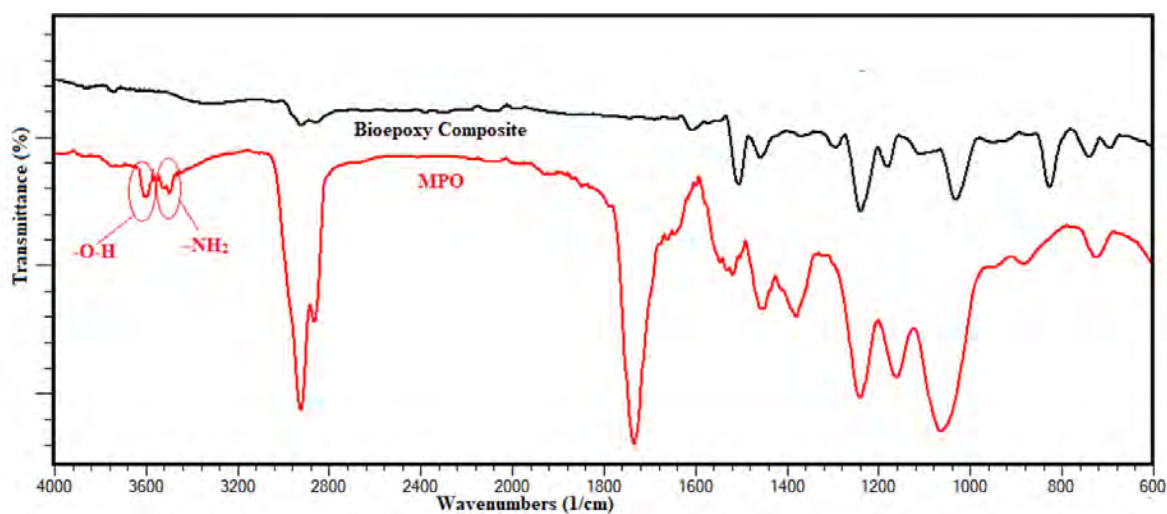
FTIR Spectrophotometer

FTIR spectrum of extracted oil samples attained in the wavenumber region between 4000 and 600 cm^{-1} . The result from FTIR is tabulated in Table 4. At the vibra-

tion at 3005 cm^{-1} , a stretch of =C-H, corresponding to an alkene, is observed. Symmetrical and asymmetrical stretching of C-H is observed in vibration at 2922 and 2852 cm^{-1} . The intense band observed at 1743 cm^{-1} is the result of C=O vibrations indicating the presence of saturated aliphatic esters. This group is also known as triglyceride, the predominant component in fats and oils [58]. The peak at 1510 cm^{-1} indicates stretching of the C=C of the alkene group. The peak at 1460 cm^{-1} is observed due to C-C stretching in the aromatics group [59]. The peak at 3478 cm^{-1} , which occurs with the modification of palm oil, belongs to the hydroxyl group. It shows that the structure which is expected to disappear after the

Table 4. Results from FTIR analysis of the components.

	Palm oil peak (cm ⁻¹)	Epoxy Palm oil peak (cm ⁻¹)	MPO (cm ⁻¹)
-OH	----	3478	3538-3500
-SO ₂ -N-H	----	----	3357-3269
Stretching of=C-H	3005	----	----
Symmetric and Asymmetric stretching of C-H	2922-2852	2929-2875	2945-2858
Triglyceride (TGA)	1743	1628	1721
Stretching of C=C	1510	-----	
Stretching of C-C	1460	1455	
Asymmetric stretching -SO ₂	----	----	1367-1228
Oxirane group	-----	833	----

**Figure 9.** FTIR spectrum of the biocomposite and MPO.

modification of =C-H and C=C stresses corresponding to an alkene in vibration at 3005 cm⁻¹ and 1510 cm⁻¹ is formed. However, the peak formation of the oxirane group at 833 cm⁻¹ supports the expected structure [60]. The peaks at 3357 and 3269 cm⁻¹ observed in MPO spectrum belong to the -SO₂-N-H group [61-63]. The observation of 1367 and 1228 cm⁻¹ asymmetric stretching peaks of -SO₂ confirms the binding [64]. Epoxide ring-opening is generally observed with an increasing peak of hydroxyl peak. It is known that the shift of the hydroxyl characteristic peak from high to low wave number represents increased hydrogen bonding in the network. However, the disappearance of the oxirane peaks at 833 cm⁻¹ and the increase in the hydroxyl peak intensity confirm this information.

The FTIR spectrum in Fig. 9 shows the chemical bonds found in MPO and biocomposite. The disappearance of both -O-H groups and -NH₂ groups in MPO in the biocomposite indicates that these groups are lost by entering the chemical reaction.

CONCLUSION

According to the results obtained, although the increase in the MPO ratio by mass increased the density, thermal conductivity, and thermal stability of the bio-epoxy composite, it decreased the Shore D hardness.

As the MPO rate (wt.%) in the produced biocomposite goes up, the thermal stability of the composite also rises. Calculated activation energies of the biocomposite according to the Flynn Wall Ozawa method are found to be 139.65 kJ/mol (Run No: 9), 143.56 kJ/mol (Run No: 2), and 145.28 kJ/mol (Run No: 13). According to the Coats Redfern method, the best model is determined by the function ($f = (1 - \alpha)^{1.273}$). Coats Redfern, Flynn Wall Ozawa, and Kissinger model results, the deviation in the calculated activation energy values of the biocomposites are found below 7%. Experimental studies are carried out under non-isothermal conditions, and kinetic parameters are calculated with the best model approach. The model results are found in the

statistical analysis with minimum R^2 error functions and maximum efficiency values.

CONFLICT OF INTEREST

The authors declare that they have no known competing financial interests or personal relationships that could have appeared to influence the work reported in this paper.

AUTHOR CONTRIBUTION

All the work in this study were performed equally by the authors.

References

- Zamri MH, Akil HM, MohdIshak ZA. Pultruded Kenaf Fibre Reinforced Composites: Effect of Different Kenaf Fibre Yarn Tex. *Procedia Chem.* 19 (2016) 577–585.
- Ilyas RA, Sapuan SM. The Preparation Methods and Processing of Natural Fibre Biopolymer Composites. *Curr. Org. Synth.* 16 (2020) 1068–1070.
- Ilyas RA, Sapuan SM. Biopolymers and Biocomposites: Chemistry and Technology. *Curr. Anal. Chem.* 16 (2020) 500–503.
- Abral H, Atmajaya A, Mahardika M, Hafizulhaq F, Handayani DK, Sapuan SM, Ilyas RA. Effect of ultrasonication duration of polyvinyl alcohol (PVA) gel on characterizations of PVA film. *J. Mater. Res. Technol.* 9 (2020) 2477–2486.
- Faruk O, Bledzki AK, Fink HP, Sain M. Biocomposites reinforced with natural fibers: 2000–2010. *Prog. Polym. Sci.* 37 (2012) 1552–1596.
- Ilyas RA, Sapuan SM, Atikah, MSN, Asyraf MRM, Rafiqah SA, Aisyah HA, Nurazzi NM, Norraahim MNF. Effect of hydrolysis time on the morphological, physical, chemical and thermal behavior of sugar palm nanocrystalline cellulose (*Arenga pinnata* (Wurmb.) Merr). *Text. Res. J.* 91(2021) 152–167.
- Ilyas RA, Sapuan SM, Ibrahim R, Abrial H, Ishak MR, Zainudin ES, Atikah MSN, Mohd Nurazzi N, Atiqah A, Ansari MNM, Syafri E, Asrofi M, Sari NH, Cumaidink R. Effect of sugar palm nanofibrillated cellulose concentrations on morphological, mechanical and physical properties of biodegradable films based on agro-waste sugar palm (*Arenga pinnata* (Wurmb.) Merr) starch. *J. Mater. Res. Technol.* 8 (2019) 4819–4830.
- Ilyas RA, Sapuan SM, Ibrahim R, Abrial H, Ishak MR, Zainudin ES, Asrofi M, Atikah MSN, Huzaifah MMR, Radzi AM, Azammi AMN, Shaharuzaman MA, Nurazzi NM, Syafri E, Sari NH, Norraahim MRF, Jumaidin R. Sugar palm (*Arenga pinnata* (Wurmb.) Merr) cellulosic fibre hierarchy: A comprehensive approach from macro to nanoscale. *J. Mater. Res. Technol.* 8 (2019) 2753–2766.
- Aisyah HA, Paridah MT, Sapuan SM, Khalina A, Berkalp OB, Lee SH, Lee CH, Nurazzi NM, Ramli N, Wahab MS, Ilyas RA. Thermal Properties of Woven Kenaf/Carbon Fibre-Reinforced Epoxy Hybrid Composite Panels. *Int. J. Polym. Sci.* (2019) 1–8.
- Jumaidin R, Saidi ZAS, Ilyas RA, Ahmad MN, Wahid MK, Yaakob MY, Maidin NA, Rahman MHA, Osman MH. Characteristics of Cogon Grass Fibre Reinforced Thermoplastic Cassava Starch Biocomposite: Water Absorption and Physical Properties. *J. Adv. Res. Fluid Mech. Therm. Sci.* 62 (2019) 43–52.
- Alsubari S, Zuhri MYM, Sapuan SM, Ishak M.R, Ilyas R.A, Asyraf M.R.M. Potential of Natural Fiber Reinforced Polymer Composites in Sandwich Structures: A Review on Its Mechanical Properties. *Polymers* 13 (2021) 423.
- Omran AAB, Mohammed AABA, Sapuan SM, Ilyas RA, Asyraf MRM, Koloor SSR, Petru M. Micro- and Nanocellulose in Polymer Composite Materials: A Review. *Polymers.* 13 (2021) 231.
- Nurazzi MN, Asyraf MRM, Khalina A, Abdullah N, Sabaruddin FA, Kamarudin SH, Ahmad S, Mahat AM, Lee C.L, Aisyah H.A, Norraahim MNF, Ilyas RA, Harussani MM, Ishak B, Sapuanca SM. Fabrication, Functionalization, and Application of Carbon Nanotube-Reinforced Polymer Composite: An Overview. *Polymers.* 13 (2021) 1047.
- Aisyah HA, Paridah MT, Sapuan SM, Ilyas RA, Khalina A, Nurazzi NM, Lee SH, Lee CH. A Comprehensive Review on Advanced Sustainable Woven Natural Fibre Polymer Composites. *Polymers.* 13 (2021) 471.
- Jumaidin R, Khiruddin MAA, Saidi ASZ, Salit MS, Ilyas RA. Effect of cogon grass fibre on the thermal, mechanical and biodegradation properties of thermoplastic cassava starch biocomposite. *Int. J. Biol. Macromol.* 146 (2020) 746–755.
- Sanjay MR, Arpitha GR, Naik LL, Gopalakrishna K, Yogesha B. Applications of Natural Fibers and Its Composites: An Overview. *Nat. Resour.* 7 (2016)108–114.
- Asyraf MRM, Ishak MR, Sapuan SM, Yidris N, Ilyas RA. Woods and composites cantilever beam: A comprehensive review of experimental and numerical creep methodologies. *J. Mater. Res. Technol.* 9 (2020) 6759–6776.
- Ayu RS, Khalina A, Harmaen A.S, Zaman K, Isma T, Liu Q, Ilyas RA, Lee CH. Characterization Study of Empty Fruit Bunch (EFB) Fibers Reinforcement in Poly (Butylene) Succinate (PBS)/Starch/Glycerol Composite Sheet. *Polymers.* 12 (2020) 1571.
- Holbery J, Houston D. Natural-fiber-reinforced polymer composites in automotive applications. *JOM.* 58 (2006) 80–86.
- Kim YK, Chalivendra V. Natural fibre composites (NFCs) for construction and automotive industries. In *Handbook of Natural Fibres*; Elsevier: Amsterdam, The Netherlands, 469–498, 2020.
- Fragassa C. Marine applications of natural fibre-reinforced composites: A manufacturing case study. In *Advances in Applications of Industrial Biomaterials*; Springer: Berlin/Heidelberg, Germany, 21–47, 2017.
- Jaafar ACN, Zainol I, Ishak NS, Ilyas RA, Sapuan SM. Effects of the Liquid Natural Rubber (LNR) on Mechanical Properties and Microstructure of Epoxy/Silica/Kenaf Hybrid Composite for Potential Automotive Applications. *J. Mater. Res. Technol.* 12 (2021) 1026–1038.
- Rezaifard AH, Hodd KA, Tod DA, Barton JM. Toughening epoxy resins with poly (methyl methacrylate)-grafter-natural rubber and its use in adhesive formulations. *Int. J. Adhes. Adhes.* 14 (1994) 153–159.
- Technotes BE. Composite Recycling, and Disposal An Environmental R&D Issue. *Boeing Environ. Technotes.* 8 (2003) 1–4.
- Bandyopadhyay S. Source composite curve for waste reduction. *Chem. Eng. J.* 125 (2006) 99–110.
- Sanjay MR, Madhu P, Jawaid M, Senthamaraiannan P, Senthil S, Pradeep S. Characterization and properties of natural fiber polymer composites: A comprehensive review. *J. Clean. Prod.* 172 (2018) 566–581.
- Vinod A, Sanjay MR, Suchart S, Jyotishkumar P. Renewable and sustainable biobased materials: An assessment on biofibers, biofilms, biopolymers, and biocomposites. *J. Clean. Prod.* 258

- (2020) 120978.
28. Ramnath VB, Kokan JS, Raja NR, Sathyanarayanan R, Elanchezhian C, Prasad RA, Manickavasagam V.M. Evaluation of mechanical properties of abaca-jute-glass fibre reinforced epoxy composite. *Mater. Des.* 51 (2013) 357–366.
 29. Szolnoki B, Bocz K, S6ti PL, Bodzay B, Zimonyi E, Toldy A, Morlin B, Bujnowicz K, Wladyka-Przybylak M, Marosi G. Development of natural fibre reinforced flame retarded epoxy resin composites. *Polym. Degrad. Stab.* 119 (2015) 68–76.
 30. Pickering KL, Le TM. High performance aligned short natural fibre—Epoxy composites. *Compos. Part B Eng.* 85 (2016) 123–129.
 31. Mittal V, Saini R, Sinha S. Natural fibre-mediated epoxy composites—A review. *Compos. Part B* 99 (2016) 425–435.
 32. Abu Bakar MA, Ahmad S, Kuntjoro W. Effect of epoxidized natural rubber on mechanical properties of epoxy reinforced kenaf fibre composites. *Pertanika J. Sci. Technol.* 20 (2012) 129–137.
 33. Hassan F, Zulkifli R, Ghazali MJ, Azhari CH. Kenaf Fiber Composite in Automotive Industry: An Overview. *Int. J. Adv. Sci. Eng. Inf. Technol.* 7 (2017) 315.
 34. Nurazzi NM, Khalina A, Sapuan SM, Ilyas, R.A. Mechanical properties of sugar palm yarn/woven glass fiber reinforced unsaturated polyester composites: Effect of fiber loadings and alkaline treatment. *Polimery.* 64 (2019) 12–22.
 35. Rihayat T, Suryani S, Fauzi T, Agusnar H, Wirjosentono B, Syafruddin, Helmi, Zulkifli, Alam PN, Sami M. . Mechanical properties evaluation of single and hybrid composites epoxy reinforced bamboo, PALF and coir fiber. *IOP Conf Ser Mater Sci Eng.* 334 (2018) 012081. doi:10.1088/1757-899X/334/1/012081
 36. Wang F, Shao Z. Study on the variation law of bamboo fibers' tensile properties and the organization structure on the radial direction of bamboo stem. *Ind Cros Products.* 152 (2020) 112521.
 37. Mahmoud MA. Oil spill cleanup by raw flax fiber: modification effect, sorption isotherm, kinetics, and thermodynamics. *Arabian J Chem.* 13 (2020) 5553– 5563.
 38. Kang JT, Kim SH. Improvement in the mechanical properties of polylactide and bamboo fiber biocomposites by fiber surface modification. *Macromol Res.* 19 (2011)789–796.
 39. Lee SH, Wang S. Biodegradable polymers/bamboo fiber biocomposite with bio-based coupling agent. *Compos Appl Sci Manuf.* 37 (2006) 80–91.
 40. Fan M. Chemical compositions of natural fibres. In: S. R. Reid, G. Zhou, editors. *Advanced high strength natural fibre composites in construction.* London: Woodhead Publishing, 35–41, 2016.
 41. Fernandes, F. C., Kirwan, K., Lehane, D., & Coles, S. R. (2017). Epoxy resin blends and composites from waste vegetable oil. *European Polymer Journal*, 89, 449–460. <https://doi.org/10.1016/j.eurpolymj.2017.02.005>
 42. Vural K6k, B., Aydođmuş, E., Yilmaz, M., & Akpolat, M. (2021). Investigation on the properties of new palm-oil-based polyurethane modified bitumen. *Construction and Building Materials*, 289. <https://doi.org/10.1016/j.conbuildmat.2021.123152>
 43. Aydođmuş, E., Arslanođlu, H., & Dađ, M. (2021). Production of waste polyethylene terephthalate reinforced biocomposite with RSM design and evaluation of thermophysical properties by ANN. *Journal of Building Engineering*, 44, 103337. <https://doi.org/10.1016/j.jobe.2021.103337>
 44. Mustapha, R., Rahmat, A. R., Abdul Majid, R., & Mustapha, S. N. H. (2019). Vegetable oil-based epoxy resins and their composites with bio-based hardener: a short review. In *Polymer-Plastics Technology and Materials* (Vol. 58, Issue 12, pp. 1311–1326). Taylor and Francis Inc. <https://doi.org/10.1080/25740881.2018.1563119>
 45. Xu Y, Yang Y, Shen R, Parker T, Zhang Y, Wang Z, Wang Q. Thermal behavior and kinetics study of carbon/epoxy resin composites. *Polymer Composites*, 40 (2019) 4530–4546. <https://doi.org/10.1002/pc.25309>
 46. Tikhani F, Moghari S, Jouyandeh M, Laoutid F, Vahabi H, Saeb MR, Dubois P. Curing kinetics and thermal stability of epoxy composites containing newly obtained nano-scale aluminum hypophosphite (AlPO2). *Polymers.* 12 (2020), 1–22. <https://doi.org/10.3390/polym12030644>
 47. Tranchard P, Samyn F, Duquesne S, Est6be B, Bourbigot S. Modelling behaviour of a carbon epoxy composite exposed to fire: Part I-Characterisation of thermophysical properties. *Materials*, 10 (2017) 494. <https://doi.org/10.3390/ma10050494>
 48. Tranchard P, Duquesne S, Samyn F, Est6be B, Bourbigot S. Kinetic analysis of the thermal decomposition of a carbon fibre-reinforced epoxy resin laminate. *Journal of Analytical and Applied Pyrolysis*, 126 (2017) 14–21. <https://doi.org/10.1016/j.jaap.2017.07.002>
 49. Wang R, Xie C, Zeng L, Xu H. Thermal decomposition behavior and kinetics of nanocomposites at low-modified ZnO content. *RSC Advances.* 9 (2019), 790–800. <https://doi.org/10.1039/c8ra09206k>
 50. Xiong X, Zhou L, Ren R, Liu S, Chen P. The thermal decomposition behavior and kinetics of epoxy resins cured with a novel phthalide-containing aromatic diamine. *Polymer Testing.* 68 (2018) 46–52. <https://doi.org/10.1016/j.polymertesting.2018.02.012>
 51. Hassan MZ, Sapuan SM, Roslan SA, Aziz SA, Sarip S. Optimization of tensile behavior of banana pseudo-stem (Musa acuminata) fiber reinforced epoxy composites using response surface methodology. *Journal of Materials Research and Technology*, 8 (2019), 3517–3528. <https://doi.org/10.1016/j.jmrt.2019.06.026>
 52. Sinha AK, Bhattacharya S, Narang HK. Experimental determination and modelling of the mechanical properties of hybrid abaca-reinforced polymer composite using RSM. *Polymers and Polymer Composites*, 27 (2019) 597–608. <https://doi.org/10.1177/0967391119855843>
 53. Oladele IO, Akinola OS, Agbabiaka OG, Omotoyinbo JA. Mathematical Model for the Prediction of Impact Energy of Organic Material Based Hydroxyapatite (HAp) Reinforced Epoxy Composites. *Fibers and Polymers.* 19 (2018), 452–459. <https://doi.org/10.1007/s12221-018-7844-5>
 54. Antil P. Modelling and Multi-Objective Optimization during ECDM of Silicon Carbide Reinforced Epoxy Composites. *Silicon*, 12 (2020) 275–288. <https://doi.org/10.1007/s12633-019-00122-8>
 55. Sinha AK, Narang HK, Bhattacharya S. Experimental Determination, Modelling and Prediction of Sliding Wear of Hybrid Polymer Composites Using RSM and Fuzzy Logic. *Arabian Journal for Science and Engineering*, 46(3), 2071–2082. <https://doi.org/10.1007/s13369-020-04997-3>
 56. Sarafrazi, M., Hamadian, M., & Ghasemi, A. R. (2019). Optimize epoxy matrix with RSM/CCD method and influence of multi-wall carbon nanotube on mechanical properties of epoxy/polyurethane. *Mechanics of Materials*, 138 (2021) 103154. <https://doi.org/10.1016/j.mechmat.2019.103154>
 57. Dadrasi A, Farzi GA, Shariati M, Fooladpanjeh S, Parvaneh V. Experimental study and optimization of fracture properties of epoxy-based nano-composites: Effect of using nano-silica by GEP, RSM, DTM and PSO. *Engineering Fracture Mechanics.* 232 (2020), 107047. <https://doi.org/10.1016/j.engframech.2020.107047>
 58. Wahab, AAA, Chang SH, Som, AM. Characterisation of waste cooking oil as a potential green solvent for liquid-liquid extraction. *International Conference on Advances in Civil and Environmental Engineering*, s. 20–28, 2015.
 59. Lim SF, Hamdan A, Chua SND, Lim BH. Comparison and optimization of conventional and ultrasound-assisted solvent

- extraction for synthetization of lemongrass (*Cymbopogon*)-infused cooking oil. *Food Sci Nutr.* 9 (2021) 2722–2732. DOI: 10.1002/fsn3.2234.
60. El-Aouni N, Hsissou R, El Azzaoui J, El Bouchti M, Elbachiri A, Elharfi A, Rafik M. One-pot Synthesis of Trifunctional Epoxy Resin and its Nanocomposite: Investigation of Thermal and Rheological Properties. *Biointerface Res. Appl. Chem.* 11 (2021) 12403–12413. <https://doi.org/10.33263/BRIAC114.1240312413>
 61. Baxter JN, Cymerman-Craig J, Willis JB. The infrared spectra of some sulphonamides. *J. Chem. Soc.* (1955) 669–679.
 62. Goldstein M, Russell MA, Willis HA. The infrared spectra of N-substituted sulphonamides. *Spectrochim. Acta A.* 25 (1969) 1275–1285.
 63. Reiss A, Cioateră N, Dobritescu A, Rotaru M, Carabet AC, Parisi F, Gănescu A, Dăbuleanu I, Spînu CI, Rotaru P. Bioactive Co(II), Ni(II), and Cu(II) Complexes Containing a Tridentate Sulfathiazole-Based (ONN) Schiff Base. *Molecules* 26 (2021) 3062. <https://doi.org/10.3390/molecules26103062>
 64. Mubarik A, Rasool N, Hashmi MA, Mansha A, Zubair M, Shaik MR, Sharaf MAF, Awwad EM, Abdelgawad A. Computational Study of Structural, Molecular Orbitals, Optical and Thermodynamic Parameters of Thiophene Sulfonamide Derivatives. *Crystals.* 11 (2021) 211. <https://doi.org/10.3390/cryst11020211>

Effect of Fibroblast Growth Factor (FGF) on Some Serum Oxidative Parameters in Hyperglycemic Rats

Esra Oguz¹  Sule Coskun Cevher² 

¹Gazi University, Department of Biophysics, Ankara, Turkey

²Gazi University, Department of Biology, Ankara, Turkey

ABSTRACT

Wound healing is a complex and dynamic process that includes multiple biological pathways and has some successive healing periods. Most growth factor is responsible for wound healing. Fibroblast growth factor has a positive effect on wound healing problems that can be caused by diabetes. In the present study, we aimed to investigate the effect of bFGF applied to dorsolateral incision wounds in hyperglycemic rats on time-dependent serum oxidative events by measuring serum TBARS, NOx and RSH. Experiments were performed on 30 male Wistar albino rats (weight range:170-250 g). Rats were hyperglycemic with streptozotocin (ip, 60 mg/kg). Experimental groups were divided into subgroups with and without treatment according to the days. bGF was applied locally to the dorsolateral wounds of rats (10 ng/ml). After these administrations, on the 3th and 7th days of wound healing, the animals were sacrificed. Serum TBARS, RSH and NOx levels were recorded spectrophotometrically. The results were expressed as mean \pm Standard deviation and the mean differences were compared by Anova Variance Analysis ($p < 0,05$). When compared with the treatment group, on the 7th day and the 3rd day, it was found that the serum TBARS levels increased statistically in hyperglycemic rats ($p < 0,05$). Both in the 3rd day of the untreated and 3rd day of the rats treated with bFGF may significant decrease in the serum RSH levels. bFGF application was found both enhancing and reducing effects on oxidative stress. In subsequent studies, the effect of bFGF, which has positive effects on diabetic wound healing, on oxidative events can be investigated in detail using different doses and different treatment periods.

Keywords:

bFGF; Diabetic wound healing; Free radicals; Oxidative stress; Diabetes mellitus

INTRODUCTION

Repair of tissue damage, loss or deterioration in tissue continuity is one of the most important functions of the organism. The purpose of this repair is to ensure tissue integrity and the function of the damaged organ [1]. The healing of damaged tissue is provided by a regular, in-line of cellular and biochemical chain of events [2, 3].

Wound healing is an evolutionarily preserved complex process aimed at tissue restoration. The wound healing process includes separate but intertwined stages of inflammation, cellular proliferation and maturation and remodeling [4, 5]. Each step; It takes place through the integration of a series of events controlled by endogenous and exogenous factors. This process is regulated by growth factors, cytokines and chemokines [6].

Growth factors are molecules with polypeptide structure that stimulate the growth, differentiation and

proliferation of cells [7, 8]. Studies conducted in recent years have shown that Fibroblast Growth Factor is a large family consisting of 28 members. FGFs produced by keratinocytes, fibroblasts, endothelium, smooth muscle and mast cells have characteristically high binding affinity for both heparin and fibroblast growth factor receptors. Endothelial cells have the ability to both express and respond to FGF [9-11]. bFGF is often used clinically; it has been emphasized that it has a significant effect on wound healing in the skin, cornea, eardrum and salivary glands [12, 13].

Diabetes mellitus (DM) is a metabolic disease that occurs as a result of disorders in insulin secretion as a result of the interaction of genetic, environmental factors, lifestyle changes and events caused by the immune system. It is characterized by hyperglycemia [14, 15]. Inflammation, angiogenesis and collagen synthesis are impaired in diabetes. Blood circulation in the wound area

Article History:

Received: 2021/07/12

Accepted: 2021/09/26

Online: 2021/12/31

Correspondence to: Esra Oguz,
Gazi University, Department of Biophysics,
06500, Ankara, Turkey.
E-Mail: esraoguz28916@gmail.com
Phone: +90 (542) 284 5833

is negatively affected by the angiopathy and neuropathic effects of diabetes. Diabetes is a disease involving peripheral tissue injuries caused by oxidative stress caused by chronic hyperglycemia. Diabetes is known to cause an increase in oxidative stress and inflammatory response. Delayed wound healing is associated with an inflammatory response induced by hyperglycemia. This suggests that the effect of oxidative stress and inflammatory response on wound healing may be positively affected by antioxidant supplementation. Diabetic scar; characterized by a disturbance in the wound healing process, according to animal experiments, a significant decrease in tensile strength was observed, particularly in inflammatory and proliferative phases, pathological angiogenesis and wound healing. Diabetes increases apoptosis of lymphocytes and increases the production of reactive oxygen species, also stimulating the signaling pathway of apoptosis [15-17].

Free radicals affect cellular structures and affect important components such as lipids, proteins, carbohydrates, DNA and enzymes[18]. There are many studies emphasizing the importance of reactive oxygen species in diabetic vascular pathogenesis and showing that diabetic complications are associated with oxidative stress[19].

Oxidative stress, which is one of the causes of diabetes, causes biological problems in wound healing. Considering that the mechanism of action of free radicals on wound healing is not clear, reducing the resulting products will affect the healing process. Many growth factors are effective against free radicals in wound healing. There are studies in which bFGF plays an important role in accelerating healing and biochemically. It is known that bFGF activity is high in the first 3 days of the healing process. However, studies showing the time-dependent effects of bFGF are insufficient. We aimed to measure the positive effect of bFGF, which is used in wound healing and whose doses are tried to be determined, against oxidative stress in the healing process in diabetic rats with biochemical parameters. Therefore, serum TBARS, RSH and NOx levels were measured spectrophotometrically in this study.

MATERIAL AND METHODS

The studies were initiated with the permission of Gazi University Experimental Animals Ethics Committee (G.Ü. ET-15.032) and all stages until the tissue samples were taken in Gazi University Laboratory Animal Breeding and Experimental Research Center (GÜDAM) laboratory. In the experiments, 30 Wistar albino male rats, 170-250 grams, obtained from GÜDAM were used. Before animals fed with free feed and water and during the experiment were looked after in individual cages during the experiment, in an environment illuminated in pa-

rallel with the daylight cycle. Tissue samples taken were analyzed in Gazi University Faculty of Science, Physiology-Biochemistry research laboratory.

bFGF Preparation

In previous studies conducted in our laboratory, the dosage was determined as 10ng / ml, since it was determined histologically that the contribution of bFGF to wound healing at a dosage of 10ng / ml was high. bFGF (10 ng / ml) was applied locally to the wounds of rats in the bFGF applied groups once a day at approximately the same time[20-22].

Diabetes Model

In groups formed to compare wound healing in healthy and diabetic animals, streptozotocin (STZ)(ip, 60 mg / kg) dissolved in 0.1 M citrate buffer (pH 4.5) buffer was administered to diabetic animals[23]. One week later, blood glucose levels were measured with a glucometer and those above 300 mg / dl were considered as having diabetes. In contrast to the experimental animals that were resistant to diabetes, STZ administration was made in a second dose and made diabetic.

Wound Model

In order to prevent infection before the experiment, the dorsal parts of the animals were made ready by applying batticon before the wound was created.

General anesthesia was provided by weighing the experimental animals on a standard scale and injecting ketamine (Alfamanine 50mg / kg) and xylazine (Alfazyne 5mg / kg) intramuscularly according to their weight.

Dorsolateral excisional incision wounds were made on the dorsal of the animals, approximately 4 cm long on both sides of the spine [24-26]. Later, the wound lips were adapted with suture. In order to provide postoperative analgesia, paracetamol, a pharmacological agent, was used as 2 mg / ml into drinking water.

Diabetic Experimental Groups

5 separate experimental groups were formed, 6 in each group, and the following procedures were applied to the groups.

Hyperglycemic control group: In order to compare the values of the groups formed, only STZ and diabetic control group (n = 6)

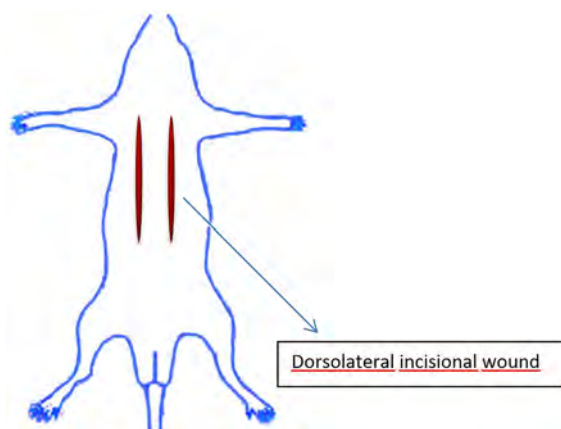


Figure 1. Incisional wound model

Hyperglycemic untreated groups: After being diabetic with STZ, only the wounded group (3rd day of healing was sacrificed) (n = 6) After being diabetic with STZ, only the wounded group (7th day of healing was sacrificed) (n = 6)

Hyperglycemic bFGF treated groups: The group that was wounded after being diabetic with STZ and applied bFGF (3rd day of recovery was sacrificed) (n = 6) The group that was wounded after being diabetic with STZ and applied bFGF (7th day of recovery was sacrificed) (n = 6)

After the applications, the rats were sacrificed by taking blood from their hearts on the 3rd and 7th days in accordance with the chronobiological order. The blood samples taken were centrifuged at 3000 rpm for 15 minutes and the serums were taken into ependof tubes and stored at -30°C until analyzed.

Biochemical Analyses

Determination of TBARs Levels

The determination of MDA, which is the indicator of lipid peroxidation, was made by the method of thiobarbituric acid reactive substance (TBARS) formation using Kurtel method [27]. The solutions used are 15% TCA, 0.02% BHT (in 95% ethanol), 0.375% TBA and 0.25 N HCl. 400 μ L of TBA-TCA-HCl mixture (in equal amounts) was added onto 200 μ L of plasma and vortexed. After being kept at room temperature for 5 minutes, it was centrifuged at 10000 rpm for 5 minutes. The entire supernatant obtained was placed in glass tubes. After adding 4 μ L of BHT to the supernatants, the tubes were boiled for 15 minutes. After cooling in tap water, it was placed in an ELISA plate and read at a wavelength of 532 nm.

Determination of RSH Levels

Determination of plasma total sulfhydryl groups (RSH), which is an indicator of antioxidant capacity, was made

by spectrophotometric method [27]. The solutions used are the mixture containing 10 mM DTNB, 100 mM Tris-HCl (pH 8.2), 1% SDS-2 mM EDTA in 0.1 M potassium phosphate buffer (pH: 7). 1 mL of Tris-SDS-EDTA mixture was added to 500 μ L sample. It was incubated for 5 minutes at room temperature, and then centrifuged at 10000 rpm for 5 minutes. 40 μ L DTNB was added to the obtained supernatant. After being kept at 37 °C for 20 minutes, it was read at 412 nm wavelength on the ELISA reader.

Determination of Total NOx Levels

The modified Griess method was used for the determination of NOx, which is the sum of plasma nitrite and nitrate[28]. 0-50 μ M dilutions of sodium nitrate (NaNO_3) prepared with deionized water were used as standard. 0.3 N NaOH was completed to 100 ml by adding deionized water to 1.2 g of NaOH. 10% ZnSO_4 is completed to 100 ml by adding deionized water on 10 g of ZnSO_4 . VaCl_3 4.2 ml HCl was added to 0.4 g VaCl_3 and this mixture was completed to 50 ml with deionized water. Sulfanamide 2 gr sulfanamide 13.6 ml HCl was added and this mixture was completed to 100 ml with deionized water. -NEDD (N- (1-naphtyl) ethylenediamide dihydrochloride) was completed to 100 ml by adding deionized water on 0.1 gr NEDD. 100 μ L 0.3 M NaOH was added to 100 μ L plasma and incubated for 5 minutes at room temperature. 100 μ L of 10% ZnSO_4 was added to this mixture and vortexed. The resulting mixture was centrifuged at +4°C at 14000 rpm. 100 μ L of each of the supernatants obtained after centrifugation was placed on a 96-well ELISA plate. The samples were placed on the plate in duplicate with the same volume of standard solutions. 100 μ L of VaCl_3 was added to all samples and standard solutions, followed by 50 μ L of sulfanamide and 50 μ L of NEDD. The plate was incubated at 37°C for 30 minutes. At the end of the incubation it was read on an ELISA reader at a wavelength of 540 nm.

Statistical Evaluation

All values are expressed as arithmetic mean \pm standard error. The values obtained were evaluated using Anova analysis of variance (one-way ANOVA) and Tukey multiple comparison test (SPSS 16.0 for Windows (SPSS, Inc., Chicago, USA). P value of <0.05 was considered statistically significant.

RESULTS

Morphological images of the wounds belonging to the untreated and treated groups of hyperglycemic rats and their changes depending on the days, blood samples ta-

ken are shown in Figures 2, 3, 4 and 5.

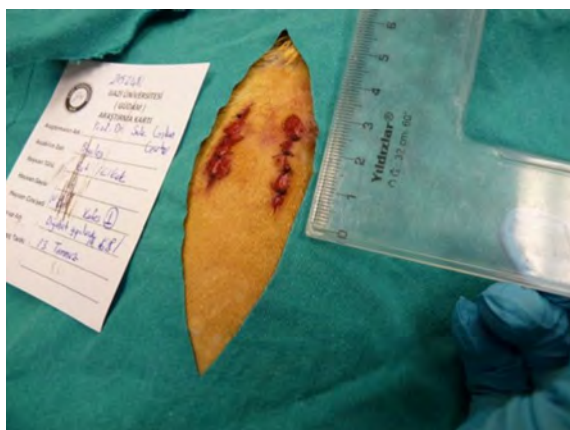


Figure 2. Dorsolateral incisional wound



Figure 3. Morphological image of hyperglycemic 3-day untreated and bFGF 3-day treated wounds



Figure 4. Morphological image of hyperglycemic 7-day untreated and 7-day bFGF-treated wounds



Figure 5. Taking blood samples

Findings of the oxidative parameters of TBARS, RSH and NOx in the control group, treated and untreated groups in hyperglycemic rats are shown in Table 1.

Serum TBARS Levels in Hyperglycemic Rats

TBARS level is measured to determine malondialdehyde, the final product of lipid peroxidation. When the 7 days untreated and treated groups were compared with the control group, a significant increase was observed ($p < 0.05$) (Table 1 and Figure 6). Serum TBARS levels statistically increased on the 7th day compared to the 3rd day in hyperglycemic rats treated with bFGF ($p < 0.05$) (Table 1 and Figure 6).

Serum RSH Levels in Hyperglycemic Rats

When the 7th day of the bFGF applied rats and the 7th day of the untreated group were compared, a significant decrease was detected ($p < 0.05$) (Table 1 and Figure 7)

It was observed that the RSH levels in rats treated with bFGF decreased compared to the 3rd and 7th days. ($p < 0.05$) (Table 1 and Figure 7). Both in the 3rd day of the untreated

Table 1. Serum TBARS, RSH and NOx levels in hyperglycemic rats

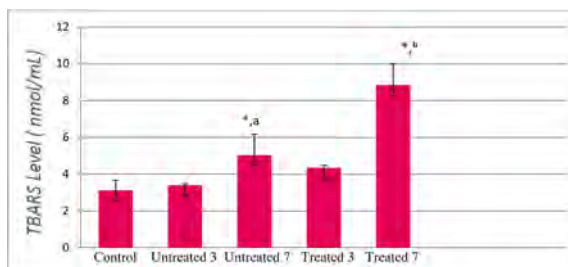
Groups	T B A R S (nmol/mL)	RSH (nmol/mL)	NOx ($\mu\text{mol/L}$)
Control (n=6)	3,12 \pm 0,56	135,43 \pm 28,28	180,24 \pm 9,95
U n t - r e a t e d (n=12)	3 Days (n=6)	183,21 \pm 3,4	121,92 \pm 14,21 [*]
	7 days (n=6)	152,88 \pm 14,38 ^a	92,68 \pm 6,42 ^a
bFGF t r e a - t e d (n=12)	3 Days (n=6)	128,65 \pm 6,06	173,87 \pm 6,02 [*]
	7 days (n=6)	123,79 \pm 7,76 ^{b,c}	151,22 \pm 23,95 ^a

*: $p < 0.05$: Compared with the control group

a: $p < 0.05$: Comparison of 3 days untreated group and 7 days untreated group

b: $p < 0.05$: 3 days treatment group compared to 7 days treatment group

c: $p < 0.05$: Comparison of 7 days untreated group and 7 days treated group

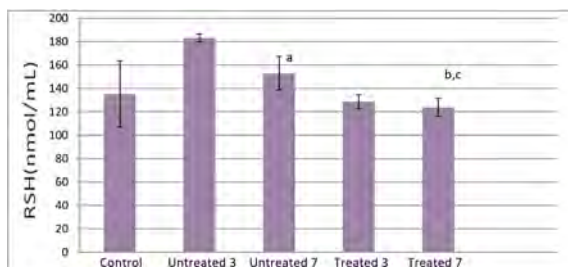


* $p < 0.05$ When compared with the control group

a $p < 0.05$ 3-day untreated group compared

b $p < 0.05$ 3-day treatment group compared

c $p < 0.05$ 7 days without treatment group compared

Figure 6. Serum TBARS (nmol / mL) levels in hyperglycemic rats

* $p < 0.05$ When compared with the control group

a $p < 0.05$ 3-day untreated group compared

b $p < 0.05$ 3-day treatment group compared

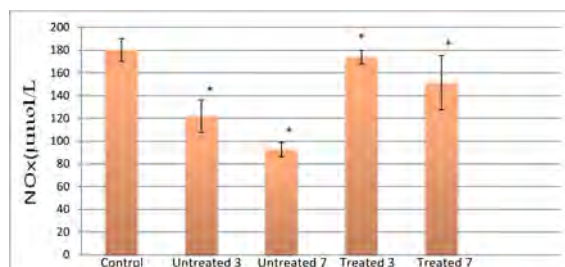
c $p < 0.05$ 7 days without treatment group compared

Figure 7. Serum RSH (nmol / mL) levels in hyperglycemic rats

and 3rd day of the rats treated with bFGF may significant decrease in the serum RSH levels.

Serum NOx Levels in Hyperglycemic Rats

A statistically significant increase was found in rats treated with hyperglycemic bFGF when compared with the NOx levels of the 3rd day of wound healing and the same day of the untreated group ($p < 0.05$). Nitric oxide levels increased with the bFGF treatment we applied. When all groups were compared with the control, a statistically significant difference was found ($p < 0.05$) (Table 1 and Figure 8).



* $p < 0.05$ When compared with the control group

a $p < 0.05$ 3-day untreated group compared

b $p < 0.05$ 3-day treatment group compared

c $p < 0.05$ 7 days without treatment group compared

Figure 8. Serum levels of NOx ($\mu\text{mol} / \text{L}$) Levels in hyperglycemic rats

DISCUSSION

Free radicals affect organic compounds as a result of oxidative reactions and cause various biological problems [29]. The oxidative balance is disturbed when an increase in the rate of radical formation or a decrease in the rate of their removal is observed. Oxidative stress may reduce the effect of antioxidants and cause tissue damage. With the oxidative stress that occurs, the effect of antioxidants may decrease, resulting in tissue damage [30].

It can be said that bFGF significantly reduces oxidative stress and plays an important role in suppressing this damage.

The research is limited to the bFGF treatment applied to rats by the researchers and the data obtained biochemically. Çetin et al. (2004) pointed out that bFGF has a scavenging effect on free radicals that occur with respiratory burst, which is effective in the inflammatory phase of wound healing [31]. The production of H_2O_2 and ROS in the inflammatory process in the wound area causes increases in the TBARS level. Inflammatory responses are required for wound repair following injury [32]. In our current findings, the negative effect of diabetes, lipid peroxidation in hyperglycemic rats with bFGF application could not be eliminated. The reason for this can be shown as increased oxidative stress due to diabetes. bFGF has a very short biological half-life (2-3 min). It can be rapidly removed from the blood when injected. For this reason, suitable systems such as controlled release systems should be used to increase the release time and eliminate its undesirable effects [31]. Wei et al. (2009) emphasized in their research that the FGF family shows antioxidant properties in conditions related to oxidative stress [33]. In our experiment, the high TBARS levels in the treated 7-day group indicate that bFGF in serum did not have an antioxidant effect. Due to the strong link between diabetes and free radicals in the studies, it can be said that bFGF application against free radicals should be done at a more appropriate dose. In addition, it is necessary to provide long-term release of bFGF to increase the in vivo efficacy.

There are antioxidant systems that protect the body against free radical damage at many stages. Antioxidants are negatively affected by the oxidative stress caused of free radicals. Antioxidants used to prevent the effect of free radicals, especially thiol groups, can't protect the plasma and tissue levels due to interactions [34]. All plasma -SH groups are associated with proteins. With the increasing oxidative stress, -SH groups found in plasma and membranes are oxidized by free radical effect and a decrease in their reduced form is detected. GSH is required for the oxidized thiol groups to become reduced again and to be used in oxidative damage. While GSH neutralizes thiol groups affected by oxidative stress, it falls short[34, 35]. Both in the 3rd day of the untreated and 3rd day of the rats treated with bFGF may significant decrease in the serum RSH levels. The decrease in RSH levels of treated diabetes groups compared to untreated diabetes groups is that plasma proteins may be sensitive to bFGF, especially due to free sulfhydryl groups in the serum albumin structure. The molecular structure of bFGF could not positively affect the oxidative stress that increases with diabetes.

Nitric oxide levels increased with the bFGF treatment we applied. Topical application of bFGF decreased NOx levels and nitrite oxide synthase enzyme was suppressed. In the light of this information, bFGF application in diabetic rats contributed to wound healing systemically. NO is an endothelium-derived vasodilator agent and plays an active role in lowering blood pressure. It is one of the important molecules in the wound healing process. While it has a protective effect at physiological doses, it can show a cytotoxic effect at high levels [30]. NO is rapidly metabolized to nitrite and nitrate by interacting with the Hem group of hemoglobin in the blood. NO also reacts with heme and other iron-containing molecules, and with thiol (-SH) groups of proteins [36]. A statistically significant increase was found in rats treated with hyperglycemic bFGF when compared with the NOx levels of the 3rd day of wound healing and the same day of the untreated group ($p < 0.05$). In hyperglycemic rats, there was an increase in NO production due to the increased leukocyte activation during the inflammation phase of wound healing and its effect preventing leukocyte outflow. The decrease in nitrite oxide production in the endothelium has been blamed for the disorders of endothelial functions seen in diabetes, although controversial [37]. However, there are also studies showing that NO is increased in diabetes [38].

CONCLUSION

It can be said that bFGF significantly reduces oxidative stress and plays an important role in suppressing this damage. In this study, information about how bFGF, which is known to have an effect on wound healing, mana-

ges oxidative events was tried to be clarified. When all the information is evaluated, our study has shown that bFGF applied to dorsolateral incision wounds created in hyperglycemic rats has a regulatory effect on serum levels of oxidative events. It has been shown that this effect may vary depending on the days, the stages of wound healing and the dose administered. In subsequent studies, the effect of bFGF, which has positive effects on diabetic wound healing, on oxidative events can be investigated in detail by using different doses and different treatment times.

ACKNOWLEDGEMENT

This study was supported by a research grant from TÜ-BİTAK (215Z482).

CONFLICT OF INTEREST

Esra Oguz confirms, on behalf of all authors, that the information provided is accurate.

AUTHOR CONTRIBUTION

Esra Oğuz and Sule Coskun Cevher designed the study. EO performed all experiments. EO and SCC analysed the data. EO and SCC wrote the paper.

References

1. Yüceyar, S., Cerrahi Yaraların Takip ve Tedavisi. Yara Bakımı ve Tedavisi., İÜ Cerrahpaşa Tıp Fakültesi Sürekli Tıp Eğitimi Etkinlikleri. (2008) p. 17.
2. Lazarus, G.S., et al., Definitions and guidelines for assessment of wounds and evaluation of healing. *Wound repair and regeneration*, (1994). 2(3): p. 165-170.
3. Barrientos, S., et al., Growth factors and cytokines in wound healing. *Wound Repair and Regeneration*, (2008). 16(5): p. 585-601.
4. Karasu, A. and B. Bakır, Yara ve yara iyileşmesi. *Veteriner Cerrahi Dergisi*. (2008) . 36-43.
5. Taşır, S., Ekzojen epidermal büyüme faktörü'nün tükürük bezi oksidan olaylarına zaman bağımlı etkisi. *Fen Bilimleri Enstitüsü. Gazi Üniversitesi*. 2007.
6. Takayama, Y. and R. Aoki, Roles of lactoferrin on skin wound healing. *Biochemistry and Cell Biology*. (2011). 90(3): p. 497-503.
7. Anusaksathien, O. and W.V. Giannobile, Growth factor delivery to re-engineer periodontal tissues. *Current Pharmaceutical Biotechnology*. (2002). 3(2): p. 129-139.
8. Lee, S.J., Cytokine delivery and tissue engineering. *Yonsei Medical Journal*. (2000). 41(6): p. 704-719.
9. Ornitz, D.M. and N. Itoh, Fibroblast growth factors. *Genome Biology*. (2001). 2(3): p. 1-12.
10. Casey-Sawicki, K., et al., A basic fibroblast growth factor analog for protection and mitigation against acute radiation syndromes. *Health Physics*. (2014). 106(6): p. 704- 712.
11. Teven, C.M., et al., Fibroblast growth factor (FGF) signaling in development and skeletal diseases. *Genes & Diseases*. (2014). 1(2):

- p. 199-213.
12. Özbek, Z. and Vural M., Kranial Sütürlerin Biyolojisi, Sütür Büyüme, Gelişme ve Kapanmasının Regülasyonu. *Türk Nöroşirürji Dergisi*. (2017). 27(3): p. 245-250.
 13. Kobayashi, F., K. Matsuzaka, and T. Inoue. The effect of basic fibroblast growth factor on regeneration in a surgical wound model of rat submandibular glands. *International Journal of Oral Science*. (2016). 8(1): p. 16-23.
 14. Özler, M., et al., Pinealektomili ratlarda yara iyileşmesi. *Gulhane Medical Journal*. (2010). 52: p. 181-184.
 15. Brogard, J., T. Vetter, and J. Blickle, Discovery of pancreatic diabetes in Strasbourg. *Diabete & Metabolisme*, (1992). 18(2): p. 104-114.
 16. Baynes, J.W. and S.R. Thorpe, Role of oxidative stress in diabetic complications: a new perspective on an old paradigm. *Diabetes*. (1999). 48(1): p. 1-9.
 17. Dandona, P., et al., Oxidative damage to DNA in diabetes mellitus. *The Lancet*. (1996). 347(8999): p. 444-445.
 18. Aslan, D., Onat, T., Emerk, K. And Sözmén, E. Y, İnsan Biyokimyası, second edition, Ankara: Palme Publishing, 2006.
 19. Pitocco, D., et al., Oxidative stress, nitric oxide, and diabetes. *The Review of Diabetic Studies: RDS*. (2010). 7(1): p. 15.
 20. Hu, C., et al., Basic fibroblast growth factor stimulates epithelial cell growth and epithelial wound healing in canine corneas. *Veterinary Ophthalmology*. (2009). 12(3): p. 170-175.
 21. Xie, J., et al., Effects of basic fibroblast growth factor on the expression of extracellular matrix and matrix metalloproteinase-1 in wound healing. *Clinical and Experimental Dermatology: Continuing professional development (CPD)*, (2008). 33(2): p. 176-182
 22. Erarslan, S., Bazik fibroblast büyüme faktörü uygulamasının yara dokusu oksidan olaylarına etkisi, *Biyoloji Anabilim Dalı*. Gazi Üniversitesi. (2019).
 23. Alimohammadi S, Hobbenaghi R, Javanbakht J, Kheradmand D, Mortezaee R, Tavakoli M, Khadivar F, Akbari H. Protective and antidiabetic effects of extract from *Nigella sativa* on blood glucose concentrations against streptozotocin (STZ)-induced diabetic in rats: an experimental study with histopathological evaluation. *Diagn Pathol*. (2013) Aug 15;8:137.
 24. Masson-Meyers, D.S., et al., Experimental models and methods for cutaneous wound healing assessment. *Int J Exp Pathol*, (2020). 101(1-2): p. 21-37.
 25. Laila, L., et al., Wound healing effect of Haruan (*Channa striatus*) spray. *International Wound Journal*, (2011). 8(5): p. 484-491.
 26. Gökşen, S., Diyabetik ratlarda topikal trombosit kökenli büyüme faktörü'nün yara dokusu oksidatif olayları üzerine etkisinin incelenmesi, *Fen Bilimleri Enstitüsü. Gazi Üniversitesi*. (2014).
 27. Kurtel, H., et al., Vulnerability of intestinal interstitial fluid to oxidant stress. *American Journal of Physiology-Gastrointestinal and Liver Physiology*. (1992). 263(4): p. G573-G578.
 28. Miranda, K.M., M.G. Espey, and D.A. Wink, A rapid, simple spectrophotometric method for simultaneous detection of nitrate and nitrite. *Nitric Oxide*. (2001). 5(1): p. 62-71.
 29. Aydemir, B. and E.K. SARI, Antioksidanlar ve büyüme faktörleri ile ilişkisi. *Kocatepe Veterinary Journal*, (2009). 2(2): p. 56-60.
 30. Altan, N., Dinçel, A. S., and Koca, C., Diabetes Mellitus ve Oksidatif Stres. *Türkiye Biyokimya Dergisi*, (2006). 31 (2): 51-56.
 31. Çetin, M. and Y. Çapan, bFGF Bazik Fibroblast Büyüme Faktörü ve Formülasyonlarında Yeni Yaklaşımlar. *Hacettepe University Journal of the Faculty of Pharmacy*, (2004). (2): p. 107-124.
 32. Rajasekaran, N., et al., The effect of finger millet feeding on the early responses during the process of wound healing in diabetic rats. *Biochimica et Biophysica Acta (BBA)- Molecular Basis of Disease*, (2004). 1689(3): p. 190-201.
 33. Wei, W., et al., Oxidative stress, diabetes, and diabetic complications. *Hemoglobin*. (2009). 33(5): p. 370-377.
 34. Yazıcı, A.E et al., Tip II Diabetes Mellituslu Hastalarda Plazma Total Tiyoil ve Eritrosit Redükte Glutasyon Düzeyleri. *T Klin J Med Sci* (2002). 487-492.
 35. Hu, M. L. [41] Measurement of protein thiol groups and glutathione in plasma. *Methods in enzymology*, (1994). 233, 380-385.
 36. Karabağ, F., Deneysel Olarak Hipertiroidizm Olusturulan Ratlarda Kafeik Asit Fenetil Ester'in Plazma Homosistein, Asimetrik Dimetil Arjinin, Nitrik Oksit ve Lipid Profili Üzerine Etkilerinin Araştırılması. *Sağlık Bilimleri Enstitüsü. Afyon Kocatepe Üniversitesi*. (2010).
 37. Chin, Gloria A., Robert F. Diegelmann, and Gregory S. Schultz. Cellular and molecular regulation of wound healing. *Basic and Clinical Dermatology*. 33 (2005): 17.
 38. Memişoğulları, R., Diyabette serbest radikallerin rolü ve antioksidanların etkisi. *Duzce Medical Journal*, 2005. 7(3): p. 30-39.

Evaluation of the Cytotoxic Effects of Ultrasonic Extracts of *Tribulus Terrestris* L. on MCF-7 Cell Line by MTT Assay

Giray Bugra Akbaba¹  Füreyâ Elif Ozturkkan²  Mustafa Sertcelik² 

¹Kafkas University, Department of Bioengineering, Kars, Turkey

²Kafkas University, Department of Chemical Engineering, Kars, Turkey

ABSTRACT

People, especially those living in rural environments and those who have recently been dissatisfied with traditional medicine, use medicinal plants for their therapeutic effects. In this study, ethanol, ethyl acetate and methanol extracts of *Tribulus terrestris* L. plant, which is used by local people as one of these medicinal plants in Kars province (Turkey), were obtained by ultrasound assisted extraction method. The cytotoxic effects of the obtained extracts on MCF-7 breast cancer cells in the concentration range of 10-1000 ppm at 24 h of exposure were investigated by the MTT method, which is a colorimetric method. *T. terrestris* L. ethanol extracts at 1000 ppm caused a moderate cytotoxic effect on MCF-7 breast cancer cells. It was determined that ethanolic extracts in the concentration range of 10-500 ppm and methanol and ethyl acetate extracts in the concentration of 10-1000 ppm caused cell proliferation.

Keywords:

Tribulus Terrestris L.; MCF-7; Ultrasound assisted extraction; Cytotoxicity; MTT Assay

INTRODUCTION

It is known that human beings used only natural medicines until 1800 in the treatment of diseases. Compounds obtained through isolation from natural sources since the beginning of 1800 have been synthesized in the laboratory environment since 1830 [1]. In recent years, the belief that natural remedies are safer than synthetic drugs have led to an increase in people's use of natural products such as herbs, phytotherapeutics and phytopharmaceuticals. Therefore, researchers conduct various studies on the biological significance of plant extracts [2, 3]. However, there is no regulatory system that determines the safety and required dose of natural products, or even commercially sells them. The most widely used of these natural products are herbs. Unfortunately, most of those who use these herbs therapeutically do not have adequate knowledge or training in the safe use of the products. For these reasons, many studies are required to standardize natural plant products and evaluate possible risks such as undesirable side effects, overdose and toxicity [4].

Tribulus terrestris L. is known in Turkey as “deve çökerten”, “çoban çökerten” and “çarık diken”. These names were given to the plant because its fruit has horn-shaped spikes (Figure 1). The plant is of medicinal

and pharmaceutical interest due to its steroidal saponin content [5, 6]. *Tribulus terrestris* L., in addition to its hypolipidemic and hypoglycemic effects, is also used for the treatment of vitiligo, urological infections, prostatic hypertrophy, eye, abdomen and cardiovascular system diseases [6-8]. There are limited in vitro studies on the effect of *T. terrestris* L. extracts [7], which have low cytotoxicity on normal cells, on different cancer cells [7, 10-12]. In this context, in this study, the cytotoxic effects of ethanol, ethyl acetate and methanol extracts of *Tribulus terrestris* L. on MCF-7 human breast cancer cell line for 24 hours were investigated by MTT Assay.

MATERIAL AND METHODS

Collection of Chemicals and Plant Material

Ethanol, ethyl acetate, methanol, DMSO, MTT, DMEM, Penicillin-Streptomycin, Fetal Bovine Serum (FBS), Phosphate Salt Buffer (PBS) and Trypsin EDTA (Sigma Aldrich, Germany) were commercially available. *Tribulus terrestris* L. aerial parts (leaf, fruit and stem) were collected from Kars, Turkey at the altitude of 1410 m at 40°29'46" North and 43°33'40" East coordinates. Map views related to these coordinates were obtained from Google Earth online and were gi-

Article History:

Received: 2021/07/16

Accepted: 2021/11/20

Online: 2021/12/31

Correspondence to: Füreyâ Elif Ozturkkan,
Kafkas University, Department of Chemical
Engineering, 36100, Kars, Turkey.
E-Mail: fozturkkan36@gmail.com
Phone: +90 (535) 652 2105
Fax: +90 (474) 225 1160



Figure 1. *Tribulus terrestris* L. plant

ven in Figure 2. The collected plant was described by Prof. Dr. Fatma Güneş. The collected plant samples were dried in the dark and ground using a grinder.



Figure 2. Map view of 40°29'46" North, 43°33'40" East coordinates where *Tribulus terrestris* L. samples were collected

Instruments

In this study, Bandelin Sonorex RK 106 at 35 kHz frequency, Panasonic MCO-170AICUVH-PE CO₂ Incubator, Hed Lab X BIO MSC CLASS II Biosafety cabinet, Thermo Fisher EVOS FL Inverted Microscope and BioTek Epoch UV-Vis Spectrophotometer were used.

Plant Extraction

For ultrasound assisted extraction, 10 g from the milled plant sample was weighed and placed in the round-bot-

tom flask, then added in a 30 mL the extraction solvent (ethanol, ethyl acetate and methanol). Extraction was continued 60 min. Temperature was measured at 15 minutes intervals. The obtained extracts were filtered with blue band filter paper and the liquid part was dried in a rotary evaporator. For the MTT test, a stock solution of 1000 ppm was prepared and other solutions (500, 250, 100, 10 ppm) were prepared from this stock solution.

MTT Assay

100 μ L (~5000 cells/well) of MCF-7 cell suspension prepared according to protocols [13] was placed in each well of 96-well plates and incubated for 24 h. After incubation, 100 μ L aliquots from prepared solution (1000, 500, 250, 100 and 10 ppm) were added to the wells (100 μ L of medium + 100 μ L of cell suspension was added to the control wells) and allowed to incubate again for 24 h. Then, 10 μ L of MTT (5 mg/mL) solution prepared in PBS was added to each well and incubated for 4 h. In order to dissolve the formed purple colored formazan crystals, 100 μ L of DMSO was added to all wells and incubated at 18 h. After this period, absorbances were measured at a wavelength of 570 nm with a microplate spectrophotometer. Cell viability percentages were calculated with the following equation 1. All experiments were performed in triplicate.

$$\text{Cell Viability (\%)} = \frac{\text{Absorbance of test well}}{\text{Absorbance of control well}} \times 100 \quad (1)$$

RESULTS AND DISCUSSION

Extraction

Ultrasound assisted extraction is an important technology for green chemistry. The extraction process, which takes hours or days with traditional methods, can be completed in a short time thanks to ultrasound wave-assisted extraction. The most important advantages of this extraction method are short duration, high reproducibility, low solvent consumption and high purity of the final product [14, 15]. The temperatures were recorded as 24 °C, 29 °C, 34 °C and 38 °C (for ethanol); 25 °C, 36 °C, 42 °C and 44 °C (for ethyl acetate) and 26 °C, 32 °C, 38 °C and 39 °C (for methanol) at 15, 30, 45 and 60 minutes, respectively. The yields of extraction were found to be 45.25 % for ethanol, 52.39 % for ethyl acetate and 62.64 % for methanol.

FT-IR Spectroscopy

In many studies, it has been reported that ethanol, ethyl acetate and methanol extracts of the *Tribulus terrestris*

L. plant are quite rich in terms of phenolic acids, flavonoids and saponins [16, 17]. The biological activity of the plant is also attributed to these components. Dinchev et al. reported that there are saponins such as protodioscin, prototribestin, pseudoprotodioscin, dioscin, tribestin, tribulosin, rutin in the ethanolic extracts of the TT plant collected from Turkey [17]. Li et al also determined that the plant contains tigogenin, gitogenin, hecogenin and neohecogenin [18]. Reshma et al. attributed the antioxidant activity of ethyl acetate extracts of the plant to the total phenolic substance content and reported that it contains caffeic acid, chlorogenic and 4-hydroxybenzoic acid phenolic acids [19]. Phenolic compounds such as α -Amyrin as the major component and 3,7,11,1-tetramethyl 2-hexadecen 1-01, n-hexadecanoic acid, hexadecanoic acid, ethyl ester, phytol, 1,2-octadecadienoic acid, 9,12,15-octadecanoic acid, benzenedicarboxylic acid and diisooctyl ester as the minor component have been reported in the methanolic extracts of the plant [20]. In another study, it was determined that the methanolic extracts of the plant contain flavanoids such as naringin, rutin, hyperoside, quercetrin, quercetin, naringenin, hesperetin, campferol and apigenin, as well as phenolic acids such as pyrogallol, gallic acid, protocatechuic acid, catechin, catechol, chlorogenic acid, p-hydroxybenzoic acid, caffeic acid, vanillic acid, ferulic acid, salicylic acid, ellagic acid, coumaric acid and cinnamic acid [21]. These compounds generally have functional groups such as O-H, C-H (aromatic), C-H (aliphatic), C=O, C=C, C-H bending and C-H belonging to substituted benzene rings vibrations. When the FT-IR spectrums of the obtained extracts are examined, the vibrations of the O-H groups are seen in the range of 3500-3200 cm^{-1} . C-H stretching (aromatic), C-H bending (aliphatic) and C-H bending (substitue benzenes) vibrations are observed in the 3100-2900 cm^{-1} , 2900-2800 cm^{-1} and 850-700 cm^{-1} regions, respectively. The vibrations of the C=O group are observed at 1750-1650 cm^{-1} (Figure 3-5).

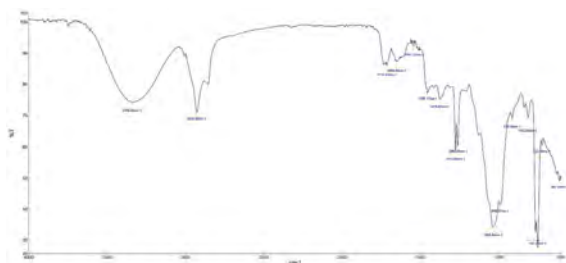


Figure 3. FT-IR spectra of ethanol extract of *Tribulus Terrestris* L.

MTT Assay

In this study, compared with the cell control group, it was determined that *Tribulus terrestris* L.'s methanol extracts caused proliferation of MCF-7 cells at all concentrations.

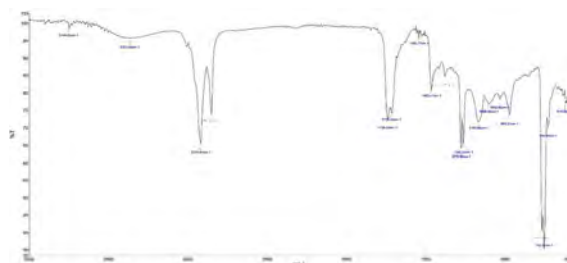


Figure 4. FT-IR spectra of ethyl acetate extract of *Tribulus Terrestris* L.

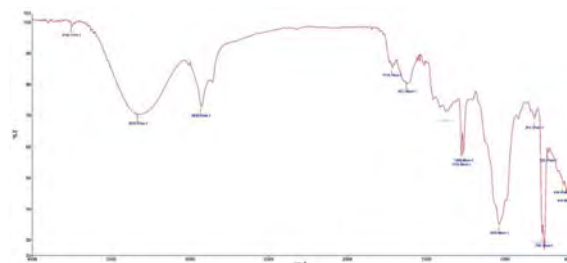


Figure 5. FT-IR spectra of methanol extract of *Tribulus Terrestris* L.

It was determined that cell proliferation increased with decreasing concentration. While 12 % cell proliferation occurred at 1000 ppm concentration, cell viability doubled (210 %) at 10 ppm concentration. Methanol used as a solvent caused 5 % cytotoxicity on MCF-7 cells (Figure 6).

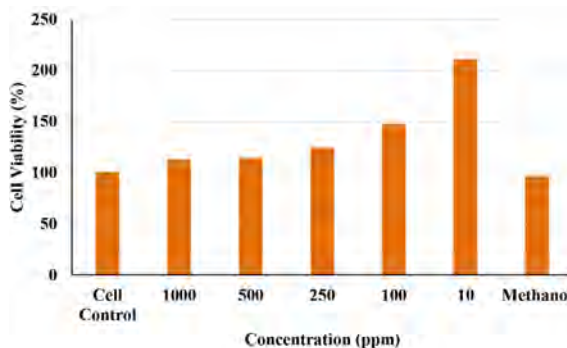


Figure 6. Effect of *Tribulus terrestris* L.'s methanol extract on MCF-7 cell line

The ethanolic extract of *Tribulus terrestris* L. at 1000 ppm concentration caused 19.9 % cytotoxicity. *Tribulus terrestris* L. extracts at 500 ppm, 250 ppm, 100 ppm and 10 ppm concentrations caused proliferation in MCF-7 cells. While proliferation increased with decreasing concentration, more cell viability was found from the methanolic extracts of the plant. Ethanol used as a solvent also increased cell viability by 10 % (Figure 7).

The effects of *Tribulus terrestris* ethyl acetate extracts on MCF-7 are similar to its methanol extracts. That is, the cell viability percentages are similar. 10 % cell viability was found at 1000 ppm concentration and 230 % cell viability at 10 ppm concentration. Ethyl acetate, which was used as a solvent, caused 9.3% moderately cytotoxic [33] on MCF-7 cells (Figure 8). Comparison of effect of the all extracts on

MCF-7 cell viability was given in Figure 9.

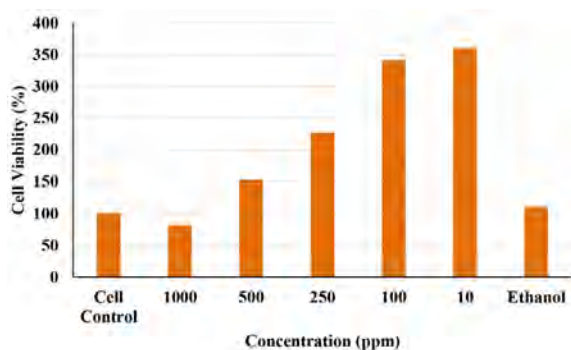


Figure 7. Effect of *Tribulus terrestris* L.'s ethanol extract on MCF-7 cell line

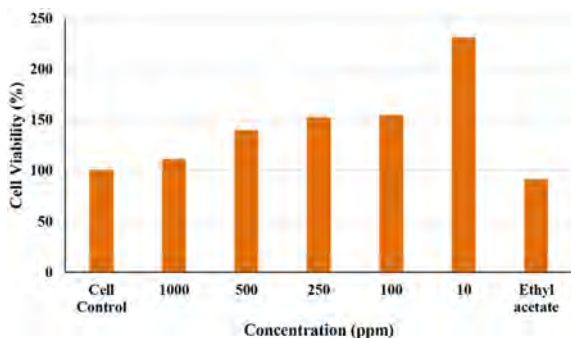


Figure 8. Effect of *Tribulus terrestris* L.'s ethyl acetate extract on MCF-7 cell line

Ammar et al (2018) reported that methanol and petroleum ether extracts of *T. terrestris* L. were cytotoxic to human hepatocellular carcinoma cells (HepG2) at 16.1 $\mu\text{g}\cdot\text{mL}^{-1}$ and 21.5 $\mu\text{g}\cdot\text{mL}^{-1}$ concentrations [21]. Angelova et al. (2013) examined the cytotoxic effects of *T. terrestris* extract on cell viability in human breast cancer (MCF-7) and normal (MCF10A) cell lines. It was determined that this plant extract inhibited the viability of breast cancer cells in a concentration-dependent manner (IC_{50} =15 mg/mL) [7]. Similarly, Neychev et al. (2007) found that the obtained saponins from *T. terrestris* exhibited low toxicity to normal human fibroblasts than some cancer cells [9]. Sun et al. reported that saponins isolated from the of *T. terrestris* L.'s ethanolic extract inhibited the proliferation of Bcap-37 breast cancer cell line and showed a cytotoxic effect on BEL-7402 cell line by causing apoptosis [10, 12]. Wang et al. reported that steroidal saponins isolated from the *T. Terrestris* L.'s fruits exhibited antitumor property on NCI-H460, SF-268, MCF-7 and HepG2 tumor cells [22]. Abudayyak et al. examined the cytotoxicity of NRK-52E cells exposed to *T. terrestris*'s methanol extracts for 24 hours by MTT assay. It was found that cell viability was 68.5 % at 500 mg/mL concentration. The IC_{50} value was determined as 160 mg/mL. It was determined that water and chloroform extracts of this plant did not show cytotoxic effects in the concentration range of 62.5-500 ppm [23]. Chauhan et al. obtained the extracts of *T. Terrestis* fruits by mixing method in ethanol:water (1:1) solvent

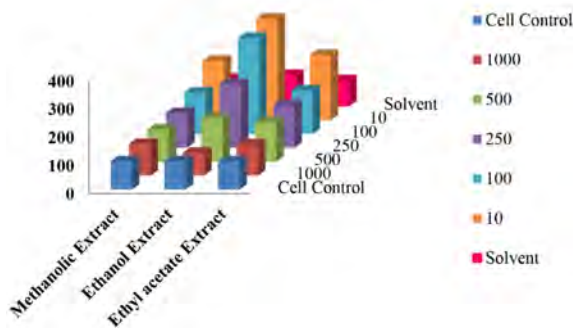


Figure 9. Comparison of effect of the all extracts on MCF-7 cell viability

mixture for 24 h. Researchers examined the effects of the extracts on HCT-15 cells in the concentration range of 10-70 ppm and found that the cells proliferated at 10 and 20 ppm. At 40-70 ppm, the cell viability was found as 25 %. They determined that cytotoxicity increased with increasing concentration [24]. In another study, the water:methanol (1:4) extracts of the fruits of the plant were obtained by the Soxhlet method. The effects of plant extracts on colon cancer cells (HT29) and prostate cancer cells (LNCaP-FGC-10) cells were investigated by MTT method. While colon cancer cell viability was 10 % at 0.5 ppm, no cytotoxicity was observed on prostate cancer. At 12 ppm, the viability of prostate and cancer cells was reported as 10 % and 30 %, respectively [25]. In addition, the aqueous extracts of this plant obtained by ultrasonic wave assisted extraction and these extract's cytotoxicity was investigated on Hepa 1c1c7 and Ovar 3 cells. Apart from our study, this study is the only study in which ultrasonic wave assisted extraction method was used. Plant samples were purchased commercially and water was used as the extraction solvent. In these samples, only one caused severe cytotoxicity at 250 ppm and 500 ppm concentrations, while notable cytotoxicity was observed in the others [26]. Naz et al. evaluated the cytotoxicity of extracts of leaves and fruits of *Tribulus Terrestris* on brine shrimps. They used methanol as the extraction solvent. Leaf and fruit extracts at 1000 ppm concentrations exhibited mortality of 3.50 % and 5.20 %, respectively. Mortality percentages at 10 ppm were reported as 1.55 % and 2.65 %, respectively [27]. In a study by Menon et al., the effects of methanolic extracts of *Tribulus Terrestris* on DLA and EAC cells in the concentration range of 100-500 ppm were investigated by trypan blue exclusion method. Cell viability rates decreased below 50 % at 380 and 420 ppm [28]. Gacche et al. obtained extracts of *Tribulus Terrestris* fruits with different solvents by Soxhlet extraction. Water extract, ethanol extract and chloroform extract caused cytotoxicity of 50 %, 45 % and 25 %, respectively, at 1000 ppm concentrations on HeLa cells [29]. The cell line we used in our study is MCF-7 breast cancer cell line. Patel et al. first extracted the plant with n-hexane and then re-extracted the defatted extracts with ethanol. It was determined that the seeds of the plant caused 47.02 % cell vi-

ability at 100 ppm concentration and 80.54% cell viability at 12.50 ppm on MCF-7 cell line. It had been reported that the leaves of the plant cause 98.46 % and 69.51 % cell viability on MCF-7 cells at 100 ppm and 12.50 ppm concentrations, respectively [30]. The biological activity of a plant sample varies according to many conditions such as the solvent used in the isolation of its phenolic compounds, extraction technique, climate, coordinates, altitude, soil quality and fertilizer used [31, 32]. The results of previous studies are also very different from each other as they are heavily influenced by these factors.

CONCLUSION

In conclusion, according to the findings of previous studies, it was determined that saponins isolated from methanol and petroleum ether extracts and ethanolic extracts of *T. terrestris* L. cause cytotoxicity. In this study, the effects of the extracts of the aerial parts of the plant obtained by ultrasound assisted extraction using methanol, ethanol and ethyl acetate solvents on the viability of MCF-7 cells were investigated by MTT method. It was determined that only 1000 ppm ethanol extract from the obtained extracts caused moderate cytotoxicity and cell viability was found approximately 80 %. In general, it was determined that *T. terrestris* L. ethanol, ethyl acetate methanol and extracts caused cell proliferation at all other concentrations. Also, breast cancer cells are strong cells compared to normal cells. The fact that the plant extract used in this study did not caused cytotoxicity is attributed to these reasons. Therefore, the use of *Tribulus Terrestris* L. plant collected for this study as an anticarcinogenic agent against breast cancer is not recommended. In addition, it is recommended that more studies be carried out for the use of plants for alternative treatment, especially in patients.

ACKNOWLEDGEMENT

The authors are thanked to Yıldırım Öztürkkan and Kenan Kara for their help in the collection of plant samples, and to Prof. Dr. Fatma Güneş for their support in plant identification, to Prof. Dr. Bingür Sönmez and Prof. Dr. Fikretin Şahin for their support in the supply of cell lines, and to Prof. Dr. Hacı Necetoğlu, Dr. Cem Öziç, Dr. Yunus Ensari and Didem Yıldırım for their technical support.

CONFLICT OF INTEREST

The authors declare that they have no known competing financial interests or personal relationships that could have appeared to influence the work reported in this paper.

AUTHOR CONTRIBUTION

Giray Bugra Akbaba: Performing cytotoxicity experiments and Evaluation of Results; Füreya Elif Ozturkkan: Planning of the study, Performing all experiments Writing-Reviewing and Editing and Evaluation of Results; Mustafa Sertcelik: Performing extraction experiments

References

1. Alp M, Alp A.S. Medisinal Kimyaya Kısa Bir Giriş, 1st ed. Akademisyen Kitabevi, Ankara, 2019.
2. Özbek O, Berkel C, Gürdere MB, Budak Y, Özyigit C, Ceylan M, Yanar Y. The growth inhibitory potential of eudicot-based preparations against plant pathogenic fungi. *Indian Phytopathology* (2021) <https://doi.org/10.1007/s42360-021-00366-8>.
3. Özbek O, Budak Y, Berkel Ç, Özyigit Ç, Yanar Y. The use of *Marrubium vulgare* L. plant extracts in the control of fungal plant pathogens. *International Journal of Agriculture, Environment and Food Sciences* 4(4) (2020) 476–482.
4. Ala AA, Olotu BB, Ohia CMD. Assessment of cytotoxicity of leaf extracts of *Andrographis paniculata* and *Aspilia africana* on murine cells in vitro. *Archives of Basic and Applied Medicine* 6 (2018) 61–65.
5. Evstatieva L, Tchobanov B. Complex Investigations of *Tribulus Terrestris* L. for Sustainable use by Pharmaceutical Industry. *Biotechnology & Biotechnological Equipment* 25 (2011) 2341–2347.
6. Hashim S, Bakht T, Marwat KB, Jan A. Medicinal Properties, Phytochemistry and Pharmacology of *Tribulus Terrestris* L. (*Zygophyllaceae*). *Pakistan Journal of Botany* 46 (2014) 399–404.
7. Angelova S, Gospodinova Z, Krasteva M, Antov G, Lozanov V, Markov T, Bozhanov S, Georgieva EI, Mitev V. Antitumor activity of Bulgarian herb *Tribulus terrestris* L. on human breast cancer cells. *Journal of BioScience and Biotechnology* 2 (2013) 25–32.
8. Kang LP, Wu KL, Yu HS, Pang X, Liu J, Han LF, Zhang J, Zhao Y, Xiong CQ, Song XB, Liu C, Cong YW, Ma BP. Steroidal saponins from *Tribulus terrestris*. *Phytochemistry* 107 (2014) 182–189.
9. Neychev VK, Nikolova E, Zhelev N, Mitev VI. Saponins from *Tribulus terrestris* L. Are Less Toxic for Normal Human Fibroblasts than for Many Cancer Lines: Influence on Apoptosis and Proliferation. *Experimental Biology and Medicine* 232 (2007) 126–33.
10. Sun B, Qu W, Bai Z. [The inhibitory effect of saponins from *Tribulus terrestris* on Bcap-37 breast cancer cell line in vitro]. *Zhong Yao Cai = Zhongyao Cai = Journal of Chinese Medicinal Materials* 26 (2003) 104–106.
11. Bedir E, Khan IA. New Steroidal Glycosides from the Fruits of *Tribulus terrestris*. *Journal of Natural Products* 63 (2000) 1699–1701.
12. Sun B, Qu W, Zhang X, Yang H, Zhuang X, Zhang P. [Investigation on inhibitory and apoptosis-inducing effects of saponins from *Tribulus terrestris* on hepatoma cell line BEL-7402]. *Zhongguo Zhong Yao Za Zhi = Zhongguo Zhongyao Zazhi = China Journal of Chinese Materia Medica* 29 (2004) 681–684.
13. van Meerloo J, Kaspers GJL, Cloos J. Cell sensitivity assays: the MTT assay. *Methods in Molecular Biology* (Clifton, N.J.) 731 (2011) 237–245.

14. Al Jitan S, Alkhoori SA, Yousef L F. Phenolic Acids from Plants: Extraction and Application to Human Health. *Studies in Natural Products Chemistry* 58 (2018) 389–417.
15. Ötleş S, ed. *Handbook of Food Analysis Instruments*. CRC Press, Boca Raton, 2009.
16. Semerdjieva IB, Zheljzkov VD. Chemical Constituents, Biological Properties, and Uses of *Tribulus terrestris*: A Review. *Natural Product Communications* 14(8) (2019) 1-26.
17. Dinchev D, Janda B, Evstatieva L, Oleszek W, Aslani MR, Kostova I. Distribution of steroidal saponins in *Tribulus terrestris* from different geographical regions. *Phytochemistry* 69(1) (2008) 176–186.
18. Li T, Zhang Z, Zhang L, Huang X, Lin J, Chen G. An improved facile method for extraction and determination of steroidal saponins in *Tribulus terrestris* by focused microwave-assisted extraction coupled with GC–MS. *Journal of Separation Science* 32(23–24) (2009) 4167–4175.
19. Reshma PL, Lekshmi VS, Sankar V, Raghu KG. *Tribulus terrestris* (Linn.) Attenuates Cellular Alterations Induced by Ischemia in H9c2 Cells Via Antioxidant Potential. *Phytotherapy Research* 29(6) (2015) 933–943.
20. Abirami P, Rajendran A. GC-MS Analysis of *Tribulus terrestris*. I. *Asian Journal of Plant Science & Research* 1 (2011) 13–16.
21. Ammar NM, El-Din El-Hawary SS, Mohamed DA, Afifi MS, Ghanem DM, Awad G, Research Article Phytochemical and Biological Studies of *Tribulus terrestris* L. Growing in Egypt. *International Journal of Pharmacology* 14 (2) (2018) 248-259.
22. Wang J, Zu X, Jiang Y. Five furostanol saponins from fruits of *Tribulus terrestris* and their cytotoxic activities. *Natural Product Research* 23 (2009) 1436–1444.
23. Abudayyak M, Jannuzzi AT, Özhan G, Alpertunga B. Investigation on the toxic potential of *Tribulus terrestris* in vitro. *Pharmaceutical Biology* 53 (2015) 469–476.
24. Chauhan S, Sharma D, Goel HC. An in vitro evaluation of *Tribulus terrestris* L. fruit extract for exploring therapeutic potential against certain gut ailments. *Indian Journal of Experimental Biology* 56 (2018) 430–436.
25. Pourali M, Yaghoobi MM, Salehi Sormaghi MH. Cytotoxic, Anti-Proliferative and Apoptotic Effects of *Tribulus terrestris* L. Fruit Extract on Human Prostate Cancer Lncap and Colon Cancer HT-29 Cell Lines. *Jundishapur Journal of Natural Pharmaceutical Products* 12 (2016) e33561.
26. Oliveira Filho CC, Kampke EH, Vargas TS, Salustriano NA, Scherer R, Fronza M, Campagnaro BP. In vitro cytotoxic activity of five commercial samples of *Tribulus terrestris* Linn in Espírito Santo (Brazil). *Brazilian Journal of Pharmaceutical Sciences* 53(4) (2018) e00262.
27. Naz R, Ayub H, Nawaz S, Islam ZU, Yasmin T, Bano A, Wakeel A, Zia S, Roberts TH. Antimicrobial activity, toxicity and anti-inflammatory potential of methanolic extracts of four ethnomedicinal plant species from Punjab, Pakistan. *BMC Complementary and Alternative Medicine* 17(1) (2017) 302.
28. Menon D, Dharmapal S, Raghavamenon A, Babu T. Cytotoxic and antitumor effects of *Tribulus terrestris* L fruit methanolic extract. *Journal of Pharmacognosy and Phytochemistry* 3(2) (2014) 1–4.
29. Gacche RN, Dhole NA. Profile of aldose reductase inhibition, anti-cataract and free radical scavenging activity of selected medicinal plants: An attempt to standardize the botanicals for amelioration of diabetes complications. *Food and Chemical Toxicology* 49(8) (2011) 1806–1813.
30. Patel A, Soni A, Siddiqi NJ, Sharma P. An insight into the anticancer mechanism of *Tribulus terrestris* extracts on human breast cancer cells. *3 Biotech* 9(2) (2019) 58.
31. Fieldsend AF, Morison JIL. Climatic conditions during seed growth significantly influence oil content and quality in winter and spring evening primrose crops (*Oenothera* spp.). *Industrial Crops and Products* 12 (2000) 137–147.
32. Endes Z, Er F, Özcan MM, Juhaimi FA. Oil Content, Saturated and Unsaturated Fatty Acids of Some Linseed (*Linum usitatissimum* L.) Genotypes. *Asian Journal of Chemistry* 25 (2013) 9285–9287.
33. International Organization for Standardization. *Biological evaluation of medical devices – ISO 10993, Part 5: Tests for in vitro cytotoxicity*. Geneva, Switzerland; 1999.

Bioadsorbent (Rice Grains) Efficiency in Mercury II Removal from Aqueous Solutions: Adsorption Kinetics, Isotherm and Thermodynamics

Cigdem Oter 

Van Yuzuncu Yil University, Department of Chemistry, Van, Turkey

ABSTRACT

Heavy metals are major pollutants in marine, soil, industrial, and even treated wastewater. These metals are transported by flowing waters and polluted water sources downstream of the industrial site. Mercury is a highly toxically heavy metal. Mercury, on the other hand, is a highly toxically heavy metal. Mercury spillage is hazardous for it destroys the tissue, lungs, brain, and can affect the nervous systems and kidneys, causing some diseases. Therefore, removing Hg (II) from drinking water, aqueous solutions is essential in wastewater treatment and hydrometallurgical. A diverse process has been suggested to eliminate Hg (II) ions from wastewater. The adsorption method is used as a low-cost, efficient, and effective technique for removing toxically heavy metals from wastewater. Researchers have turned to inexpensive adsorbents such as vegetable wastes. This study aimed to remove Hg (II) ions from wastewater by using ground rice grains as adsorbents. The suitability of different isotherm and kinetic models for the adsorption process was researched. It was determined that the Langmuir isotherm best describes the adsorption equilibrium process, and the pseudo-second-order kinetic model is the most suitable model for adsorption. As a result of the analysis of thermodynamic parameters, it was concluded that the adsorption mechanism proceeds spontaneously and has an endothermic character. The data obtained show that rice grains can be considered a cheap, practical, and effective adsorbent for Hg (II) adsorption from wastewater.

Keywords:

Adsorption; Contamination; Isotherm; Kinetics; Mercury II; Thermodynamics

Article History:

Received: 2021/08/23

Accepted: 2021/10/25

Online: 2021/12/31

Correspondence to: Cigdem Oter,
Van Yuzuncu Yil University, Department
of Chemistry, 65040, Van, Turkey.
E-Mail: cigdemoter@yyu.edu.tr
Phone: +90 (506) 825 25
Fax: +0 (432) 225 18 02

INTRODUCTION

The rapid increase in the world population, the excessive increase in industrialization, but the lack of environmental awareness in parallel with this rapidly consumes usable water resources. In addition to the advantages arising from the rapid rise in automation, it poses significant threats to the environment and living things due to the wastes produced. Harmful wastes produced by various industrial establishments can be divided into two categories as organic and inorganic wastes. Of these, organic wastes may be more unstable in the environment than inorganic wastes. However, inorganic wastes can remain undegraded for a long time, especially in aqueous environments, and can cause accumulations. When it comes to inorganic wastes, heavy metals usually come to mind [1]. Various definitions can be made for heavy metals. These metals are called "heavy metals" because their density is more than five g.cm³ in terms of their physical properties. More than 60 heavy metals can be identified in this way, including iron, cop-

per, lead, zinc, nickel, cobalt, mercury, and chromium [2]. Heavy metals are among the pollutants that need to be removed due to their toxic and carcinogenic effects on human and aquatic environments through many sources. These dangerous pollutants are formed because of industrial, agricultural, waste disposal, and military activities. Industrial wastewater is the leading source of heavy metal pollution [3]. Some heavy metal salts are easily mixed in aqueous environments due to their excellent solubility in water. Since most of them dissolve in water as colorless, it is impossible to detect water contaminated with heavy metals easily. Heavy metal ions mixed with aqueous environments from various industrial establishments form precipitates as slightly soluble salts, especially in the sediments of seas, rivers, and lakes. Thus, when the heavy metal dissolved in the water decreases, the deposits release heavy metal ions into the water. This state shows how dangerous heavy metal pollution can be. In this way, living creatures living in waters pol-

luted with heavy metal ions take heavy metals into their bodies. Thus, heavy metals in aquatic environments pass from the most minor living thing to the body of other living things with an increasing concentration through the food chain and threaten [4].

Some conventional techniques of dealing with aqueous contamination include adsorption, coagulation, precipitation, membrane separation, reduction, photocatalysis, ion exchange, and so forth [5, 6]. Amongst these techniques, the adsorption process is easy, low-cost to and an effective way to handle water pollution [7]. Therefore, the quality and quantity necessities of adsorbents are rising. Recently, there are many kinds of commercially present adsorbents for different practices. The improvement of environmentally more efficient, cheap, and friendly adsorbents is a very active investigative issue. Therefore, alternative low-cost adsorbents such as chitin [8], coffee [9], tea waste [10], rice husk [11], orange peel [12], bark [13], and coir pith [14] have been studied.

A widely sourced and low-cost adsorbent with high adsorption capacity should be used to remove mercury ions, a toxic heavy metal, from wastewater. Grown rice is the second most grown cereal plant globally and significant fundamental food for more than half of the world's population [15]. Rice contains some unique ingredients that have proven benefits for human health. Rice grains contain phenolic compounds with antioxidant activity. The most widespread shapes of phenolic compounds in rice are hydroxybenzoic and hydroxycinnamic acids. Other compounds defined contain protocatechuic acid, sinapic, and p-hydroxybenzoic acid, which are benzoic acids. Additionally, the two primary groups of compounds influential, aldehyde analogs such as vanillin are also called phenolics. [16].

This research aims to specify the optimum parameters for the maximum adsorption of Hg (II) ions from aqueous solutions using rice grains, which are widely used and contain different compounds in their structure as adsorbents. In addition, using the obtained data, adsorption kinetics, isotherm models, and thermodynamic properties were evaluated.

MATERIAL AND METHODS

Chemicals and instruments

The rice grains used were purchased from local markets. The $HgCl_2$ salt, 1,5-diphenylcarbazine, Acetic acid (CH_3COOH), and Sodium hydroxide (NaOH) were obtained from Merck and were of analytical grade. A stock solution of mercury chloride salt was prepared (500 mg/L) and diluted to desired concentrations.

WiseStir multiple mechanical stirrer heater, NUVE FN 400 oven, Thermo Scientific ultrapure water device, 620 Lab pH Meter, Optizen POP UV spectrophotometer were used in the experiments.

Adsorption Experiments

Rice obtained from local markets was ground into particles of approximately 100-150 mesh and dried in an oven at 50°C for 12 hours to remove moisture. Dried rice grains were stored in a desiccator for use in experiments without any further modification. Mercury ions adsorption studies were carried out with bioadsorbent (rice grains) in Hg (II) solution (10 mL). The pH of the Hg (II) solution is adjusted between 3 and 10 using diluted 0.1 M CH_3COOH or 0.1 M NaOH solutions. A known mass of bioadsorbent was then added to the mercury solution and shaken at 500 rpm and room temperature. After the adsorption process, the bioadsorbent was removed from mercury solutions by filtration. The concentration of Hg (II) in the solutions was determined at 532 nm with a UV spectrophotometer using 1,5-diphenylcarbazine [17]. The effects of process variables like contact time, temperature, pH, and initial concentration on the mercury removal efficiency were investigated.

Equations for determining the amount of Hg (II) adsorbed using bioadsorbent are given below:

$$q_t = \frac{(C_0 - C_t)}{m} x V \quad (1)$$

$$q_e = \frac{(C_0 - C_e)}{m} x V \quad (2)$$

$$\%R = \frac{(C_0 - C_t)}{C_0} x 100 \quad (3)$$

Where, q_e and q_t are the adsorption capacity (mg/g) at equilibrium and t, respectively; C_0 , C_e and C_t , initial concentration at time t, mercury equilibrium concentration (mg/L) and liquid phase concentration, respectively; the volume (L); m is the amount of adsorbent (g); and R is removed yield (%) [18].

RESULTS AND DISCUSSION

Infrared Spectrum of Bioadsorbent

FT-IR spectra of the bioadsorbent before and after adsorption were recorded between 4000 and 400 cm^{-1} using Bio-Rad-Win-IR spectrophotometer. When the FT-IR graphs before and after Hg (II) adsorption are examined (Fig. 1); stretching vibration of hydroxyl (O-H) and N-H bonds around 3600 cm^{-1} ; at 2970 cm^{-1} the asymmetric stretching of the -CH- groups; asymmetrical carboxy-

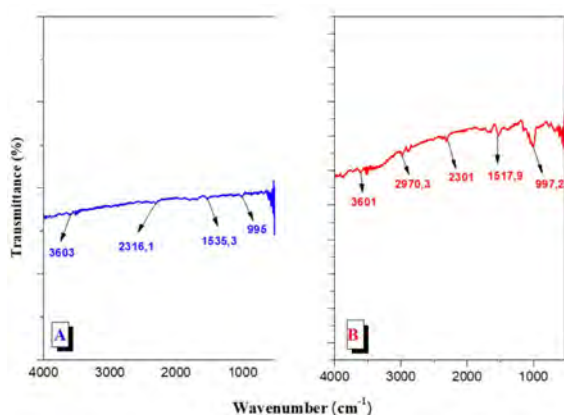


Figure 1. FTIR plots of bioadsorbent (a) after and (b) before Mercury II adsorption

late (-COO-) stretching vibration at 1517 cm^{-1} ; -C-O stretching vibration of alcohol, phenol and carboxylic groups is observed at 997 cm^{-1} . It was observed that the peaks of the functional groups of the bioadsorbent determined before the adsorption process changed because of Hg (II) adsorption. It was observed that some of the previously determined peaks disappeared after Hg (II) adsorption, and there was a shift in frequency values at some peaks. This proves that physical or chemical bonds are formed between the surface functional groups of the bioadsorbent and Hg ions and that adsorption takes place.

pH Effect

The effect of initial pH on Hg (II) removal efficiency was investigated in the pH range of 4-10. Maximum adsorption (84.58%) was obtained at pH=6 (Fig. 2). Depending on the pH range, three main types of HgCl_2 , HgO , and $\text{Hg}(\text{OH})\text{Cl}$ can be found in the solution. Under acidic conditions, HgCl_2 is present, and protons compete with mercury ions to occupy active sites. Thus, the uptake of HgCl_2 , mercury ions is reduced. In the pH (4-6) range, $\text{Hg}(\text{OH})\text{Cl}$ is formed, a species that increases mercury uptake. Under primary conditions, red mercuric oxide precipitates with the most thermodynamically steady kinds obtained at high pH [19]. In a study on the adsorption of mercury on granular activated carbon in aqueous solutions containing nitrates and chlorides, the optimum pH value was found to be 5 [20].

Effect of Adsorbent Amount

In the experiments carried out to examine the effect of the adsorbent dose on the adsorption of mercury ions; Varying amounts of adsorbent in the range of 25-150 mg were used. According to the results obtained, maximum adsorbance was obtained when 100 mg of adsorbent was used and this amount was also used in subsequent studies. The results are shown in Figure 3.

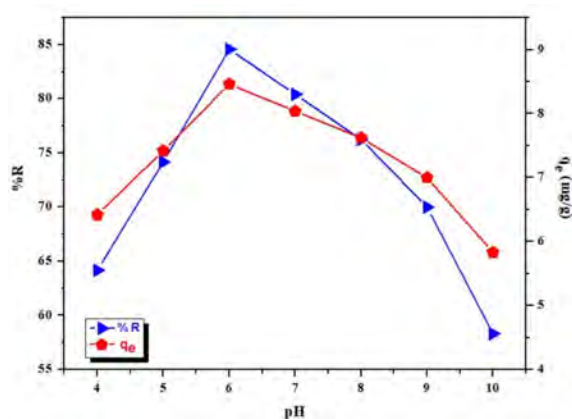


Figure 2. The impact of pH on Mercury II adsorption (25°C, 60 min, 50 mg/L, pH: 4-10).

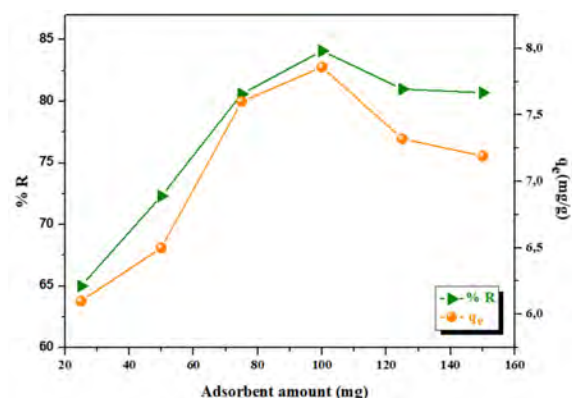


Figure 3. The impact of adsorbent amount on Mercury II adsorption (25°C, pH: 6, adsorbent: 25-150 mg, 50 mg/L).

Effect of Contact Time and Kinetic Studies

One of the parameters effecting adsorption is contact time. As a result of adsorption of 100 mg bioadsorbent and 50 mg/L HgCl_2 solutions at pH 6.0 at 25°C and mixing at 500 rpm for 5-180 minutes, the maximum contact time was found to be 30 minutes (Fig. 4). This time was also used in subsequent parameter studies.

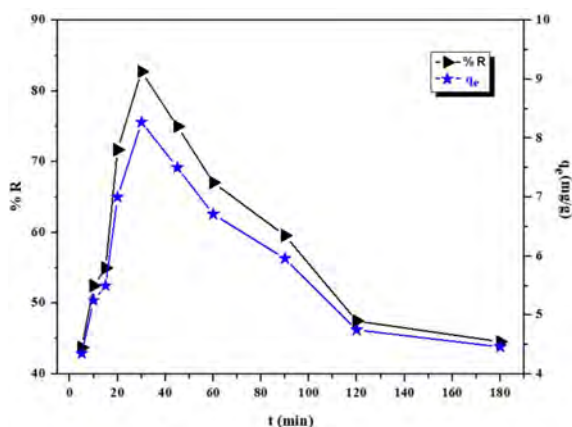


Figure 4. The impact of contact time on Mercury II adsorption (pH: 6, 25°C, 100 mg adsorbent, 50 mg/L).

The kinetics of Hg (II) adsorption were investigated with Pseudo first order (Fig. 5a) [21] and Pseudo second order (Fig. 5b) [22], and intra-particle diffusion (Fig. 5c) [23] models according to the following equations and the calculated parameters are shown in Table 1.

$$\ln(q_e - q_t) = \ln q_e - k_1 t \tag{4}$$

$$\frac{t}{q_t} = \frac{1}{k_2 q_e^2} + \frac{1}{q_e} t \tag{5}$$

$$q_t = K_{id} t^{1/2} + I \tag{6}$$

Where, q_t and q_e are the adsorption capacity (mg/g) at t and equilibrium, respectively. k_1 (1/min) and k_2 (g/mg.dk), the ratio constant of the pseudo-first-order and pseudo-second-order model, K_{id} particle inside diffusion rate regular (mg/g.min^{1/2}). The value of I gives an idea of the thickness of the boundary layer. That is to say, the greater the intersection degree, the greater the boundary layer effect.

Table 1. Kinetic parameters of Mercury II adsorption on bioadsorbent.

Models	Parameters	Hg (II)
Pseudo-first order	q_e (mg/g)	6.36
	k_1 (1/min)	0.07
	R^2	0.8527
Pseudo-second order	q_e (mg/g)	8.19
	k_2 (g/mg.min)	0.02
	R^2	0.9935
Weber-Morris intra-particle diffusion	q_{exp}	8.27
	k (mg/gmin ^{1/2})	1.08
	I (mg/g)	1.8
	R^2	0.8937

When Table 1 is examined, the pseudo-second-order kinetic model appears to be the most appropriate for Hg (II) adsorption. This equality is used to explain the adsorption behaviors at lower concentrations. In the table, it is seen that

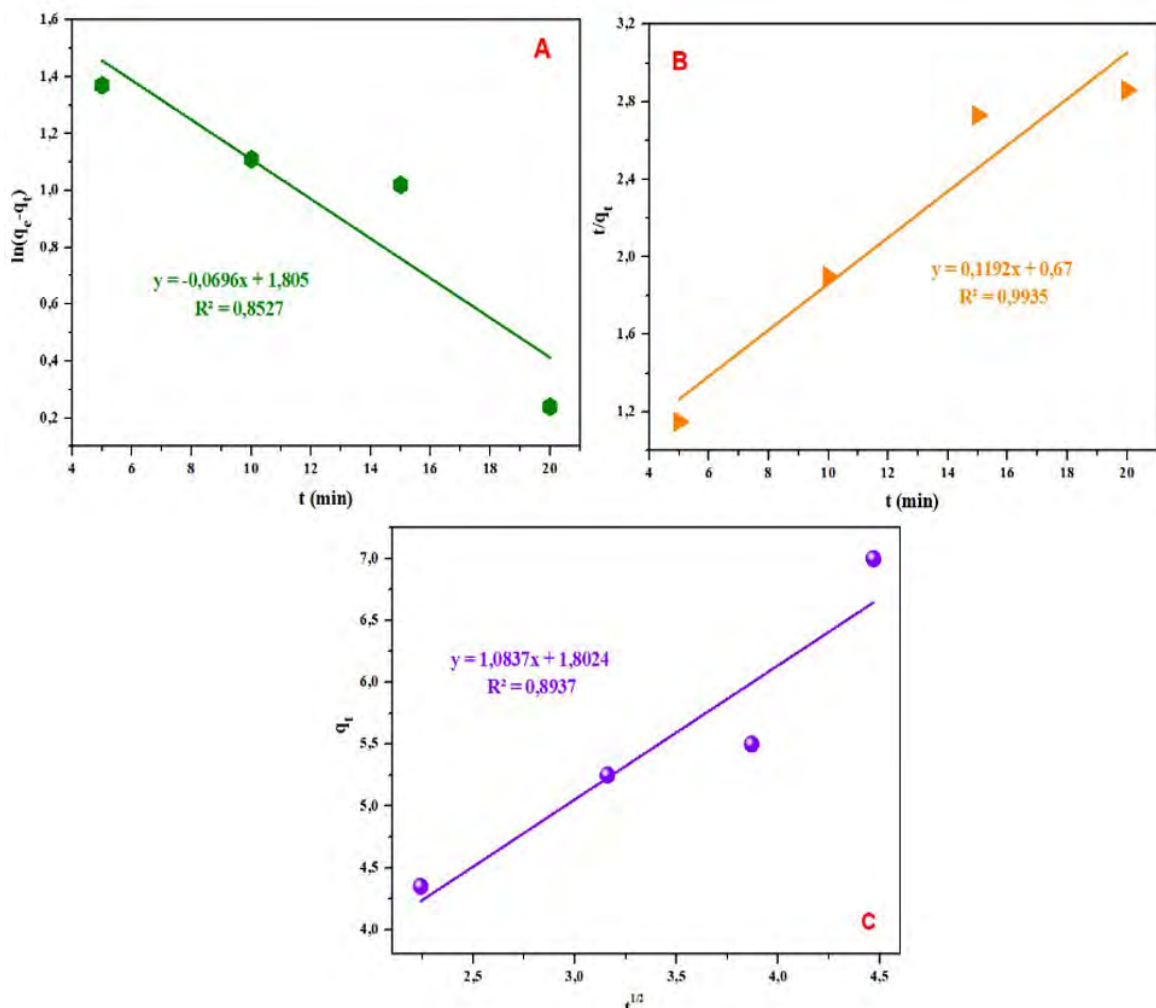


Figure 5. Adsorption kinetics of Mercury II adsorption on bioadsorbent according to (a) pseudo-first-order, (b) pseudo-second-order, (c) intraparticle diffusion kinetic models.

the correlation coefficient R^2 of the pseudo-second-order equation is close to 1 (0.9935), and the q_e value (8.19) calculated from the equation gives a result closer to the q_{exp} (8.27) value. The inadequacy of the pseudo-first-order rate equation to fit the kinetic data is due to the boundary layer that controls the initiation of the adsorption process. In a study in which toxic mercury was removed from petroleum oil using a molecularly imprinted polymer, it was stated that the adsorption process was suitable with the pseudo-second-order kinetic model [24].

Initial Concentration Effect and Adsorption Equilibrium Isotherms

The effect of the initial mercury concentration on the adsorption efficiency was investigated using $HgCl_2$ solutions with concentrations ranging from 10 to 250 mg/L. In the given concentration range at pH 6.0, mercury solutions were shaken with 100 mg bioadsorbent at 500 rpm

for 30 minutes at 25°C. Optimum adsorption efficiency (85.8%) was obtained at 50 mg/L concentration.

Experimental data analyzes were performed in Langmuir, Dubinin-Radushkevich, Temkin, and Freundlich isotherm models to evaluate the adsorption equilibrium process [25, 26, 27, 28]. Isotherm graphs are given in Figure 6, and isotherm parameters are given in Table 2.

The compatibility of Langmuir, Dubinin-Radushkevich (D-R), Temkin, and Freundlich isotherm models to the mercury ion adsorption mechanism was investigated and it was determined that Langmuir isotherm was more compatible. The correlation coefficient calculated for the Langmuir isotherm was $R^2= 0.9964$, which was higher than the other isotherms. Accordingly, in the Langmuir equilibrium isotherm, the adsorption process is adsorption in which mercury ions bind to functional groups and binding sites homogeneously distributed on the adsorbent surface in a monolayer. At the

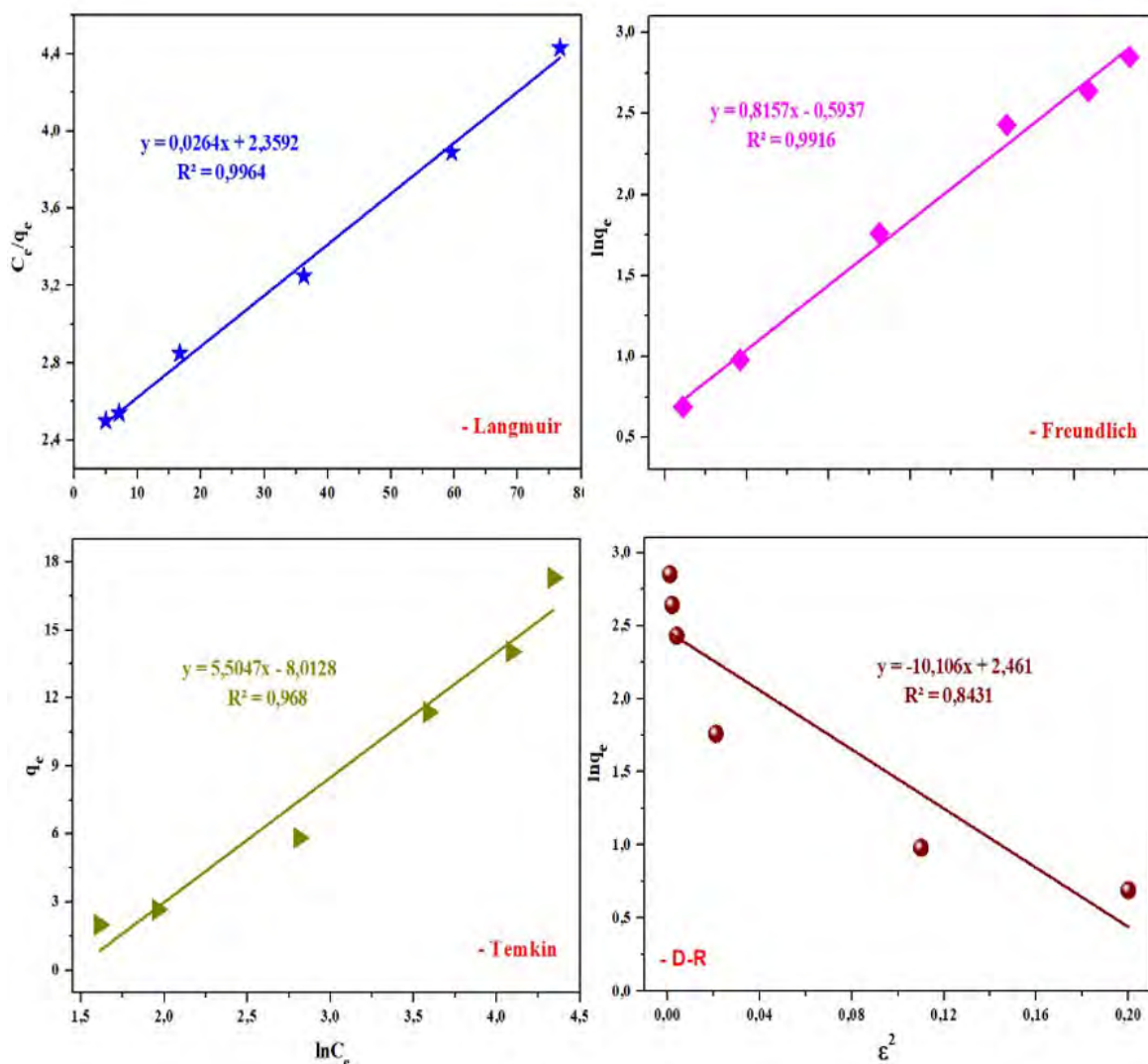


Figure 6. Isotherm graphics for the Mercury II adsorption process.

Table 2. Isotherm parameters for adsorption process.

Models	Parameters	Hg (II)
Langmuir	q_{\max} (mg/g)	37.88
	b (L/mg)	0.01
	R_L	0.2
	R^2	0.9964
Freundlich	K_f	0.55
	$[(\text{mg/g}) (\text{L/mg})^{1/n}]$	
	n	1.23
	R^2	0.9916
Temkin	bT	0.23
	K_T (L/g)	5.5
	R^2	0.968
Dubinin-Radushkevich	q_m (mg/g)	11.72
	β (1/mol ² .J ²)	10.1
	E (J/mol)	0.22
	R^2	0.8431

same time, in this adsorption, there is a certain number of active sites on the adsorbent surface and the molecules bind to these active ends. Accordingly, mercury ions are attached to the functional groups and binding sites on the surface as a single layer. The maximum monolayer adsorption coefficient (q_{\max}) value was found to be 37.88 mg/g. Using the b value from the calculated Langmuir parameters, the R_L values (dimensionless separation factor) were found to be as 0.2. The fact that these values are in the range of $0 < R_L < 1$ indicates that the adsorption mechanism is suitable for mercury ions. In a study in which mercury adsorption was performed by rice husk ash, it was stated that Langmuir isotherm, one of the isotherm models, was more compatible with the adsorption system and the maximum adsorption capacity (q_{\max}) was 9.32 mg/g [29].

Then value defined in the Freundlich isotherm model was calculated as 1.23. The calculated n value in the range of $1 < n < 10$ means that the adsorption of mercury ions on the bioadsorbent is favored and positive.

The mean adsorption energy (E) value defined in the Dubinin-Radushkevich isotherm delivers an opinion concerning the reaction mechanism that is efficient in the adsorption process. Since the calculated E value is calculated to be 0.22 kJ/mol ($E < 8$ kJ/mol), physical forces are efficient in adsorption. Due to physical adsorption, it can be mentioned that there are weak Van der Waals attraction forces between bioadsorbent and mercury ions.

Temperature Effect and Thermodynamic Studies

To examine the impact of ambient temperature on the adsorption of 50 mg/L solutions of mercury ions with 100 mg bioadsorbent; It was studied for 30 minutes at pH 6.0, at a stirring speed of 500 rpm, at temperatures ranging from 20-50°C. The optimum temperature for the adsorption process was found to be 50°C (Fig. 7). The rising in

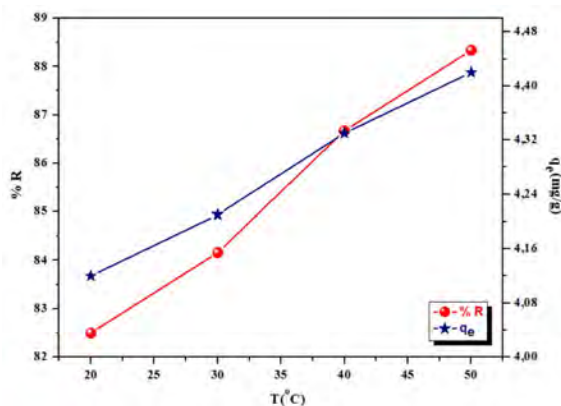


Figure 7. The effect of temperature on Mercury II adsorption (pH: 6, 30 min, 100 mg adsorbent, 50 mg/L).

adsorption yield with temperature indicates that the process is endothermic.

The thermodynamic parameters enthalpy change (ΔH°), free energy (ΔG°), and entropy change (ΔS°) are gotten from the following equations [30].

$$\ln K_d = \frac{\Delta S^\circ}{R} - \frac{\Delta H^\circ}{RT} \quad (7)$$

$$\Delta G^\circ = \Delta H^\circ - T\Delta S^\circ = -RT \ln K_d \quad (8)$$

$$K_d = \frac{C_{ad}}{C_e} \quad (9)$$

Inequality, C_e is the equilibrium concentration of mercury in the solution; K_d is the equilibrium constant; C_{ad} , the concentration of mercury adsorbed to the adsorbents at equilibrium; R (8.314 (J/mol.K) is the gas constant; T (K) is temperature. ΔH° and ΔS° are obtained from the incline and intersection of the Van't Hoff plot of $\ln K_d$ for $1/T$ (Fig. 8), values are obtained from the slope and intersection of the graph, and these results are shown in Table 3.

The enthalpy of adsorption (ΔH°) value calculated from the incline of the line in the graph in Figure 8 was favorable for the adsorption of mercury ions. It showed that the adsorption had an endothermic nature. At the same time, the fact that the adsorption enthalpy values are lower than 40 kJ/

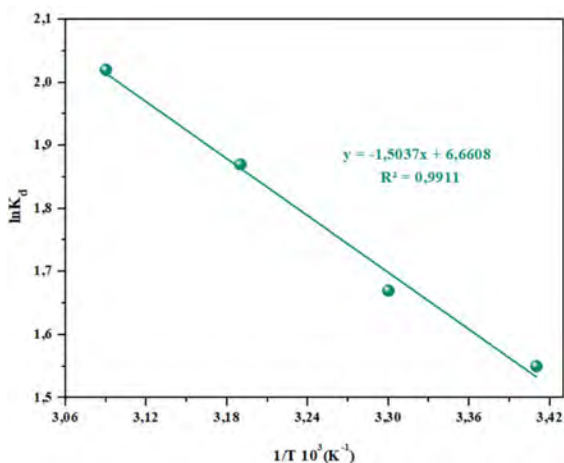


Figure 8. Change of $\ln K_d$ with $1/T$ in Mercury II adsorption.

Table 3. Thermodynamical parameters for Mercury II adsorption.

Thermodynamic parameters				
T (K)	ΔH° (J/mol)	ΔS° (J/mol K)	$T\Delta S^\circ$ (kJ/mol)	ΔG° (kJ/mol)
293			16.4	-3.77
303	12.5	55.38	16.78	-4.21
313			17.33	-4.87
323			17.89	-5.42

mol shows that the adsorption processes can be explained by physical adsorption. The adsorption entropy (ΔS°) value calculated from the shift of the graph in Figure 8 was also found to be positive. This result shows that the adsorption occurs spontaneously and that the bioadsorbent has an affinity for mercury ions. The Gibbs free energy change (ΔG°) was calculated as an average of -4.57 kJ/mol. The increase in the negative values of ΔG° with rising temperature indicates that adsorption at high temperatures is even more convenient and applicable. At the same time, the negative value of Gibbs free energy (ΔG°) shows that adsorption consists spontaneously. In a study in which mercury adsorption was carried out on a carbon sorbent obtained from fruit peel; It was stated that the positive value of ΔH° indicates the endothermic adsorption of Hg ions and the positive value of ΔS° indicates the increasing randomness at the solid-solution interface during Hg (II) adsorption. It was also stated that the negative values of ΔG° and the decrease in ΔG° with temperature increase indicate the spontaneous nature of its adsorption [31].

CONCLUSION

The adsorption method is a very effective method among the various methods used for the removal of heavy metals in wastewater, nowadays, where the prevention of environmental pollution is becoming increasingly important.

In the study, rice grains containing different compounds in their structure were used as adsorbents to remove toxic metal pollutants.

The suitability of adsorption with isotherm models, kinetic models, and thermodynamic expressions was investigated with the data obtained due to the experiments for the adsorption of mercury ions from aqueous solutions on bioadsorbent.

Pseudo-first-order kinetic model, pseudo-second-order kinetic model, and intraparticle diffusion models were evaluated for mercury adsorption processes. The most suitable kinetic model was determined to be the pseudo-second-order kinetic model. Freundlich, Langmuir, Dubinin-Radushkevich, and Temkin's isothermal models were examined for their suitability for adsorption processes. It was stated that the equilibrium data of adsorption isotherms were quite compatible for the Langmuir model in the concentration range studied, and the q_{max} value was calculated as 37.88 mg/g. As a result of the analysis of thermodynamic parameters, it was determined that the adsorption processes were spontaneous and endothermic. Also, entropy with a positive value shows the affinity of mercury ions to the bioadsorbent.

According to the results, it is stated that rice grains used without any chemical treatment to remove mercury from aqueous solutions are low cost and effective adsorbents. It is thought that this bioadsorbent can be used as an alternative to adsorbents prepared with costly and complex processes, and this study will contribute to environmental studies.

CONFLICT OF INTEREST

The authors declare that they have no known competing financial interests or personal relationships that could have appeared to influence the work reported in this paper.

References

- Gültekin S, Sesal C, Kayhan FE. İstanbul ili Anadolu yakası doğal kaynak sularının kimyasal analizlerinin değerlendirilmesi. *Marmara Fen Bilimleri Dergisi* 28(4) (2016) 132-140.
- Kahvecioğlu Ö, Kartal G, Güven A, Timur S. Metallerin çevresel etkileri-I. TMMOB Metalurji Mühendisleri Odası Metalurji Dergisi 136 (2003) 47-53.
- Ali RM, Hamada HA, Hussein MM, Malash GF. Potential of using green adsorbent of heavy metal removal from aqueous solutions: Adsorption kinetics, isotherm, thermodynamic, mechanism and economic analysis, *Ecological Engineering* 91 (2016) 317-332.
- Deniz S, Dartan G, Türkmenoğlu YK. Synthesis of A New Cysteine Containing Adsorbent and Removal of Pb (II) and Hg (II) Ions From Aqueous Media. *Marmara Fen Bilimleri Dergisi* 3 (2018) 195-200.

5. Shu J, Liu R, Qiu J, et al. Simultaneous removal of ammonia nitrogen and manganese from wastewater using nitrite by electrochemical method. *Environmental Technology* 38 (2017) 370-376.
6. Yuan HP, Nie JY, Gu L, et al. Studies on affecting factors and mechanism of treating decentralized domestic sewage by a novel anti-clogging soil infiltration system. *Environmental Technology* 37 (2016) 3071-3077.
7. Hakami O, Zhang Y, Banks CJ. Thiol-functionalised mesoporous silica-coated magnetite nanoparticles for high efficiency removal and recovery of Hg from water. *Water Research* 46 (2012) 3913-3922.
8. Gurusamy A, Jiunn-Fwu L. Equilibrium studies on the adsorption of acid dye into chitin. *Environmental Chemistry Letters* 6 (2008) 77-81.
9. Franca AS, Oliveira LS, Ferreira ME. Kinetics and equilibrium studies of methylene blue adsorption by spent coffee ground. *Desalination*, 249 (2009) 267-272.
10. Tamez UM, Akhtarul IM, Shaheen M, Rukanuzzaman M. Adsorptive removal of methylene blue by tea waste. *Journal Hazardous Material* 164 (2009) 53-60.
11. Ola A, Ahmed E N, Amany ES, Azza K. Use of rice husk for adsorption of direct dyes from aqueous solution: A case study of direct F. Scarlet. *Egyptian Journal Aquatic Research* 31 (2005) 1-11.
12. Mokhtar A, Nargess Y.L, Niyaz MM, Nooshin ST. Removal of dyes from colored textile wastewater by orange peel adsorbent: Equilibrium and kinetic studies. *Journal of Colloid and Interface Science* 288 (2005) 371-376.
13. Tan LS, Jain K, Rozaini CA. Adsorption of textile dye from aqueous solution on pretreated mangrove bark, an agricultural waste: Equilibrium and kinetic studies. *Journal of Applied Sciences and Environmental Management* V(N). (2010) 266-276.
14. Kavitha D, Namasivayam C. Experimental and kinetic studies on methylene blue adsorption by coir pith carbon. *Bioresearch Technology* 98 (2007) 14-21.
15. OECD-FAO. *Agricultural Outlook 2011*, release 6, (2011) <http://dx.doi.org/10.1787/888932427797>
16. Setyaningsih W, Saputro IE, Palma M, Barroso CG. Optimisation and validation of the microwave-assisted extraction of phenolic compounds from rice grains. *Food Chemistry* 169 (2015) 141-149.
17. Samaneh SS, Gazi M. Removal of Mercury (II) from Aqueous Solution using Chitosan-graft-Polyacrylamide Semi-IPN Hydrogels. *Separation Science and Technology* 48 (2013) 1382-1390
18. Öter Ç, Zorer ÖS. Molecularly imprinted polymer synthesis and selective solid phase extraction applications for the detection of ziram, a dithiocarbamate fungicide. *Chemical Engineering Journal Advances* 7 (2021) 100118.
19. Pourjavadi A, Mahdavinia GR. Superabsorbency, pH sensitivity and swelling kinetics of partially hydrolyzed chitosan-g-poly (acrylamide) hydrogels. *Turkish Journal of Chemistry* 30 (2006) 595.
20. Di Natale F, Erto A, Lancia A, Musmarra D. Mercury adsorption on granular activated carbon in aqueous solutions containing nitrates and chlorides. *Journal of Hazardous Materials* 192 (2011) 1842-1850.
21. Lagergren S. About the theory of so-called adsorption of soluble substances, *Kongliga Svenska Vetenskapsakademiens Handlingar* 24 (1898) 1-39.
22. Ho YS, McKay G., Pseudo-second order model for sorption processes, *Process Biochemistry*. 34 (1999) 451-465.
23. Weber WJ, Morris JC. Kinetics of adsorption on carbon from solution. *Journal of the Sanitary Engineering Division* 89 (1963) 31-60.
24. Khairi NAS, Yusof NA, Abdullah AH, Mohammad F. Removal of Toxic Mercury from Petroleum Oil by Newly Synthesized Molecularly-Imprinted Polymer. *International Journal of Molecular Sciences*. 16 (2015) 10562-10577.
25. Langmuir I. The constitution and fundamental properties of solids and liquids. *Journal of the American Chemical Society* 38 (1916) 2221-2295.
26. Dubinin MM, Radushkevich LV. The equation of the characteristic curve of the activated charcoal, *Proceedings of Academy of Sciences. Physical Chemistry Section* 55 (1947) 331-337.
27. Temkin MI, Pyzhev V. Kinetics of ammonia synthesis on promoted iron catalyst, *Acta Physico-Chimica Sinica USSR*. 12 (1940) 327-356.
28. Freundlich HMF. Over the adsorption in solution. *Journal of Physical Chemistry* 57 (1906) 385-471.
29. Feng Q, Lin Q, Gong F, Sugita S, Shoya M. Adsorption of lead and mercury by rice husk ash. *Journal of Colloid and Interface Science* 278 (2004) 1-8.
30. Alver E, Metin AÜ, Brouers F. Methylene blue adsorption on magnetic alginate/rice husk bio-composite. *International Journal of Biological Macromolecules* 154 (2020) 104-113.
31. Stephen Inbaraj B, Sulochana N. Mercury adsorption on a carbon sorbent derived from fruit shell of *Terminalia catappa*. *Journal of Hazardous Materials B133* (2006) 283-290.

Computational Analysis of Potential Key Genes Associated with Dopamine Neurotransmission in Pheochromocytoma and Paraganglioma

Orcun Avsar 

Hitit University, Department of Molecular Biology and Genetics, Corum, Turkey

ABSTRACT

Pheochromocytoma and Paraganglioma (PCPG) are rare and potentially lethal neuroendocrine tumors. PCPG that predominantly or exclusively produce and secrete DA is rarely seen, and it has been known that exclusively dopamine-secreting PCPG is related to advanced malignant features and metastases. Up to the present, little has been known about the role of dopamine neurotransmission and the dopaminergic system in the initiation and progression of PCPG. The genes with significant expression differences between normal tissue and pheochromocytoma and paraganglioma, survival and correlation analysis, CpG islands prediction, and miRNA-target enrichment analysis were performed by several bioinformatics tools. In the present study, it was determined that the COMT gene was significantly less expressed in PCPG than in normal tissue and the COMT gene showed a remarkable relationship between differential expression with shorter overall survival among the individuals with PCPG (HR=1, $p=0.011$). MAOA and COMT gene pair was significantly correlated with PCPG ($p=0.012$; $R=0.19$), and hsa-miR-5000-5p regulates the expression of both COMT and MAOA genes ($p=0.00215$, $FDR=0.127$). Our findings suppose that COMT may potentially be implicated in tumor suppressive mechanism. The expression values of COMT and MAOA genes, and hsa-miR-5000-5p may have the potential to be used in the genetic evaluation of the pathogenesis and prognosis of PCPG. Further *in vitro* and *in vivo* studies are required to clarify the molecular mechanism of the dopaminergic system in the pathogenesis and prognosis of PCPG.

Keywords:

Dopamine; Pheochromocytoma and Paraganglioma (PCPG); Dopaminergic system; Gene expression; Neurotransmission

INTRODUCTION

Pheochromocytoma and Paraganglioma (PCPG) are rare chromaffin cell tumors that produce catecholamines (CA) and present a therapeutic and diagnostic challenge, and are associated with severe morbidity when non-diagnostic [1, 2]. Pheochromocytomas and Paragangliomas are originated from adrenal tissues or extra-adrenal parasympathetic or sympathetic paraganglia, respectively [2]. PCPG produce and secrete CA in the neuroendocrine system. PCPG may lead to the elevation of blood pressure and subsequently damage of target organs such as the brain, heart, and kidney. The symptoms of PCPG include palpitations, hypertension, headache, anxiety, and profuse sweating. Furthermore, PCPG may lead to metabolic disorders that are associated with insulin and blood sugar, therefore endanger the life of patients [3, 4].

Circulating catecholamines are composed of nore-

pinephrine (NE), epinephrine (EPI), and dopamine (DA) that are mainly synthesized and released from the adrenal medulla (chromaffin cells) [5]. Specifically, DA acts as a neurotransmitter and neurohormone that modulates cognition, motivation, food intake, appetite, sexual behavior, emotion, reward system, motor activity, and prolactin secretion in the central nervous system [6, 7]. Moreover, DA participates in the regulation of inhibition of aldosterone secretion, vasodilation, inhibition of insulin secretion, diuresis, phagocytic inhibition, IgM and IgG secretion, and natriuresis in the periphery [6].

Increased generation of catecholamines is the distinctive biochemical feature of PCPG. Until recently, the biochemical prediction of PCPG was based primarily on detecting NE, EPI, or their metabolites (no interest in DA or its metabolites). PCPG that exclusively produce and secrete DA are rarely seen, and it has been known that exclusively dopamine-secreting PCPG are related

Article History:

Received: 2021/09/07

Accepted: 2021/11/17

Online: 2021/12/31

Correspondence to: Orcun Avsar,
Hitit University, Department of Molecular
Biology and Genetics, 19030, Corum,
Turkey.

E-Mail: orcunavsar.gen@gmail.com

Phone: +90 (364) 227 1658

Fax:

to advanced malignant features. Lack of clinical symptoms and the rarity of the tumor make it difficult to be detected and may cause to delay of diagnosis and poorer prognosis [8, 9]. Delayed diagnosis might be associated with the increased incidence of malignancy and metastasis. Up to the present, little has been known about the role of dopamine neurotransmission and the dopaminergic system in the initiation and progression of PCPG. Furthermore, differential diagnosis might be achieved by analyzing the expression levels of dopamine neurotransmission-related genes. Therefore, the particular relationship between dopamine neurotransmission and PCPG behavior needs further elucidating. In the present study, we aimed to determine the relationship between the genes associated with dopamine neurotransmission and PCPG by computational methods.

MATERIALS AND METHODS

Expression and Survival Analysis of Target Genes in PCPG and Normal Tissue

The sequence information and the functions of the target genes that are associated with dopamine neurotransmission were analyzed and extracted from National Center for Biotechnology Information (NCBI) database [10]. The genes with remarkable expression differences between normal tissue and pheochromocytoma and paraganglioma were designated via Gene Expression Profiling Interactive Analysis (GEPIA) database. GEPIA is an online tool and based on The Genotype-Tissue Expression (GTEx) and The Cancer Genome Atlas (TCGA) that delivers cancer and normal tissue gene expression and interactive analysis data. Furthermore, the 95% confidence interval (95% CI) and the Cox proportional hazard ratio (HR) of the survival plot are provided by the database [11]. Analysis of differential gene expression ensures to find the tumor-specific genes by comparing normal and tumor groups.

Correlation Analysis of Some Target Genes in PCPG

The statistical analysis of the relationship between MAOA and COMT genes and PCPG; TH and DDC genes and PCPG were verified by the use of the Spearman correlation test.

Estimation of Protein-Protein Interactions

The Search Tool for the Retrieval of Interacting Genes/Proteins (STRING) web tool was used to predict the functional partners of the proteins that are encoded by the target genes. The significant integration and assessment of protein-protein interactions with functional (in-

direct) and physical (direct) associations are provided by the STRING database [12].

Prediction of CpG Islands of Target Genes

In this study, the CpG islands in some target genes were analyzed by the MethPrimer bioinformatics tool to predict the effect of methylation on the expression of target genes. The values of “observed/expected CpG ratio” = 0.60, “island size” > 100 nucleotide, and “percentage of G plus C” = 50.0 were set in the MethPrimer program as standard values. MethPrimer is a program that finds the potential CpG islands based on DNA sequence and designs the primers for bisulfite sequencing PCR and methylation specific PCR [13].

miRNA-Target Enrichment Analysis

microRNAs are implicated in the regulation of gene expression. Multiple genes can be regulated by one miRNA and one gene can be targeted by several miRNAs in a simultaneous way. MicroRNA ENrichment TURned NETwork (MIENTURNET) program was used for the miRNA-target enrichment analysis. miRNA-target enrichment analysis is a standard method to clarify the hierarchical effects of microRNAs in the regulatory networks of genes [14, 15].

RESULTS AND DISCUSSION

Expression and Survival Analysis of Dopamine Neurotransmission-Related Genes in PCPG and Normal Tissue by *in silico* Methods

The expression values of TH, DDC, DBH, PNMT, MAOA, MAOB, COMT, ALDH2, DRD1, DRD2, DRD3, DRD4, DRD5, SLC6A3, SLC18A1 and SLC18A2 genes were analyzed and expression differences between PCPG and normal tissue were compared. The genes with remarkable expression differences between PCPG and normal tissue were identified. According to the analysis, MAOA, MAOB, COMT, ALDH2, and DRD1 genes were significantly less expressed in PCPG than in normal tissue. On the other hand, expression of TH, DDC, DBH, PNMT, DRD2, SLC18A1, and SLC18A2 genes were significantly higher in PCPG compared to normal tissue (Table 1). The median, log₂, and percentage values of the over-expressed genes in PCPG were shown in Table 2. The comparison of the expression values of the genes in PCPG and normal tissue was illustrated in Figure 1, Figure 2, and Figure 3. The relationship between gene expressions with overall survival of PCPG patients were evaluated to determine the role of the genes associated with the dopaminergic system in PCPG prognosis by dividing the

population into low expression and high expression, only one gene showed a remarkable relationship between differential expression with shorter overall survival among the individuals with PCPG. Log rank ($p < 0.05$) is accepted as statistically significant. The gene-COMT ($HR=1$, $p=0.011$) may serve as a molecular biomarker for PCPG (Figure 4).

Correlation Analysis of MAOA and COMT Genes and TH and DDC Genes in PCPG

The statistical analysis of the relationship between MAOA and COMT genes (encode the enzymes that degrade dopamine) and PCPG was performed via the GEPIA database. It was determined that MAOA and COMT gene pair was significantly correlated with PCPG by the Spearman correlation analysis ($p=0.012$; $R=0.19$) (Figure 5). Furthermore, Spearman correlation analysis has determined that the TH and DDC gene (encode the enzymes that are involved in the synthesis of dopamine) pair was significantly associated with PCPG ($p=0.043$; $R=0.15$) (Figure 6).

Prediction of Protein-Protein Interactions

Protein-protein interactions were estimated by STRING web tool to elucidate the functional partners of the enzymes degrading DA (MAOA and COMT) and the enzymes catalyzing the synthesis of DA (TH and DDC). Based on the findings of STRING for MAOA protein, functional interactants with high confidence were determined as: COMT (0.989), DDC (0.971), DBH (0.962), ALDH2 (0.961), CYP2D6 (0.955), AOC2 (0.951), ALDH3B2 (0.945), HNMT (0.943), ADH1B (0.942), PNMT (0.940) (Figure 7). Functional interactants of COMT protein were predicted as follows: MAOA (0.989), MAOB (0.987), DDC (0.980), DBH (0.971), CYP1B1 (0.971), CYP1A1 (0.968), PNMT (0.963), ALDH2 (0.944), ALDH1B (0.944), DRD2 (0.940) (Figure 8). Functional partners of TH protein were determined as follows: SNCA (0.992), DDC (0.992), SPR (0.968), PCBD1 (0.953), QDPR (0.951), DBH (0.945), TYR (0.943), SLC18A2 (0.937), AKR1B1 (0.927), GOT1 (0.926) (Figure 9). The functional interactants of DDC protein with high confidence were determined as: TH (0.992), DBH (0.987), TPH1 (0.984), COMT (0.980), MAOB (0.975), MAOA (0.971), TPH2 (0.969), PAH (0.966), AOC1 (0.964), AANAT (0.962) (Figure 10). According to the predictions of STRING web tool, it was demonstrated that MAOA and TH interact with COMT protein, and DDC, respectively.

Analysis of CpG Islands

Methylation is involved in the regulation of gene expression [16]. In the present study, CpG islands were analyzed

to determine the potential role of methylation in the regulation of TH, DDC, MAOA, and COMT genes. According to the findings of the study, the number of CpG islands (CIG) were indicated as follows: TH-4 CIG; DDC-1 CIG; MAOA-0 CIG; COMT-4 CIG, and the results are seen in Table 3.

miRNA-Target Enrichment Analysis

The miRNAs which have the potential to regulate the expression of more than one gene associated with dopaminergic system among the investigated mRNAs were shown in Table 4. Common miRNAs for SLC18A2 and DRD2: hsa-miR-141-3p and hsa-miR-200a-3p; for SLC18A2 and DRD1: hsa-miR-142-5p and hsa-miR-5590-3p; for DRD2 and SLC18A2: hsa-miR-9-5p; for COMT, SLC6A3, and DRD1: hsa-miR-30a-5p, hsa-miR-30b-5p, hsa-miR-30c-5p, hsa-miR-30d-5p, and hsa-miR-30e-5p; for COMT and MAOA: hsa-miR-5000-5p; for ALDH2 and TH: hsa-miR-1-3p; for ALDH2, DBH, DRD5, and MAOB: hsa-miR-335-5p; for ALDH2 and COMT: hsa-

Table 1. Expression values of the genes associated with dopamine neurotransmission in PCPG and normal tissue

Gene ID	Pheochromocytoma and Paraganglioma (PCPG)	Normal tissue
TH*	1,830.03	24.87
DDC*	599.55	3.34
DBH*	2,853.17	20.21
PNMT*	113	8.91
MAOA*	6.97	22.01
MAOB*	8.26	39.2
COMT*	112.21	256.67
ALDH2*	69	346.45
DRD1*	0.05	0.24
DRD2*	86.66	0.98
DRD3	-	-
DRD4	0.32	0.19
DRD5	0.02	0.01
SLC6A3	0.02	0.01
SLC18A1*	145.98	0.37
SLC18A2*	133.17	1.03

*significant differential expression pattern between PCPG and normal tissue

miR-16-5p; for PNMT and DRD3: hsa-miR-26b-5p.

Pheochromocytoma and Paraganglioma (PCPG) are rare and potentially lethal neuroendocrine tumors. Despite most of the tumors are benign, approximately 10-15% are classified as malignant and develop metastases in nonchromaffin tissues such as bone, liver, and lymph nodes [17]. It is

Table 2. The median, log2, and percentage values of the over-expressed genes in PCPG

Gene ID	Median (Tumor)	Median (Normal)	Log2 (Fold change)	Percentage
TH	4539.601	616.945	2.877	1.00e+0
DDC	1548.065	385.690	2.002	1.00e+0
DBH	6086.722	303.910	4.319	1.00e+0
PNMT	2178.772	465.310	2.225	9.44e-1
SLC18A1	759.997	20.487	5.146	1.00e+0
SLC18A2	534.371	89.529	2.564	1.00e+0

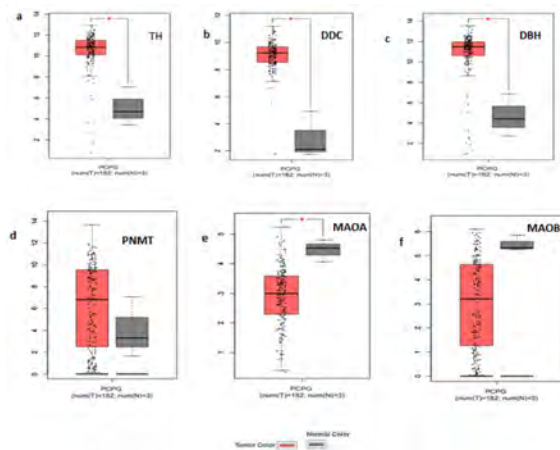


Figure 1. Differential expressions of TH, DDC, DBH, PNMT, MAOA, and MAOB genes in PCPG

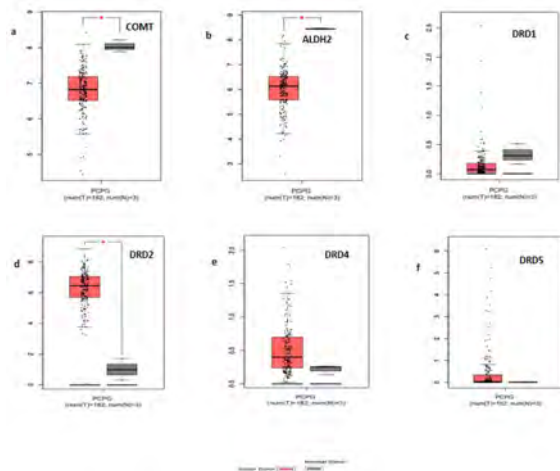


Figure 2. Differential expressions of COMT, ALDH2, DRD1, DRD2, DRD4, and DRD5 genes in PCPG

significant to diagnose PCPG in an accurate and early way to treat patients and also affected members in family cases [18]. PCPG usually secrete high amounts of catecholamines. Tumors that predominantly or exclusively produce DA are rare and often malignant and metastatic [17, 19].

Dopamine, biogenic monoamine, is a member of catecholamine neurotransmitters and generated in both central nervous system and periphery. The dopaminergic system is implicated in several biological functions such

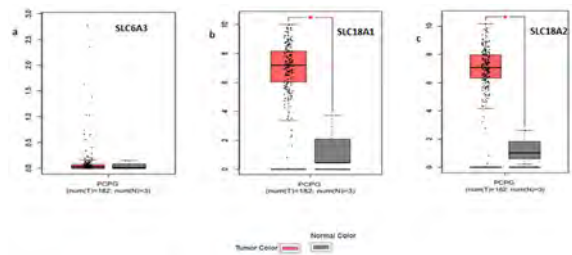


Figure 3. Differential expressions of SLC6A3, SLC18A1, and SLC18A2 genes in PCPG

as motivation, cognition, motor activity, maternal behavior, reward system, and reproductive behavior. Dopamine is synthesized directly from tyrosine or indirectly from L-phenylalanine. Tyrosine hydroxylase is the rate limiting enzyme in DA synthesis that converts tyrosine to L-DOPA and L-DOPA may be converted into DA by DOPA decarboxylase. Subsequently, DA is sequestered into the synaptic vesicles through vesicular monoamine transporter 2 (VMAT2) in dopaminergic neurons, preventing oxidation. DA may be further converted into NE or EPI by modifications from DBH and PNMT in adrenergic and noradrenergic cells [20]. In a non-acidic microenvironment, DA is metabolized by MAO and COMT enzymes [21]. Dopamine exerts its functions via binding to G protein-coupled receptors (DRD1, DRD2, DRD3, DRD4, DRD5) [22].

The dopaminergic phenotype of PCPG is composed of a rare subtype of PCPG that predominantly or exclusively secrete DA (no significant NE and EPI levels) [23]. In contrast to the symptoms that are seen in epinephrine and norepinephrine-secreting tumor in high amounts, the tumors that predominantly or exclusively produce DA are normotensive and asymptomatic [23]. DA secreting PCPG are generally larger tumors than epinephrine and norepinephrine-secreting tumors due to delayed diagnosis (incidentally identified). There are several significant differences, such as the risk of recurrence, malignancy, and peri-operative cardiovascular collapse between DA secreting PCPG and NE and EPI secreting PCPG in terms of management [24]. Moreover, DA secreting PCPG have high malignancy risk compared to NE and EPI secreting PCPG [25].

In the current study, we have analyzed the genes as-

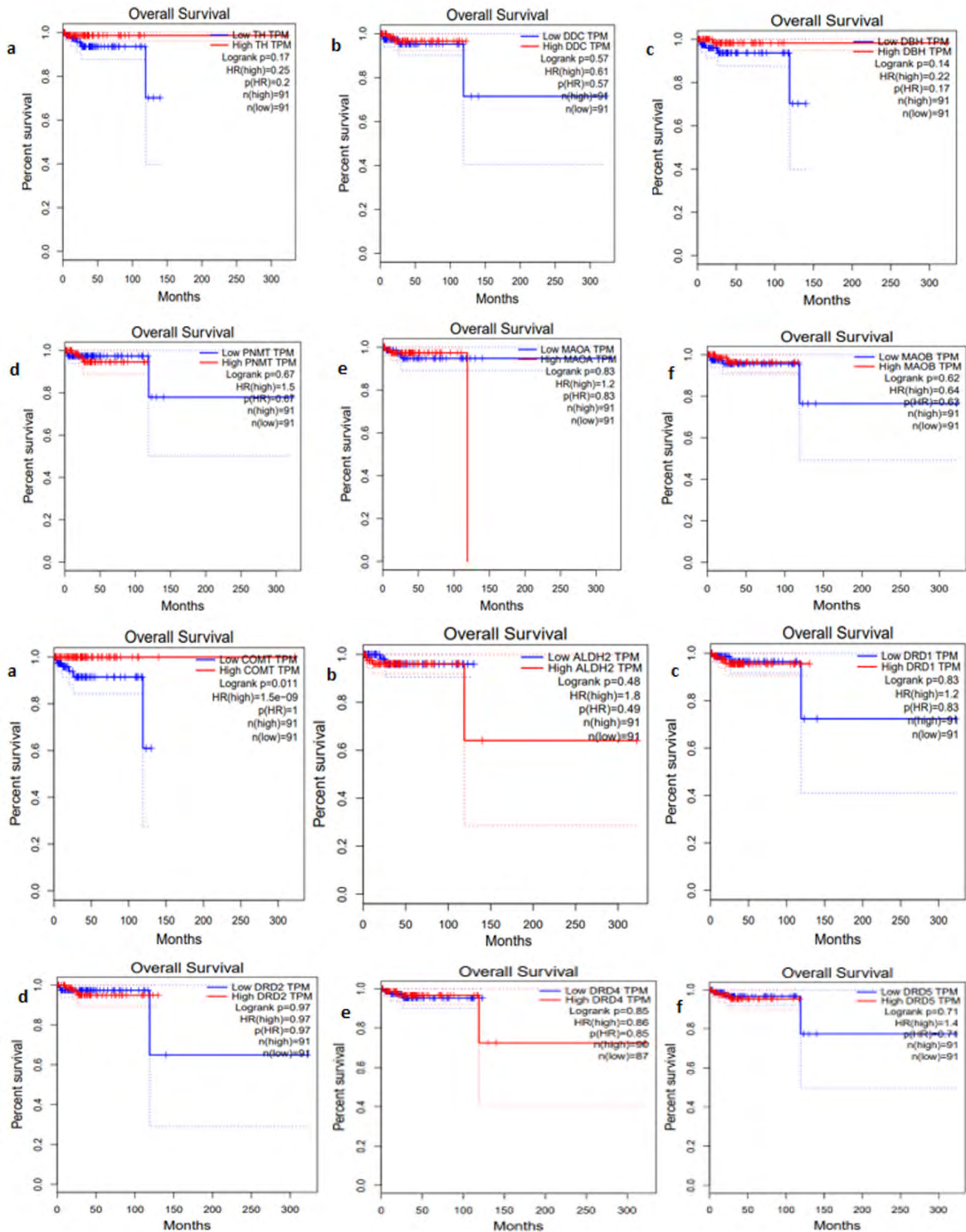


Figure 4. Associations of the genes that are associated with dopamine neurotransmission with overall survival in PCPG

sociated with dopamine neurotransmission and specifically focused on the genes that encode the main enzymes involved in DA synthesis and metabolism. High DA levels have been demonstrated in metastatic paragangliomas in consequence of reduced expression level of DBH [26]. In a study conducted with 21 PCPG patients, lower MAOA and

COMT expression levels were detected in tumor tissues [27]. It has been reported that the amounts of mRNA encoded by TH, DDC, and DBH genes were higher in pheochromocytomas compared to the normal adrenal medulla, whereas the PNMT mRNA levels were higher in the normal tissue [28]. According to the survival analysis of the current study,

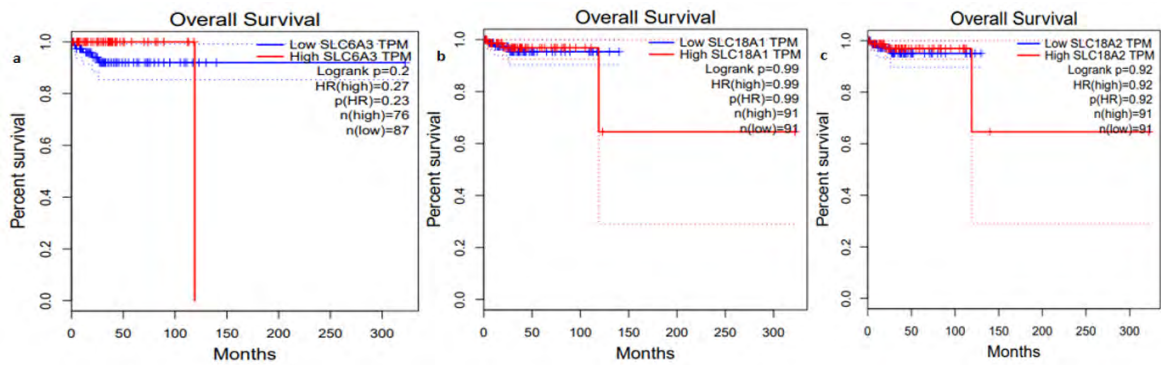


Figure 4. Continued

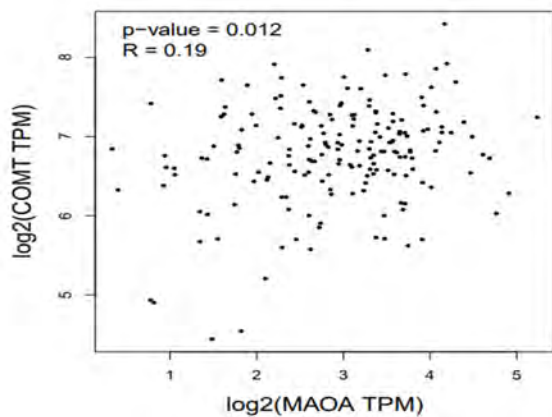


Figure 5. Spearman correlation analysis of MAOA and COMT genes with PCPG

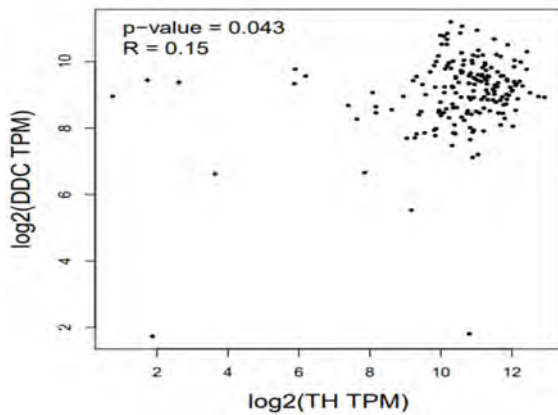


Figure 6. Spearman correlation analysis of TH and DDC genes with PCPG

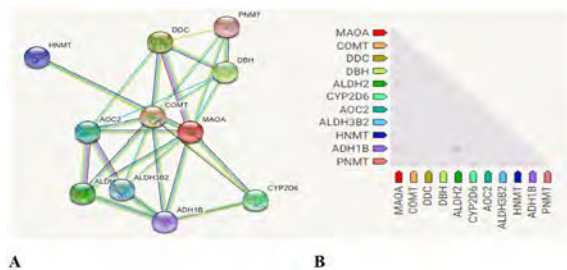


Figure 7. A. The predicted partners of MAOA B. Coexpression pattern of the genes that correlates with the gene encodes MAOA

the COMT gene was significantly less expressed in PCPG

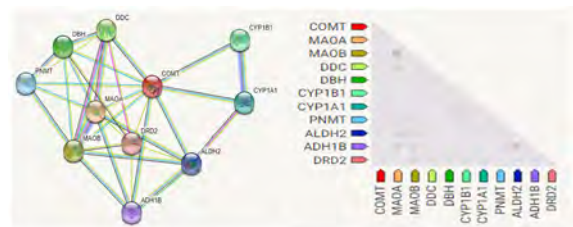


Figure 8. A. The predicted partners of COMT B. Coexpression pattern of the genes that correlates with the gene encodes COMT

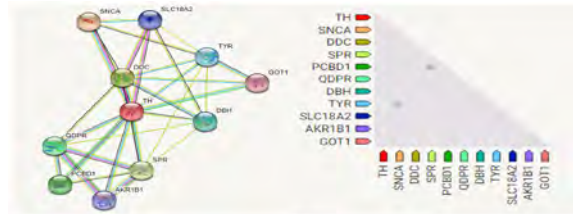


Figure 9. A. The predicted partners of TH B. Coexpression pattern of the genes that correlates with the gene encodes TH

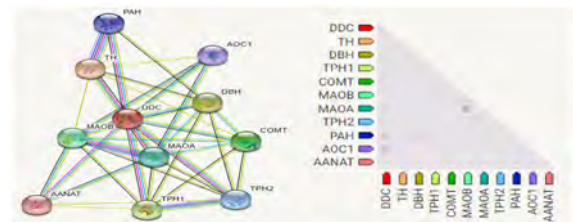


Figure 10. A. The predicted partners of DDC B. Coexpression pattern of the genes that correlates with the gene encodes DDC

compared to the normal tissue. Therefore, COMT may serve as a molecular biomarker for PCPG. DNA methylation and miRNAs directly can modulate gene expression. Based on the findings of the present study, the COMT gene has 4 CpG islands that are associated with DNA methylation. COMT protein significantly interacts with MAOA protein. hsa-miR-5000-5p regulates the expression of both COMT and MAOA genes ($p=0.00215$, $FDR=0.127$). In this regard, our findings suppose that COMT may potentially be implicated in tumor suppressive mechanism in PCPG. In patients with dopamine secreting PCPG, post-surgical observation

Table 3. The position and features of CpG islands of TH, DDC, MAOA, COMT genes

Gene	Island no	Island size	Island start	Island end	GC% percent	O/E ratio
TH	Island 1	120	103	222	50.0	0.6
	Island 2	198	292	489	50.0	0.6
	Island 3	604	583	1186	50.0	0.6
	Island 4	193	1273	1465	50.0	0.6
DDC	Island 1	257	132	388	50.0	0.6
MAOA	None					
COMT	Island 1	142	16	157	50.0	0.6
	Island 2	180	367	546	50.0	0.6
	Island 3	99	605	703	50.0	0.6
	Island 4	189	773	961	50.0	0.6

Table 4. miRNA-target enrichment analysis result for the genes associated with dopamine neurotransmission

miRNA family	p-value	FDR	Odd ratio	Number of interactions	Target Gene 1	Target Gene 2	Target Gene 3	Target Gene 4
hsa-miR-141-3p/hsa-miR-200a-3p	0.175	0.774	0.382	2	SLC18A2	DRD2		
hsa-miR-142-5p/hsa-miR-5590-3p	0.189	0.774	0.401	2	SLC18A2	DRD1		
hsa-miR-9-5p	0.330	0.774	0.586	2	DRD2	SLC18A2		
hsa-miR-30a-5p/hsa-miR-30b-5p/hsa-miR-30c-5p/hsa-miR-30d-5p/hsa-miR-30e-5p	0.139	0.774	0.443	3	COMT	SLC6A3	DRD1	
hsa-miR-5000-5p	0.00215	0.127	0.0349	2	COMT	MAOA		
hsa-miR-1-3p	0.233	0.280	0.459	2	ALDH2	TH		
hsa-miR-335-5p	0.258	0.293	0.654	4	ALDH2	DBH	DRD5	MAOB
hsa-miR-16-5p	0.469	0.494	0.775	2	ALDH2	COMT		
hsa-miR-26b-5p	0.573	0.593	0.933	2	PNMT	DRD3		

and genetic assessment has a notable effect on the prognosis of the disease. The expression values of COMT and MAOA genes, related CpG islands, and hsa-miR-5000-5p may have the potential to be used in the genetic evaluation of the pathogenesis and prognosis of PCPG. Further research is required to further enlighten the relationship between dopamine neurotransmission and the carcinogenesis of PCPG.

CONCLUSION

The present study reported that the COMT gene is significantly associated with PCPG. The findings of *in silico* analysis demonstrated that COMT might potentially be implicated in tumor suppressive mechanism. Delayed diagnosis and poorer prognosis are still a problem, and some of the tumors are recognized at autopsy. Therefore, expression analysis may be considered as a component of the clinical evaluation of patients. It requires further *in vitro* and *in vivo* dopamine neurotransmission studies in order to understand the molecular mechanism of the dopaminergic system in the pathogenesis of PCPG and

its metastases features.

CONFLICT OF INTEREST



Authors approve that to the best of their knowledge, there is not any conflict of interest or common interest with an institution/organization or a person that may affect the review process of the paper.

References

- Jochmanova I, Pacak K. Genomic landscape of pheochromocytoma and paraganglioma. *Trends Cancer* 4 (2018) 6-9.
- Kantorovich V, Pacak K. New insights on the pathogenesis of paraganglioma and pheochromocytoma [version 1; referees: 2 approved]. *F1000Research* 7 (2018) F1000.
- Su Q, Ding Q, Zhang Z, Yang Z, Qiu Y, Li X, Mo W. Identification of genes associated with the metastasis of pheochromocytoma/paraganglioma based on weighted gene coexpression network analysis. *BioMed Research International* 2020 (2020) 3876834.
- Neumann HPH, Young WF Jr, Eng C. Pheochromocytoma and

- paraganglioma. *The New England Journal of Medicine* 381 (2019) 552-565.
5. Mahata SK, Zheng H, Mahata S, Liu X, Patel KP. Effect of heart failure on catecholamine granule morphology and storage in chromaffin cells. *Journal of Endocrinology* 230 (2016) 309-323.
 6. Osinga TE, Links TP, Dullaart RPF, Pacak K, van der Horst-Schrivers ANA, Kerstens MN, Kema IP. Emerging role of dopamine in neovascularization of pheochromocytoma and paraganglioma. *FASEB Journal* 31 (2017) 2226-2240.
 7. Avsar O, Kuskucu A, Sancak S, Genc E. Are dopaminergic genotypes risk factors for eating behavior and obesity in adults? *Neuroscience Letters* 654 (2017) 28-32.
 8. Yi JW, Oh EM, Lee KE, Choi JY, Koo do H, Kim KJ, Jung KC, Kim SY, Youn YK. An exclusively dopamine secreting paraganglioma in the retroperitoneum: a first clinical case in Korea. *Journal of the Korean Surgical Society* 82 (2012) 389-393.
 9. Foo SH, Chan SP, Ananda V, Rajasingam V, Rajasingam V. Dopamine-secreting pheochromocytomas and paragangliomas: clinical features and management. *Singapore Medical Journal* 51 (2010) e89.
 10. Sayers EW, Agarwala R, Bolton EE, Brister JR, Canese K, Clark K, Connor R, Fiorini N, Funk K, Hefferon T, Holmes JB, Kim S, Kimchi A, Kitts PA, Lathrop S, Lu Z, Madden TL, Marchler-Bauer A, Phan L, Schneider VA, Schoch CL, Pruitt KD, Ostell J. Database resources of the National Center for Biotechnology Information. *Nucleic Acids Research* 47 (2019) D23-D28.
 11. Tang Z, Li C, Kang B, Gao G, Li C, Zhang Z. GEPIA: a web server for cancer and normal gene expression profiling and interactive analysis. *Nucleic Acid Research* 45 (2017) W98-W102.
 12. Szklarczyk D, Franceschini A, Wyder S, Forslund K, Heller D, Huerta-Cepas J, Simonovic M, Roth A, Santos A, Tsafou KP, Kuhn M, Bork P, Jensen LJ, von Mering J. STRING v10: protein-protein interaction networks, integrated over the tree of life. *Nucleic Acids Research* 43 (2015) D447-D452.
 13. Li LC, Dahiya R. MethPrimer: designing primers for methylation PCRs. *Bioinformatics* 18 (2002) 1427-1431.
 14. Licursi V, Conte F, Fiscono G, Paci P. MIENTURNET: an interactive web tool for microRNA-target enrichment and network-based analysis. *BMC Bioinformatics* 20 (2019) 545.
 15. Xu J, Wong CW. Enrichment Analysis of miRNA Targets, in: Ying SY. (Eds.). *MicroRNA Protocols. Methods in Molecular Biology (Methods and Protocols)*, Humana Press, Totowa, NJ, pp. 91-103, 2013.
 16. Moore L, Le T, Fan G. DNA methylation and its basic function. *Neuropsychopharmacology* 38 (2013) 23-38.
 17. van Berkel A, Lenders JW, Timmers HJ. Biochemical diagnosis of pheochromocytoma and paraganglioma. *European Journal of Endocrinology* 170 (2014) R109-R119.
 18. Tatal E, Arslan MS. Diagnosis of pheochromocytoma and paraganglioma. *Endocrinology and Diabetes Open Access* 1 (2018) 105.
 19. Soh AW, Kek PC. Dopamine-secreting carotid body paragangliomas-biochemical control with radiotherapy. *Internal Medicine* 51 (2012) 613-618.
 20. Klein MO, Battagello DS, Cardoso AR, Hauser DN, Bittencourt JC, Correa RG. Dopamine: Functions, signaling, and association with neurological diseases. *Cellular and Molecular Neurobiology* 39 (2019) 31-59.
 21. Finberg JPM. Inhibitors of MAO-B and COMT: their effects on brain dopamine levels and uses in Parkinson's disease. *Journal of Neural Transmission* 126 (2019) 433-448.
 22. Beaulieu JM, Gainetdinov RR. The physiology, signaling, and pharmacology of dopamine receptors. *Pharmacological Reviews* 63 (2011) 182-217.
 23. Gupta G, Pacak K, AACE Adrenal Scientific Committee. Precision medicine: an update on genotype/biochemical phenotype relationships in pheochromocytoma/paraganglioma patients. *Endocrine Practice* 23 (2017) 690-704.
 24. Bozin M, Lamb A, Putra LJ. Pheochromocytoma with negative metanephrines: A rarity and the significance of dopamine secreting tumors. *Urology Case Reports* 12 (2017) 51-53.
 25. Foo SH, Chan SP, Ananda V, Rajasingam V. Dopamine-secreting pheochromocytoma and paragangliomas: clinical features and management. *Singapore Medical Journal* 51 (2010) 89.
 26. Konosu-Fukaya S, Omata K, Tezuka Y, Ono Y, Aoyama Y, Satoh F, Fujishima F, Sasano H, Nakamura Y. Catecholamine synthesizing enzymes in pheochromocytoma and extraadrenal paraganglioma. *Endocrine Pathology* 29 (2018) 302-309.
 27. Grouzmann E, Matter M, Bilz S, Herren A, Triponez F, Henzen C, Kim KS, Zulewski H, Buclin T, Brack N, Abid K. Monoamine oxidase A down-regulation contributes to high metanephrine concentration in pheochromocytoma. *Journal of Clinical Endocrinology and Metabolism* 97 (2012) 2773-2781.
 28. Isobe K, Nakai T, Yukimasa N, Nanmoku T, Takekoshi K, Nomura F. Expression of mRNA coding for four catecholamine synthesizing enzymes in human adrenal pheochromocytomas. *European Journal of Endocrinology* 138 (1998) 383-387.

Mineralogy and Geochemistry of Sediments from Lake Tuz

Mehmet Yavuz Huseyinca  Suayip Kupeli 

Konya Technical University, Department of Geological Engineering, Konya, Turkey

ABSTRACT

Lake Tuz is a closed basin in the center of Anatolia (Turkey) with shallow hypersaline water. In this study, mineralogical and geochemical features of the lake sediments sampled by core drillings were investigated. Halite, polyhalite, calcite, magnesite, dolomite, huntite, quartz, and albite minerals were found in bulk sample and montmorillonite and vermiculite minerals were determined in the clay fraction XRD analyses. In geostatistical evaluations, elements are grouped into four clusters which are named Clastic, Hydrothermal, Evaporite-carbonate and Evaporite-sulfate. Trace elements included in the clastic cluster were used to constrain provenance and tectonic setting. The Light Rare Earth Element (LREE)-enriched REE pattern suggests a cratonic provenance for the lake sediments, except for the low negative Eu anomaly. Trace element ratios of La/Sc, La/Co, Th/Sc, Th/Co, Zr/Sc, Zr/Co, Ba/Sc, and Ba/Co, which are critical for provenance, show a provenance of “felsic-intermediate magmatic” composition. According to the La-Th-Sc diagram, the tectonic setting of the source area was found as “Continental Island Arc”.

Keywords:

Central Anatolia; Lake Tuz; Provenance; Sediment geochemistry; Tectonic setting

Article History:

Received: 2021/11/11

Accepted: 2021/11/30

Online: 2021/12/31

Correspondence to: Mehmet Yavuz

HÜSEYİNCA,

E-mail: myhuseyinca@ktun.edu.tr;

Phone: +90 332 205 1839;

Fax: +90 205 241 0635.

INTRODUCTION

Lake Tuz is located in the center of Anatolia (Fig. 1), and is the second largest lake of Turkey with a surface area of 1665 km². The lake includes hypersaline water, is fed by groundwater and rainwater in the autumn-winter season and without outflow [1]. The most important streams reaching the lake are Ulurmak, İnsuyu and Peçeneközü. The lake consists of two different parts; a shallow (main lake, hereafter Lake Tuz) with a large area and a deep one with a smaller area [2]. The depth of the lake water does not exceed one meter. Towards the end of the summer, approximately half of the lake floor is exposed following the evaporation of the saline water [3-6]. Also, both table salt and industrial salt are produced in the salt pans, which are separated from the lake with barriers [7].

According to Irion and Müller [8], playa sediments are largely composed of mud (silty clay) varying in colour from white through grey to black, and contains huntite, dolomite, magnesite, polyhalite, and gypsum. Uygun and Şen [9] showed that the geochemistry of the water does not show a standard composition due to the large seasonal variations. Çamur and Mutlu [10] stated that the sediments are mainly composed of gypsum, do-

lomite, huntite, magnesite, and polyhalite minerals. Kılıç and Kılıç [11] reported that the lake water is of Na-K-Mg-Cl-SO₄ type and the muddy sediments up to 20 cm deep under the salt crust contain gypsum, magnesite, thenardite, polyhalite, aragonite, and montmorillonite.

In this study, the mineralogy and geochemistry of the lake sediments, which are sampled by core drillings not exceeding one meter in depth, were investigated. It is aimed to evaluate the sediment composition by geostatistical analyses, and to infer their provenance and tectonic settings by geochemical data.

Geological Background

The current (Holocene) Lake Tuz [13] is located within the Tuzgölü basin [14-19]. The east-northeast of the lake is bordered by the Tuzgölü Fault Zone (TFZ) [20-22]. To the east of this fault zone is the Kırşehir Massif [23-30]. It is stated that the detrital material supply to the lake is mostly originates from Kırşehir Massif due to the difference in elevation [18]. The south and west of the lake are surrounded by plains, where the Quaternary aged old lake terraces take place [31].

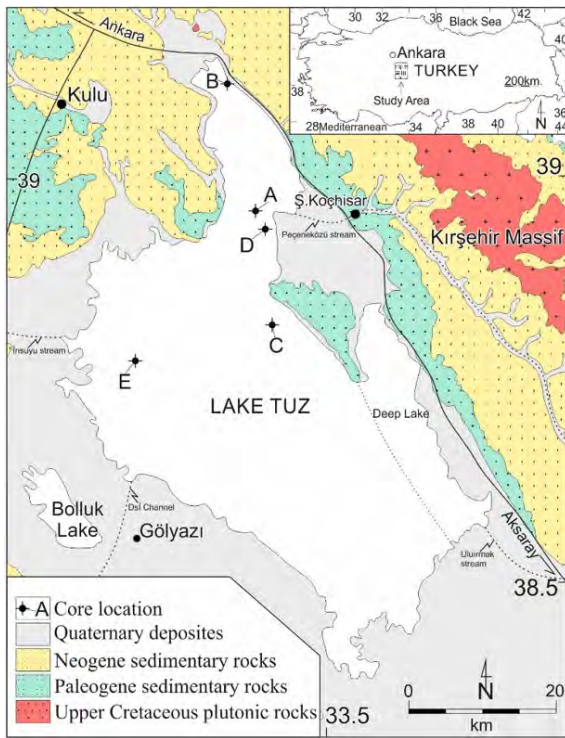


Figure 1. The geological map of the close vicinity of the Lake Tuz (modified from [12]) and the drilling locations (A-E).

MATERIAL AND METHODS

Five cores with depths varying between 48 and 78 cm were taken from the lake floor with a hand-held drilling

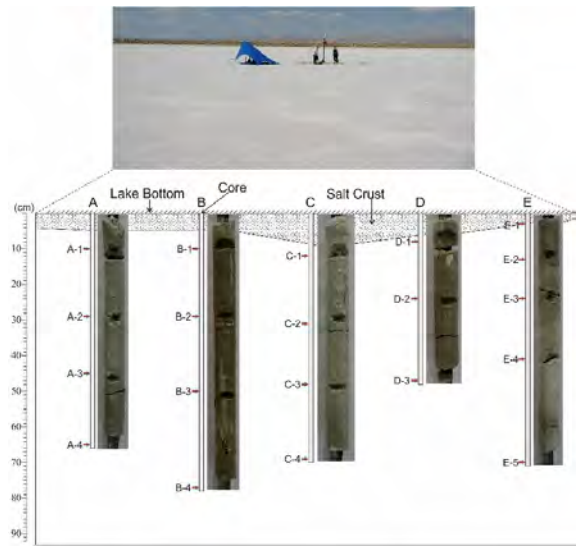


Figure 2. Sediment cores and depth of samples.

machine (Fig. 2). Samples were arranged from different depths of these cores. XRD analyses of the bulk samples were performed in MTA (Turkey) laboratories. Powdered samples were analysed with Bruker D-8 Advance brand machine that have a 2.2 kW copper X-Ray anode. XRD analyses of the clay fraction were made by standard, ethylene glycol, 300 °C heat-treated and 550 °C heat-treated samples. SEM-EDX analyses were performed in Selçuk-İLTEK (Turkey) laboratories using the ZEISS EVO-LS10 brand SEM device with EDX addition and using LaB₆ fi-

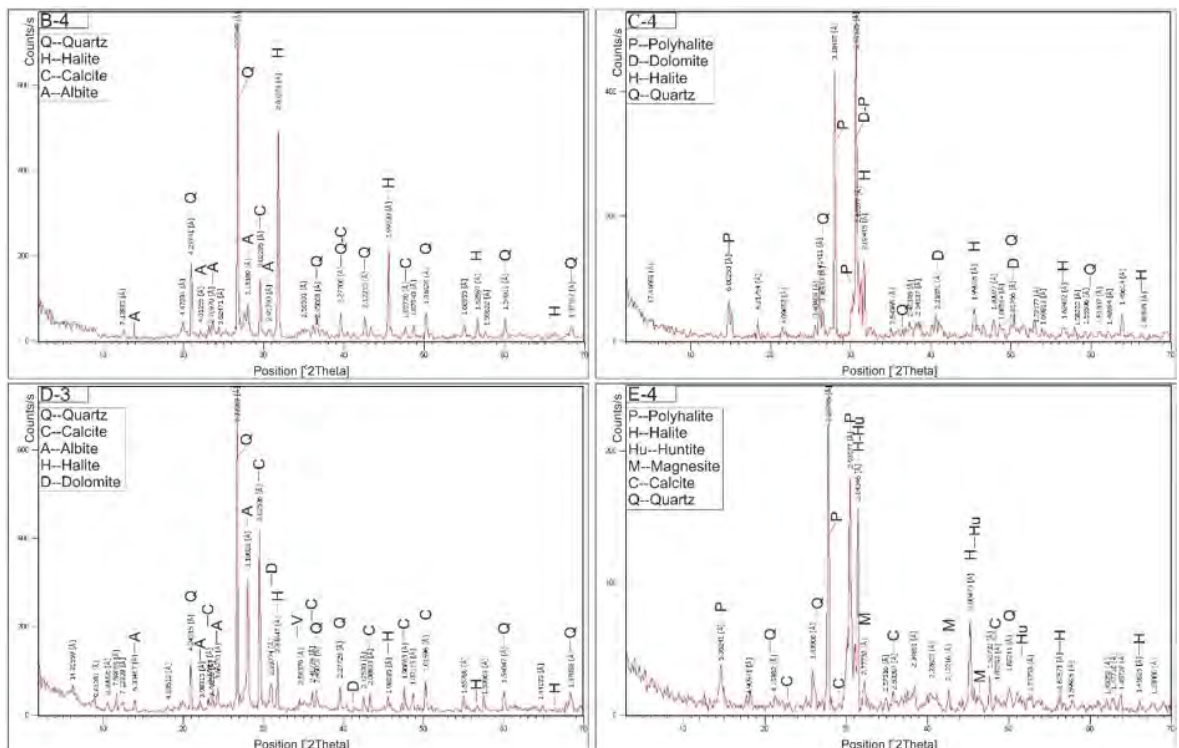


Figure 3. XRD analyses of the bulk samples from depths B-4, C-4, D-3 and E-4.

lament as an electron source. Geochemical analyses were carried out in ACME (Canada) laboratories by Lithium Borate Fusion method. A 0.2 g weighed powder sample was poured into a graphite crucible and mixed with 1.5 g of $\text{LiBO}_2/\text{Li}_2\text{B}_4\text{O}_7$ flux. The mixture was melted and then dissolved in 100 ml of 5% HNO_3 . Solution samples were analysed by ICP-ES and ICP-MS. The LOI (Loss on Ignition) was calculated by the weight difference for a 1 g. sample after ignition at 950 °C for 90 minutes. Total carbon (TOT/C) and total sulfur (TOT/S) contents were measured by Leco. Chondrite [32] and Post Archean Australian Shale (PAAS) contents [33] were used for normalization. Chondrite normalized Ce and Eu anomalies were calculated by $(\text{Ce}/\text{Ce}^*)_{\text{cn}} = [\text{Ce}_{\text{cn}} / ((\text{La}_{\text{cn}}) \cdot (\text{Pr}_{\text{cn}})^{0.5})]$ and $(\text{Eu}/\text{Eu}^*)_{\text{cn}} = [\text{Eu}_{\text{cn}} / ((\text{Sm}_{\text{cn}}) \cdot (\text{Gd}_{\text{cn}})^{0.5})]$ formulas, respectively (cn: chondrite normalized).

RESULTS AND DISCUSSION

Mineralogy

The lake sediments sampled with cores are white-grey-brown in colour. In XRD analyses of samples representing different depths, mineral compositions consisting of halite, polyhalite, calcite, magnesite, dolomite, huntite, quartz, and albite were detected (Fig. 3). In the clay fraction XRD analyses montmorillonite and vermiculite minerals were detected (Fig. 4). The presence of quartz and polyhalite crystals were observed in SEM-EDX analyses (Fig. 5).

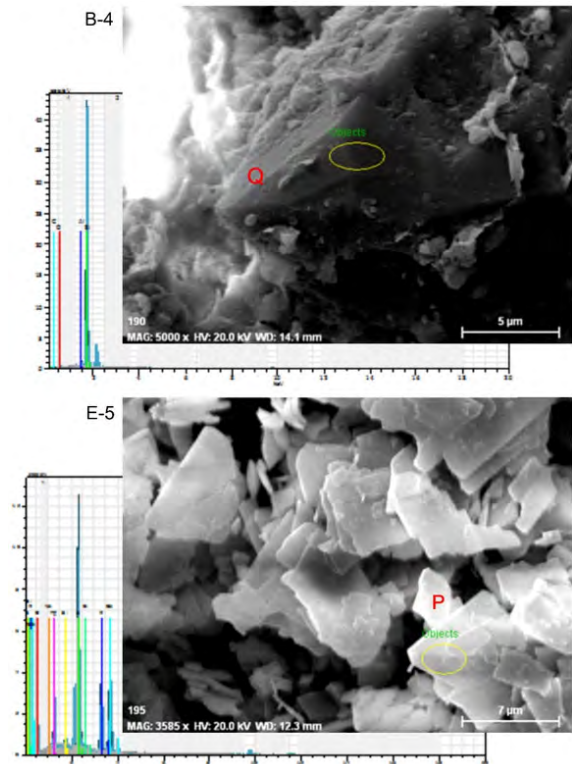


Figure 5. SEM images and EDX analyses (yellow circle) of euhehal quartz (Q) in sample B-4 and euhehal polyhalite (P) crystals in sample E-5.

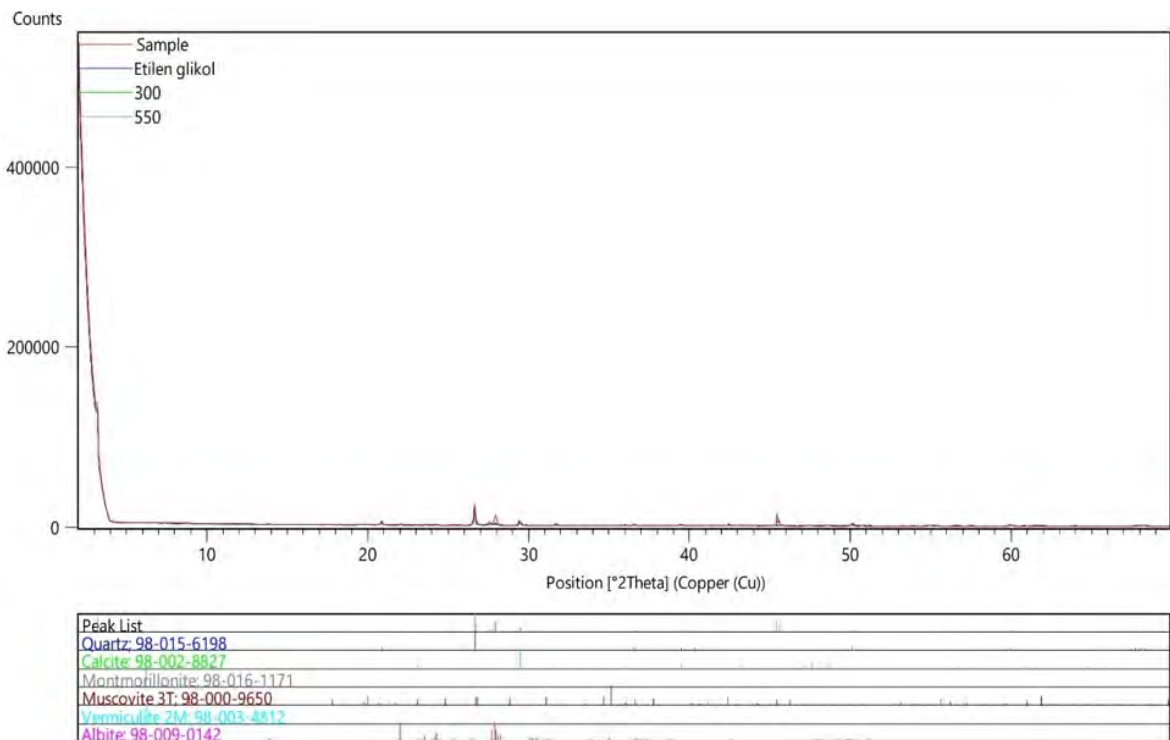


Figure 4. XRD analyses of the clay fraction.

Whole-rock Geochemistry

The major and trace element concentrations of 20 samples taken from different depths of five cores are shown in Table 1.

Major oxide concentrations were highly variable in samples (Table 1). Mineralogical compositions suggest that this variability is due to the mixture of evaporites and clastics at different ratios. In Fig. 6, the major oxides were divided by their Al₂O₃ concentrations, and compared with PAAS [34]. Such normalization may reveal major oxide enrichments originating from the evaporitic phase. Considering the sample average in the graph, Fe₂O₃/Al₂O₃, TiO₂/Al₂O₃, P₂O₅/Al₂O₃, and MnO/Al₂O₃ overlapped with that of PAAS. However, there is a significant enrichment in MgO/Al₂O₃, CaO/Al₂O₃, Na₂O/Al₂O₃, and K₂O/Al₂O₃ ratios of the samples, probably due to the evaporite minerals, as determined in XRD analyses. The slight enrichment in SiO₂/Al₂O₃ ratio is due to the abundance of quartz. In addition, the enrichment of Cr₂O₃/Al₂O₃ may indicate a contribution from an ophiolitic source [35].

The PAAS normalized plot of trace element concentrations divided by Al₂O₃ is shown in Fig. 7. In the graph, Sc/Al₂O₃, Ba/Al₂O₃, Co/Al₂O₃, Cs/Al₂O₃, Ga/Al₂O₃, Hf/Al₂O₃, Nb/Al₂O₃, Rb/Al₂O₃, Th/Al₂O₃, V/Al₂O₃, Zr/Al₂O₃, Cu/Al₂O₃, and Y/Al₂O₃ overlapped with PAAS. However, Sr/Al₂O₃, U/Al₂O₃, Mo/Al₂O₃, Pb/Al₂O₃, and Ni/Al₂O₃ were enriched. Sr enrichment may have occurred due to the evaporitic phase. The enrichment of Pb and Zn may be due to hydrothermal solutions or Pb-Zn mineralizations at the source. U and Mo may be enriched due to the redox conditions [36]. Ni may be enriched due to the ophiolitic source.

In the similarity dendrogram prepared according to the Pearson Correlation Coefficients, the variables showing strong similarity with each other form 4 clusters (Fig. 8). The first cluster consists of SiO₂, Al₂O₃, Fe₂O₃, TiO₂, P₂O₅, MnO, Cr₂O₃, Sc, Ba, Co, Ga, Hf, Nb, Rb, Th, V, Zr, Cu, Ni, and ΣREE variables; the second cluster Cs, Pb, Zn, and As variables; the third cluster consists of MgO, Na₂O, TOT/C, U, Mo, and Ce/Ce* variables; and the fourth cluster consists of CaO, K₂O, LOI, TOT/S, and Sr variables. The first cluster is named "Clastic" because of the associations with SiO₂, Al₂O₃, TiO₂, and ΣREE. The second cluster originates from possible Pb-Zn mineralization or hydrothermal solutions in the source area and was named "Hydrothermal". The third cluster was named "Evaporite-carbonate" because of its association with TOT/C. It is known that U and Mo in this cluster are enriched under reducing conditions. The Ce anomaly association shows that the elements in this group are affected from redox conditions. Finally, the fourth cluster

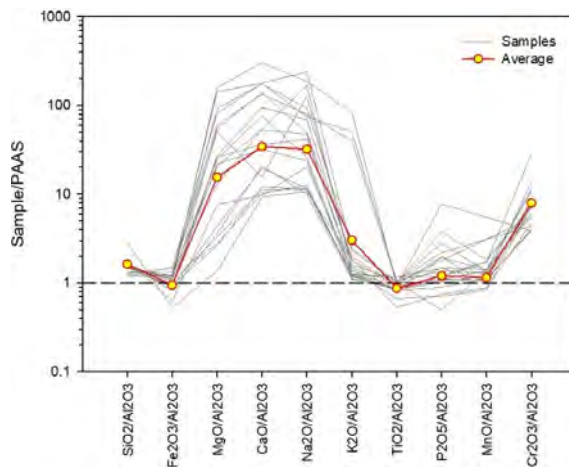


Figure 6. Element/Al₂O₃ comparison of major oxides with PAAS [34].

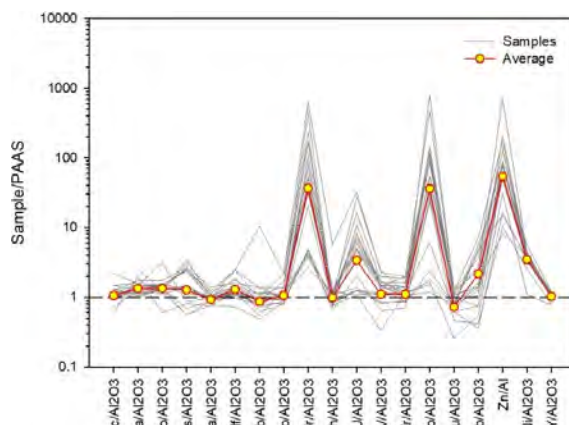


Figure 7. Element/Al₂O₃ comparison of trace elements with PAAS [34].

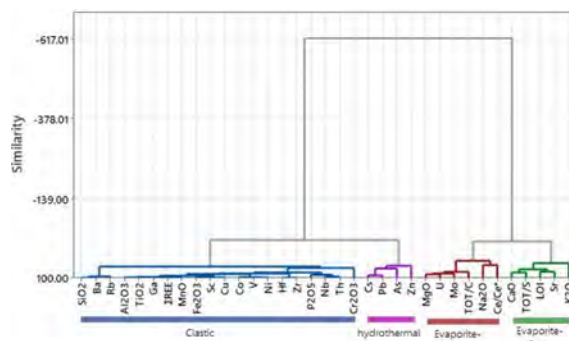


Figure 8. Dendrogram of variables

ter represents sulfates due to their association with TOT/S and was named "Evaporite-sulfate". It is understood that the LOI in this group is of gypsum origin and secondary carbonate origin due to the connection of the fourth cluster with the third cluster.

Provenance

There is a significant enrichment in the concentrations of MgO, CaO, Na₂O and K₂O which are associated with evaporites (Fig. 6). Also, they are not associated with clas-

Table 1a. Major (%) and trace element (ppm) concentrations.

	A1	A2	A3	A4	B1	B2	B3	B4	C1	C2	C3
SiO ₂	24.03	12.09	19.71	48.63	73.98	50.31	48.06	46.26	4.54	6.31	9.13
Al ₂ O ₃	4.89	2.41	3.90	8.30	7.87	9.23	9.33	9.58	0.94	1.27	1.79
Fe ₂ O ₃	1.75	0.84	1.36	2.00	1.60	3.37	3.71	4.36	0.43	0.53	0.61
MgO	12.52	7.63	11.87	7.35	1.25	2.82	3.56	3.09	15.59	13.54	11.50
CaO	10.69	15.66	9.69	5.55	5.05	7.68	7.23	6.74	11.52	15.28	16.95
Na ₂ O	7.37	10.51	10.37	10.76	5.33	6.65	6.63	7.60	14.27	7.43	5.63
K ₂ O	1.07	0.85	1.16	2.28	2.91	2.24	2.15	2.24	0.43	0.61	0.69
TiO ₂	0.22	0.12	0.17	0.29	0.22	0.40	0.42	0.45	0.05	0.07	0.09
P ₂ O ₅	0.08	0.03	0.04	0.05	0.05	0.07	0.08	0.09	0.03	0.03	0.03
MnO	0.04	0.02	0.04	0.04	0.04	0.06	0.06	0.06	0.01	0.01	0.01
Cr ₂ O ₃	0.026	0.022	0.024	0.052	0.032	0.030	0.031	0.033	0.006	0.006	0.012
LOI	24.30	27.00	21.80	14.40	1.40	16.70	18.10	4.10	27.10	27.70	25.80
Sum	87.03	77.16	80.08	99.69	99.68	99.54	99.32	84.66	74.91	72.81	72.21
TOT/C	3.15	1.79	2.74	1.29	1.01	2.03	1.98	1.72	4.38	3.47	2.89
TOT/S	4.41	11.52	6.65	4.04	0.12	0.23	0.17	0.18	4.53	7.55	8.51
Sc	4	2	3	5	4	9	10	10	1	1	2
Ba	259	114	184	371	537	377	342	326	56	66	69
Co	8	5	7	12	6	13	14	16	2	2	3
Cs	5	2	4	4	5	10	11	11	2	3	2
Ga	5	3	4	7	6	9	9	10	1	2	2
Hf	2	1	1	2	3	3	2	3	0	1	1
Nb	4	2	4	4	4	7	8	9	1	1	2
Rb	34	20	34	60	92	89	89	92	11	15	17
Sr	2242	1957	1646	406	327	410	362	265	4339	2244	1014
Th	3	2	4	4	5	7	8	9	1	1	1
U	4	2	3	3	1	2	2	2	4	3	3
V	56	32	40	42	21	60	63	88	18	17	19
Zr	55	30	38	65	99	91	88	113	12	17	28
Mo	10	7	5	12	1	1	1	1	40	8	8
Cu	8	6	9	10	5	19	19	20	3	4	4
Pb	4	2	4	4	5	12	45	50	4	2	3
Zn	1199	839	1103	386	1110	2109	3643	645	541	1186	724
Ni	58	29	42	62	25	92	93	102	11	16	19
As	39	13	11	20	17	15	25	38	22	15	15
Y	7	4	6	10	9	14	14	15	2	2	3
La	10.20	5.70	9.80	11.40	12.10	16.90	17.70	18.10	2.60	2.90	4.40
Ce	19.10	10.70	17.20	20.80	22.70	33.60	34.30	35.20	4.80	6.00	8.80
Pr	2.09	1.16	1.87	2.39	2.53	3.65	3.76	3.91	0.48	0.61	0.98
Nd	7.80	4.70	7.80	8.60	8.90	14.50	15.30	14.00	1.60	2.40	4.00
Sm	1.41	0.76	1.17	1.66	1.70	2.61	2.69	2.82	0.27	0.41	0.68
Eu	0.38	0.21	0.31	0.50	0.45	0.63	0.65	0.70	0.07	0.11	0.16
Gd	1.23	0.63	1.10	1.65	1.46	2.41	2.52	2.52	0.26	0.43	0.58
Tb	0.20	0.12	0.18	0.27	0.24	0.40	0.43	0.44	0.04	0.07	0.08
Dy	1.19	0.72	0.89	1.45	1.34	2.32	2.38	2.44	0.29	0.39	0.56
Ho	0.22	0.14	0.19	0.33	0.31	0.46	0.49	0.54	0.05	0.08	0.09
Er	0.65	0.33	0.54	0.92	0.87	1.39	1.42	1.55	0.15	0.22	0.26
Tm	0.10	0.07	0.08	0.15	0.15	0.23	0.23	0.23	0.02	0.04	0.04
Yb	0.65	0.41	0.56	0.89	0.93	1.27	1.42	1.53	0.16	0.21	0.28
Lu	0.09	0.06	0.09	0.14	0.14	0.21	0.22	0.25	0.02	0.03	0.04
ΣREE	45.31	25.71	41.78	51.15	53.82	80.58	83.51	84.23	10.81	13.90	20.95
ΣLREE/ΣHREE	9.38	9.28	10.42	7.73	8.81	8.20	8.10	7.79	9.85	8.38	9.77
(La/Yb) _{cn}	10.86	9.63	12.12	8.87	9.01	9.21	8.63	8.19	11.25	9.56	10.88
(Ce/Ce*) _{cn}	0.99	1.00	0.96	0.96	0.98	1.03	1.01	1.00	1.03	1.08	1.02
(Eu/Eu*) _{cn}	0.88	0.92	0.83	0.92	0.87	0.76	0.76	0.80	0.80	0.80	0.77

Table 1b. Major (%) and trace element (ppm) concentrations (continued). (-: below detection limits, nv: no value)

	C ₄	D ₁	D ₂	D ₃	E ₁	E ₂	E ₃	E ₄	E ₅	Average	PAAS
SiO ₂	5.86	20.87	46.55	43.03	9.56	13.37	11.62	3.14	4.59	25.08	62.80
Al ₂ O ₃	1.32	4.02	8.88	8.65	2.39	3.22	2.63	0.61	1.08	4.62	18.90
Fe ₂ O ₃	0.67	1.70	2.81	2.96	1.12	1.44	1.25	0.26	0.61	1.67	7.23
MgO	9.19	6.13	3.72	4.38	5.73	9.30	15.42	11.26	10.26	8.31	2.20
CaO	12.17	14.70	12.73	11.66	8.81	17.07	2.81	12.72	13.08	10.89	1.30
Na ₂ O	6.64	12.04	5.62	6.39	25.68	5.29	21.52	7.21	5.10	9.40	1.20
K ₂ O	10.36	1.00	1.91	2.06	0.64	0.78	0.82	10.02	10.64	2.74	3.70
TiO ₂	0.07	0.25	0.41	0.45	0.13	0.20	0.15	0.03	0.06	0.21	1.00
P ₂ O ₅	0.02	0.04	0.08	0.08	0.01	0.04	0.03	0.04	0.02	0.05	0.16
MnO	-	0.04	0.06	0.07	0.02	0.02	0.02	-	-	0.03	0.11
Cr ₂ O ₃	0.006	0.097	0.103	0.084	0.012	0.024	0.016	0.002	0.004	0.03	0.02
LOI	27.30	9.20	16.60	19.90	30.40	26.30	29.50	38.00	26.80	21.62	nv
Sum	73.59	70.06	99.51	99.73	84.50	77.01	85.74	83.32	72.27	84.64	104.59
TOT/C	0.80	2.15	2.00	2.31	1.37	2.04	3.58	1.65	1.13	2.17	nv
TOT/S	12.47	4.52	1.42	0.64	2.67	8.58	0.65	12.10	13.10	5.20	nv
Sc	1	4	7	8	3	4	3	-	2	4	16
Ba	64	211	414	363	102	179	95	54	58	212	650
Co	2	15	15	14	4	6	4	1	2	8	23
Cs	3	3	4	5	5	7	5	2	3	5	15
Ga	1	4	9	8	3	4	3	1	1	5	20
Hf	0	3	3	3	1	2	1	0	0	2	5
Nb	1	4	6	6	3	4	3	6	1	4	19
Rb	19	31	60	65	23	27	24	12	20	42	160
Sr	2427	2370	1921	445	2039	3737	882	4030	2640	1785	200
Th	1	4	6	6	2	3	2	3	1	4	15
U	2	3	2	2	2	4	3	3	1	3	3
V	15	64	75	79	28	36	31	11	14	40	150
Zr	16	84	113	110	31	73	42	14	20	57	210
Mo	7	7	3	1	7	19	20	15	5	9	1
Cu	4	9	15	15	7	7	9	2	3	9	50
Pb	2	7	3	15	7	19	20	2	3	11	20
Zn	521	1346	664	317	541	801	2065	1941	640	1116	85
Ni	17	65	89	99	27	30	31	8	14	47	55
As	10	19	5	4	19	29	34	11	8	18	nv
Y	2	7	13	13	4	6	4	1	2	7	27
La	2.90	9.70	16.30	16.00	5.60	9.50	7.10	1.90	2.80	9.18	38.00
Ce	5.40	18.60	30.30	30.60	11.40	18.60	13.60	3.90	5.00	17.53	80.00
Pr	0.60	2.14	3.37	3.36	1.22	2.02	1.43	0.40	0.53	1.93	8.83
Nd	2.30	7.40	11.70	12.50	4.70	7.90	5.70	1.30	2.00	7.26	32.00
Sm	0.44	1.51	2.47	2.47	0.86	1.23	0.98	0.26	0.37	1.34	5.60
Eu	0.10	0.36	0.65	0.67	0.20	0.30	0.25	0.07	0.10	0.34	1.10
Gd	0.39	1.42	2.25	2.10	0.78	1.16	0.85	0.29	0.36	1.22	4.70
Tb	0.06	0.21	0.39	0.38	0.12	0.17	0.13	0.04	0.06	0.20	0.77
Dy	0.42	1.17	2.10	2.07	0.63	0.98	0.71	0.19	0.31	1.13	4.40
Ho	0.06	0.22	0.44	0.44	0.12	0.20	0.12	0.04	0.05	0.23	1.00
Er	0.22	0.76	1.33	1.27	0.32	0.59	0.41	0.09	0.16	0.67	2.90
Tm	0.03	0.11	0.21	0.20	0.05	0.08	0.06	0.01	0.02	0.11	0.41
Yb	0.20	0.78	1.43	1.33	0.42	0.64	0.43	0.14	0.19	0.69	2.80
Lu	0.03	0.12	0.20	0.20	0.06	0.08	0.06	0.01	0.02	0.10	0.40
ΣREE	13.15	44.50	73.14	73.59	26.48	43.45	31.83	8.64	11.97	41.93	182.91
ΣLREE/ΣHREE	8.26	8.22	7.68	8.13	9.51	10.06	10.40	9.58	9.15	8.55	9.46
(La/Yb) _{cn}	10.04	8.61	7.89	8.33	9.23	10.28	11.43	9.40	10.20	9.17	9.40
(Ce/Ce*) _{cn}	0.98	0.98	0.98	1.00	1.05	1.02	1.02	1.07	0.98	1.00	1.05
(Eu/Eu*) _{cn}	0.73	0.75	0.84	0.89	0.74	0.76	0.83	0.77	0.83	0.82	0.65

tic cluster in close similarity (Fig. 8) Since this situation directly controls the chemical concentrations of major oxides in the clastic phase, diagrams using major oxides for provenance determination becomes useless. Therefore, trace elements whose concentrations are associated with clastic cluster were used in this study (Fig.8).

Rare earth elements (REEs) exhibit coherent, insoluble and mostly immobile geochemical behaviours in their trivalent states [33, 37]. They are transported as suspension loads or by holding to fine-grained detritus during weathering, erosion, recycling and sedimentation [38]. REEs are quantitatively transferred to the clastic sedimentary records and is subsequently unaffected by secondary processes such as diagenesis and metamorphism. [39].

Basic rocks have lower Light REE ($LREE_{La-Sm}$) contents compared to Heavy REE ($HREE_{Gd-Lu}$) and do not contain Eu anomaly. However silicic rocks have higher $LREE/HREE$ ratios and large negative Eu anomalies [40]. Due to their redox properties, Eu (+2/+3) and Ce (+3/+4) may behave differently from other trivalent REEs. The existence of the negative Eu anomaly is generally attributed to the retention of Eu by plagioclase, which is stable up to 40 km depth and under highly reducing ambient conditions. On the other hand, Ce tends to oxidize easily under surface conditions. Therefore, Ce anomaly occurs depending on whether the environment is oxidative or reductive [41].

REE concentrations of the samples are significantly lower than PAAS (Fig. 9). But the values of average $LREE/HREE$, $(La/Yb)_{cn}$, $(La/Sm)_{cn}$, and $(Gd/Lu)_{cn}$ ratios are getting closer to PAAS (Table 1). The Ce anomaly is not obvious. The effect of negative Eu anomaly is lower than that of PAAS. The specific Eu excess is probably due to plagioclase contribution from the source. The average REE pattern, which shows similarity to PAAS, except for the low negative Eu anomaly, suggests a cratonic provenance.

Elements potentially helpful for provenance identification are found in different concentrations in silicic and basic rocks. REEs, Zr, Ba and Th concentrations are higher in silicic sources, while Sc, Ni and Co concentrations are higher in basic sources [42]. These elements are also immobile and are not fractionated during sedimentary processes. Because of these features concentrations of these elements in the source rock is preserved in sediments [43].

Comparing the ratios of these preservative trace elements to each other with the average igneous rock compositions is useful to reveal the composition of the source [44]. The average values of La/Sc, La/Co, Th/Sc, Th/Co, Zr/Sc, Zr/Co, Ba/Sc, and Ba/Co ratios obtained were compared with the compositional variations (granite, felsic volcanic,

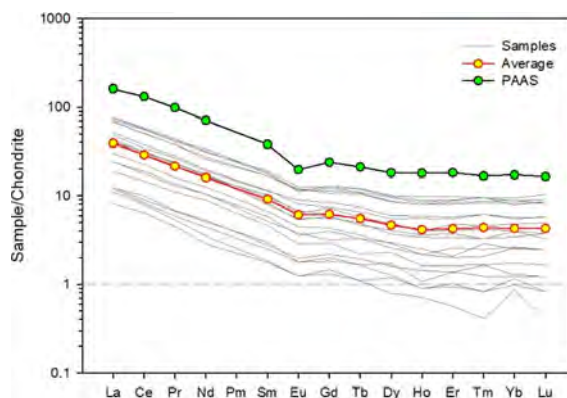


Figure 9. Comparison of REE with PAAS.

andesite and basalt) of Condie [45] (Table 2). This comparison suggests a provenance in “silicic-intermediate magmatic” composition for the lake sediments.

Considering the topographic elevation difference and the drainage network reaching the lake, the magmatic and metamorphic complex of the Kırşehir Massif in the east-northeast of the lake is the most likely the source for the sediments [27, 46-50].

Table 2. Critical element ratios for provenance.

Rocks	*Granite	*Felsic Volcanic	*Andesite	*Basalt	Tuz Lake
La/Sc	8.00	2.15	1.11	0.33	2.36
La/Co	13.33	4.67	0.91	0.31	1.37
Th/Sc	3.60	0.78	0.22	0.07	0.83
Th/Co	6.00	1.70	0.18	0.07	0.59
Zr/Sc	50.00	16.54	8.89	3.97	14.25
Zr/Co	83.33	35.83	7.27	3.74	8.45
Ba/Sc	160.00	65.38	36.11	12.42	53.55
Ba/Co	266.67	141.67	29.55	11.71	31.50

* Data from [45]

Tectonic Setting

Trace element diagrams of Bhatia and Crook [51] are frequently used to determine the tectonic setting of the source area. These diagrams were found reliable by La-Maskin et al. [52]. In this study, the La-Th-Sc diagram was used (Fig. 10). In the diagram, the tectonic settings are divided into four sections. These are A-Oceanic Island Arc, B-Continental Island Arc, C-Active continental margin, and D-Passive continental margin. In the diagram, the sample average falls on the “Continental Island Arc” region. This setting represents an arc on the continental margin along the subduction zone.

Görür et al. [18] suggested the existence of an Inner Taurus Ocean between the Menderes Taurus Block and the Kırşehir Block in the tectonic evolution model of the Tuzgölü Basin. According to this tectonic model, a continental

arc developed on the Kırşehir Block by the subduction of the Inner Taurus Ocean. The “Continental Island Arc” tectonic setting of the diagram shows that the tectonic setting of the source region coincides with the tectonic setting of Görür et al. [18].

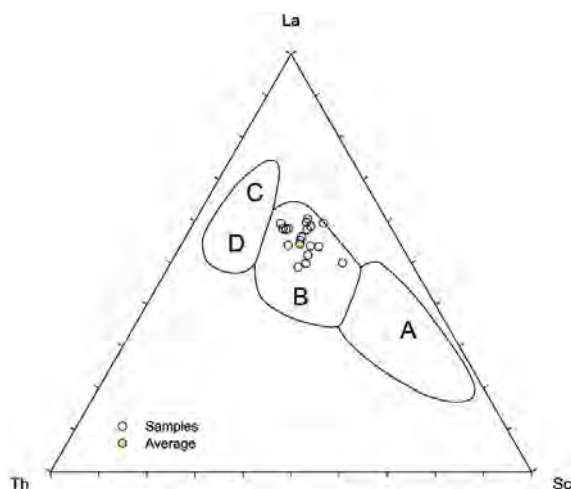


Figure 10. La-Th-Sc tectonic setting diagram [51]. A-Oceanic Island Arc, B-Continental Island Arc, C-Active continental margin, and D-Passive continental margin.

Furthermore, Yapıcı et al. [53], compared the Central Anatolian granitoids geochemically and stated that they were classified as well-developed calc-alkaline. These granitoids in the source area also support the tectonic setting model associated with the subduction.

CONCLUSION

Tuz Lake deposits sampled with cores with a depth not exceeding one meter, were determined to have halite, polyhalite, calcite, magnesite, dolomite, huntite, quartz, and albite minerals by the standard XRD analyses. In the clay fraction XRD analysis, montmorillonite and vermiculite minerals were detected. The geostatistical analyses show four groups namely Clastic, Hydrothermal, Evaporite-carbonate and Evaporite-sulfate. LREE enriched REE pattern suggests “cratonic” provenance except for the low negative Eu anomaly. The low Eu anomaly indicates that a plagioclase-rich source contributed to the sediments. Critical element ratios for provenance such as La/Sc, La/Co, Th/Sc, Th/Co, Zr/Sc, Zr/Co, Ba/Sc, and Ba/Co suggest provenance in “acidic-intermediate magmatic” composition. The most likely candidate for provenance in this composition is the Kırşehir Massif, considering the topography and catchment area. In the La-Th-Sc diagram, the tectonic setting of the source region was found as the Continental Island Arc.

ACKNOWLEDGEMENTS

This study is derived from some part of Mehmet Yavuz HÜSEYİNCA's Ph.D thesis, which was financially supported by Selçuk University Research Fund (09101002, BAP). The authors thank to anonymous reviewers for their constructive contributions to the study.

CONFLICT OF INTEREST

Authors approve that to the best of their knowledge, there is not any conflict of interest or common interest with an institution/organization or a person that may affect the review process of the paper.

AUTHOR CONTRIBUTION

First author: Conceptualization, methodology, software, investigation, writing-review and editing. Second author: Conceptualization, methodology, supervision, project administration.

REFERENCES

1. Çamur MZ, Mutlu H. Tuz Gölü'ndeki mineral çökelinin termodinamik değerlendirilmesi. *Türkiye Jeoloji Bülteni*. 38 2, (1995), 67-73.
2. Erol O. Tuz Gölü Havzasının jeoloji ve jeomorfolojisi (Genç tektonik hareketler, pluvial göl sekileri ve potas-tuz teşekkül şartları yönünden bir araştırma). TÜBİTAK, (26), 1969.
3. Ormeci C, Ekercin S. An assessment of water reserve changes in Salt Lake, Turkey, through multi-temporal Landsat imagery and real-time ground surveys. *Hydrological Processes*. 21, 11, (2007), 1424-1435.
4. Aydın F, Erlat E, Türkeş M. Impact of climate variability on the surface of Lake Tuz (Turkey), 1985–2016. *Regional Environmental Change*. 20, 2, (2020), 68.
5. Hüseyinca MY. Mineralogical and geochemical characteristics of the sediments in Lake Tuz and the close vicinity (in Turkish). Ph.D. Thesis, Selçuk University, Konya, 2015.
6. Kashima K. Environmental and climatic changes during the last 20,000 years at Lake Tuz, Central Turkey. *Catena*. 48, 1-2, (2002), 3-20.
7. Kılıç Ö, Kılıç AM. Recovery of salt co-products during the salt production from brine. *Desalination*. 186, 1, (2005), 11-19.
8. Irion G, Müller G. Huntite, dolomite, magnesite, and polyhalite, of recent age from Tuz Gölü, Turkey. *Nature*. 220, (1968), 1309-1310.
9. Uygun A, Şen E. Tuz Gölü Havzası ve doğal kaynakları I: Tuz Gölü suyunun jeokimyası. *Bulletin of the Geological Society of Turkey*. 21, (1978), 113-120.
10. Çamur MZ, Mutlu H. Major-ion geochemistry and mineralogy of the Salt Lake (Tuz Gölü) basin, Turkey. *Chemical geology*. 127, 4, (1996), 313-329.
11. Kılıç Ö, Kılıç AM. Salt crust mineralogy and geochemical evolution

- of the Salt Lake (Tuz Gölü), Turkey. *Scientific Research and Essays*. 5, 11, (2010), 1317-1324.
12. Şenel M. *Türkiye Jeoloji Haritası/Geological Map of Turkey*, scale 1:500,000, Maden Tetkik Arama Genel Müdürlüğü, Ankara, 2002.
 13. Tekin E, Ayyıldız T, Gündoğan İ, Orti F. Modern halolites (halite oolites) in the Tuz Gölü, Turkey. *Sedimentary Geology*. 195, 3, (2007), 101-112.
 14. Aydemir A, Ateş A. Structural interpretation of the Tuzgolu and Haymana Basins, Central Anatolia, Turkey, using seismic, gravity and aeromagnetic data. *Earth Planets and Space*. 58, 8, (2006), 951-961.
 15. Arıkan Y. Tuz Gölü havzasının jeolojisi ve petrol imkanları. *M.T.A. Dergisi*. 85, (1975), 17-38.
 16. Aydemir A. Hydrocarbon potential of the Tuzgolu (Salt Lake) Basin, Central Anatolia, Turkey: A comparison of geophysical investigation results with the geochemical data. *Journal of Petroleum Science and Engineering*. 61, 1, (2008), 33-47.
 17. Clark M, Robertson A. Uppermost Cretaceous–Lower Tertiary Ulukışla Basin, south-central Turkey: sedimentary evolution of part of a unified basin complex within an evolving Neotethyan suture zone. *Sedimentary Geology*. 173, 1, (2005), 15-51.
 18. Görür N, Oktay FY, Seymen İ, Şengör AMC. Palaeotectonic evolution of the Tuzgölü basin complex, Central Turkey: sedimentary record of a Neo-Tethyan closure, In: J. E. Dixon A. H. F. Robertson (Eds.), *The geological evolution of the eastern mediterranean*, Geological Society Special Publications, London, pp. 467-482, 1984.
 19. Çemen I, Göncüoğlu MC, Dirik K. Structural evolution of the Tuzgölü basin in Central Anatolia, Turkey. *The Journal of geology*. 107, 6, (1999), 693-706.
 20. Yıldırım C. Relative tectonic activity assessment of the Tuz Gölü Fault Zone; Central Anatolia, Turkey. *Tectonophysics*. 630, (2014), 183-192.
 21. Fernandez-Blanco D, Bertotti G, Çiner A. Cenozoic tectonics of the Tuz Gölü basin (central Anatolia plateau, Turkey). *Turkish Journal of Earth Sciences*. 22, 5, (2013), 715-738.
 22. Dirik K, Erol O. Tectonomorphologic evolution of Tuzgölü and surrounding area, central Anatolia-Turkey. *Turkish Association of Petroleum Geologists Special Publication*. 5, (2003), 27-46.
 23. Seymen İ. Kaman dolayında Kırşehir Masifinin jeolojisi. *Doçentlik Tezi*, İ.T.Ü. Maden Fakültesi, İstanbul, 1982.
 24. Göncüoğlu MC. Structural and stratigraphic framework of the central Anatolian Tertiary Basins. *IGCP Project Early Paleogene Benthos Third Meeting*, Ankara. 1992.
 25. Koçak K, Zedef V, Kansun G. Magma mixing/mingling in the Eocene Horoz (Nigde) granitoids, Central southern Turkey: evidence from mafic microgranular enclaves. *Mineralogy and Petrology*. 103, 1-4, (2011), 149-167.
 26. Okay AI, Tüysüz O. Tethyan sutures of northern Turkey. *Geological Society, London, Special Publications*. 156, 1, (1999), 475-515.
 27. Kuşçu İ, Gençlioğlu Kuşçu G, Meinert LD, Floyd PA. Tectonic setting and petrogenesis of the Çelebi granitoid, (Kırıkkale-Turkey) and comparison with world skarn granitoids. *Journal of Geochemical Exploration*. 76, 3, (2002), 175-194.
 28. Göncüoğlu MC, Toprak V, Kuşçu İ, Erler A, Olgun E. Geology of the western part of the central Anatolian Massif, Part 1: Southern part. *Turkish Petroleum Corporation (TPAO)*, 1991.
 29. Kocak K, Leake BE. The petrology of the Ortakoy district and its ophiolite at the western edge of the Middle anatolian Massif, Turkey. *Journal of African Earth Sciences*. 18, 2, (1994), 163-174.
 30. Kocak K, Isık F, Arslan M, Zedef V. Petrological and source region characteristics of ophiolitic hornblende gabbros from the Aksaray and Kayseri regions, central Anatolian crystalline complex, Turkey. *Journal of Asian Earth Sciences*. 25, 6, (2005), 883-891.
 31. Kashima K. The quantitative reconstruction of salinity changes using diatom assemblages in inland saline lakes in the central part of Turkey during the Late Quaternary. *Quaternary International*. 105, 1, (2003), 13-19.
 32. Anders E, Grevesse N. Abundances of the elements: Meteoritic and solar. *Geochimica et Cosmochimica Acta*. 53, 1, (1989), 197-214.
 33. Taylor SR, McLennan SM. *The continental crust: Its composition and evolution*, Blackwell Scientific Publications, Oxford, 1985.
 34. Cullers RL. The geochemistry of shales, siltstones and sandstones of Pennsylvanian-Permian age, Colorado, USA: implications for provenance and metamorphic studies. *Lithos*. 51, 3, (2000), 181-203.
 35. Hiscott RN. Ophiolitic source rocks for Taconic-age flysch: Trace-element evidence. *Geological Society of America Bulletin*. 95, 11, (1984), 1261-1267.
 36. Hallberg RO. A Geochemical Method for Investigation of Paleoredox Conditions in Sediments. *Ambio Special Report*. 4, (1976), 139-147.
 37. Cullers RL. The controls on the major- and trace-element evolution of shales, siltstones and sandstones of Ordovician to tertiary age in the Wet Mountains region, Colorado, U.S.A. *Chemical geology*. 123, 1-4, (1995), 107-131.
 38. McLennan SM, Taylor SR. Sedimentary rocks and crustal evolution: Tectonic setting and secular trends. *The Journal of geology*. 99, 1, (1991), 1-21.
 39. Condie KC. Another look at rare earth elements in shales. *Geochimica et Cosmochimica Acta*. 55, 9, (1991), 2527-2531.
 40. Cullers RL, Graf JL. Rare earth elements in igneous rocks of the continental crust: predominantly basic and ultrabasic rocks, In: *Rare earth element geochemistry*, Elsevier Amsterdam, pp. 237-274, 1984.
 41. McLennan SM, Taylor SR. Geology, geochemistry and natural abundances of the Rare Earth Elements, In: D. A. Atwood R. A. Scott (Eds.), *Encyclopedia of Inorganic and Bioinorganic Chemistry*, John Wiley & Sons, Ltd, pp. 19, 2012.
 42. Cullers RL, Podkovyrov VN. The source and origin of terrigenous sedimentary rocks in the Mesoproterozoic U1 group, southeastern Russia. *Precambrian Research*. 117, 3-4, (2002), 157-183.
 43. Armstrong-Altrin JS, Lee YI, Verma SP, Ramasamy S. Geochemistry of Sandstones from the Upper Miocene Kudankulam Formation, Southern India: Implications for Provenance, Weathering, and Tectonic Setting. *Journal of Sedimentary Research*. 74, 2, (2004), 285-297.
 44. Cullers RL, Basu A, Suttner LJ. Geochemical signature of provenance in sand-size material in soils and stream sediments near the Tobacco Root batholith, Montana, U.S.A. *Chemical geology*. 70, 4, (1988), 335-348.
 45. Condie KC. Chemical composition and evolution of the upper continental crust : Contrasting results from surface samples and shales. *Chemical geology*. 104, (1993), 1-37.
 46. Boztuğ D, Harlavan Y. K–Ar ages of granitoids unravel the stages of Neo-Tethyan convergence in the eastern Pontides and central Anatolia, Turkey. *International Journal of Earth Sciences*. 97, 3, (2008), 585-599.
 47. Boztuğ D, Jonckheere RC, Heizler M, Ratschbacher L, Harlavan Y, Tichomirova M. Timing of post-obduction granitoids from intrusion through cooling to exhumation in central Anatolia, Turkey. *Tectonophysics*. 473, 1, (2009), 223-233.
 48. Köksal S, Romer RL, Göncüoğlu MC, Toksoy-Köksal F. Timing of post-collisional H-type to A-type granitic magmatism: U–Pb titanite ages from the Alpine central Anatolian granitoids (Turkey).

- International Journal of Earth Sciences. 93, 6, (2004), 974-989.
49. Koçak K, Zedef V. Interaction of the lithospheric mantle and crustal melts for the generation of the Horoz pluton (Niğde, Turkey): whole-rock geochemical and Sr-Nd-Pb isotopic evidence. *Estonian Journal of Earth Sciences*. 65, 3, (2016), 138-160.
 50. Nurlu N, Yapıcı N. Ortaköy Granitoidi'nin petrografik ve jeokimyasal özellikleri (Yaylak/Aksaray). *Çukurova Üniversitesi Mühendislik Mimarlık Fakültesi Dergisi*. 29, 2, (2014), 69-78.
 51. Bhatia MR, Crook KAW. Trace element characteristics of graywackes and tectonic setting discrimination of sedimentary basins. *Contributions to Mineralogy and Petrology*. 92, 2, (1986), 181-193.
 52. LaMaskin TA, Dorsey RJ, Vervoort JD. Tectonic controls on mudrock geochemistry, Mesozoic rocks of eastern Oregon and western Idaho, USA: Implications for cordilleran tectonics. *Journal of Sedimentary Research*. 78, 12, (2008), 765-783.
 53. Yapıcı N, Nurlu N, Güneş H. Comparison of Ortaköy/Yaylak granitoid (Aksaray) with the other intrusions. Paper presented at the 2. international Turkish world engineering and science congress, Antalya. 7-10 November, pp. 252-260, 2019.

Expression Analysis of Some Stress-Related Genes Induced by Cadmium on Tomato (*Solanum Lycopersicum L.*) Plants

Ekrem Bolukbasi^{1,2} 

¹Amasya University, Department of Environmental Protection and Technologies, Amasya, Turkey

²Amasya University, Central Research Laboratory, Amasya, Turkey

ABSTRACT

Environmental pollution occurs in nature as air, soil and water pollution and as a result it affects whole ecosystem including human beings. Although industrialization and technological developments have made life easier than before, in recent years, they have triggered environmental pollution. Cadmium, which is a toxic pollutant for all living things, is one of the most important element in heavy metal pollutants. In this study, it was aimed to determine gene expression changes in tomato plant under Cd stress. Molecular response of tomato plants to Cd stress was examined by transcript accumulation analysis of two stress-related genes: (i) MT-2 (metallothionein-2) gene encodes metal binding protein and (ii) The GR-1 (glutathione reductase-1) gene encodes the glutathione reductase enzyme and is a marker of the ROS scavenging mechanism. Expression differences in MT-2 and GR-1 genes in tomato seedlings exposed to cadmium stress at different concentrations ranging from 20 to 1280 mg L⁻¹ for 24 hours were determined performing quantitative real-time PCR. The results obtained from this study were showed that MT-2 and GR-1 genes play an important role in the mechanism of protection against heavy metal of Cd stress. In addition, the physiological properties of tomato have been associated with cadmium accumulation.

Keywords:

Cadmium stress; Tomato; Metallothionein; Glutathione reductase; qRT-PCR

INTRODUCTION

Tomato is an important fruit crop grown mainly as an annual and economically valuable plant for growers in the Mediterranean basin (*Solanum lycopersicum L.* formerly *Lycopersicon esculentum Mill.* belongs to the Solanaceae family). It is an important source of vitamins, minerals, fiber and a dietary antioxidants [1]. It is also among the anti-carcinogenic foods due to the carotenoids it contains. Consumed as fresh and dried fruit, tomatoes are also processed in industry as tomato paste. Turkey, Egypt, Italy, Spain, Greece and Morocco are among the world's largest tomato producers and exporters [2].

With the increasing population, unplanned urbanization and developing technology, heavy metal pollution has become an important environmental problem worldwide. In addition to these, as a result of industrial activities, mining, using pesticide in agriculture, metallurgy, combustion of fossil fuels, faulty waste disposal, metal-enriched some materials, automotive emissions and domestic wastes and many other factors [3-5]. He-

avy metal pollution, one of the most important environmental pollutants, is reported to accumulate in soil and water at high concentration, causing genotoxicity and damage to many functional biomolecules in living things. Heavy metals, which accumulate intensely in soil and water ecosystems, can be included in the food chain, especially by means of plant-based nutrients [6,7]. Thus, the heavy metals included in the food chain, may deteriorate the structure of many biomolecules such as proteins, enzymes and especially nucleic acids [8-11].

Very few metals such as Zinc, Copper, Nickel, Manganese and Iron are required nutrients in low concentrations for plant life and normal growth. This situation is similar for humans and animals, too [12,13]. These metals act as co-factors for many enzymes in most metabolic pathways. Especially in the structural and catalytic functions of proteins. On the other hand, the presence of the same metals in high concentrations in tissues causes toxic effects [10,14]. Thus, it adversely affects many biological molecules. For example, reactive

Article History:

Received: 2021/11/11

Accepted: 2021/12/20

Online: 2021/12/31

Correspondence to: Ekrem Bolukbasi,

Amasya University, Department

of Environmental Protection and

Technologies, 05100, Amasya, Turkey.

E-Mail: ekrem.bolukbasi@amasya.edu.tr

Phone: +90 (358) 211 5043

Fax: +90 (358) 417 7794

oxygen species (ROS) such as hydrogen peroxide and singlet oxygen formed due to heavy metal toxicity, cause conformational changes in enzymes involved in important metabolic formation pathways such as protein and nucleic acid. This causes oxidative damage, impairment of cellular homeostasis and stress, in plants as well as in many living things [15-17]. Cadmium (Cd) heavy metal in particular is a highly toxic pollutant for all living things, especially plants. Cadmium, which is not an essential element especially for plants, is generally found in low amounts in the soil and adversely affects plant growth and development. It is not an essential nutrient for plants, but it quickly enters the cells. This metal has some serious effects on plants such as growth inhibition, decrease in enzyme activities, photosynthesis and nutrient intake. Cadmium accumulated in plant tissues can cause serious damage to biological molecules such as proteins, enzymes and nucleic acids [6,18-20]. For example; ROS formed via cadmium stress may cause changes such as incompatibilities in DNA bases and instability of the double helix structure [16,21]. This causes changes in the expression of some genes that play a role in dealing with stress caused by heavy metal pollution. This change in gene expression allows plants to cope with stress [3,7,22-24].

In the present work, gene expression changes due to Cd stress in tomato plant were analyzed by examining two different stress-related genes. (i) MT-2 (metallothionein-2) gene encodes metal binding protein and (ii) The GR-1 (glutathione reductase-1) gene encodes the glutathione reductase enzyme and is a marker of the ROS scavenging mechanism [9,25-28].

Metallothionein is a protein that combines with metals to form complex structures as chelators. Many studies have shown that metallothioneins are highly expressed in metallophyte tolerant plant varieties. Thus, the plants can protect themselves against metal stress [26-29]. These metallothionein proteins are able to bind heavy metals by the thiol groups in the cysteine residue. Also, metallothionein proteins are involved in scavenging of ROS. Glutathione reductase is an enzyme that reduces oxidized glutathione. Glutathione reductase, an enzyme especially active in the ascorbate-glutathione (ASH-GSH) pathway, plays a role in defense against ROS by maintaining the low status of GSH [30]. By determining the changes in gene expression levels of metallothionein and glutathione reductase in plants, the tolerance of plants to various types of stress can be determined [29-33].

The results suggest that the early molecular response of hydroponically cultivated tomato plants might develop different strategies to cope with Cd toxicity by manipulating the expression level of stress-related genes. Therefore, in this study, changes in metallothionein and glutathione

reductase genes in tomato seedlings exposed to cadmium heavy metal stress at different concentrations for a certain period of time were demonstrated. The quantitative real-time PCR technique was performed to determine the change in gene expression levels. Finally, the data obtained from the study; showed that the change in the expression levels of these genes in the tomato plant could serve as an additional Cd-tolerance mechanism to deal with the toxic effect of cadmium.

MATERIALS AND METHODS

Growth of Plant Samples and Cadmium Stress Treatments

Before planting tomato seeds, their surfaces were sterilized with 70 % alcohol and 30 % sodium hypochlorite solution. The seeds were then washed three or four times with distilled water. For the germination and growth of tomato seeds, viols prepared using sterile perlite were arranged. Tomato seeds were germinated in sterile perlite by irrigating with 0.2 L modified 1/10 Hoagland solution and grown hydroponically. Tomato seeds planted in three biological replicates were grown in a controlled environmental growth chamber at 23-26 °C with 250 mmol m⁻² s⁻¹ photosynthetic photon flux and 50-60 % relative humidity. After 21 days of growing period, tomato seedlings were exposed to cadmium solution at different concentrations of 20, 40, 80, 160, 320, 640, 1280 mg L⁻¹ in the growth chamber for 24 hours. At the end of the 24 hour period, the roots and shoots of tomato seedlings were harvested and stored at -80 °C until RNA isolation.

Root and shoot fragments (~200 mg) taken from samples which exposed to cadmium stress were powdered using liquid nitrogen. Subsequently, RNA was isolated from these samples. For RNA extracting, Trizol RNA extraction protocol was followed by RNeasy mini kit (Qiagen, Cat no: 74104) to cleanup. Quantity and quality measurement of isolated genomic RNAs were determined by Nanodrop (NanoDrop ND-1000 Spectrophotometer, Thermo Scientific). And then it was confirmed by 1.5 % agarose (containing 0.05 µl ml⁻¹ EtBr) gel electrophoresis.

First Strand cDNA Synthesis Assay

For the first strand cDNA synthesis assay, a two-step procedure was performed for real-time reverse transcriptase-polymerase chain reaction (RT-PCR). The reverse transcription reaction was performed using a high quality cDNA synthesis kit (Roche). According to the protocol; 2 µg isolated RNA, 2.5 µM Anchoredoligo (dT)18, 1X Transcriptor High Fidelity Reverse Transcriptase Reaction Buffer, 20 U RNase Inhibitor, 1 mM deoxynucleotide

mix and 10 U Transcriptor high fidelity reverse transcriptase were used. Quantity and quality measurements of cDNA were determined by Nanodrop (NanoDrop ND-1000 Spectrophotometer, Thermo Scientific).

The Quantitative Real-time PCR Analysis of GR-1 and MT-2 Genes

Following cDNA synthesis, Real-Time PCR applications were performed using SYBR Green I Master dye via Light Cycler Nano (Roche) device. Sequences of the target genes identified in the study were searched/determined from the NCBI database and primers specific to these regions were designed using the Primer-3 program [36]. The designed primers were commercially synthesized. In addition, the Actin (ACT) gene was selected as the housekeeping gene to be used in the normalization process. During the Real-Time PCR reaction, Melting curve analysis was performed to determine the efficiency of PCR and to observe if there was any dimer formation, following the quantification (quantification = determination of expression) performed using SYBR Green I dye. Before starting the actual experimental work, the optimization of the reaction conditions was ensured. As a result of the experiments, the most suitable primer and cDNA concentrations were determined. The sequences and melting temperatures (T_m) of the primers used throughout the reactions are given in Table-1 and the homology analysis information of the qRT-PCR amplified transcripts in the NCBI database are given in Table 2.

Table 1. Sequences and melting temperatures of primers used in qRT-PCR

Genes/Primers name	Sequence (5'-3')	T _m (°C)
MT-2F	GCTGTGGATCTAGCTGCAAGTGCG	58-60
MT-2R	AAGGGTTGCACTGCAGTCAGATC	
GR-1F	CGTGCTGTGATACTTGGTGG	58-60
GR-1R	TCGTGCAAGGATGCATAGTG	
ACT-F	GGGATGGAGAAGTTGGTGGTGG	58-60
ACT-R	CTTCGACCAAGGGATGGTGTAGC	

Real-Time PCR reactions were performed in triplicate (as technical iterations) using the optimal conditions obtained as follows were initial denaturation 10 minutes at 95 °C, (40 cycles) 95 °C for 10 seconds, 58-60 °C for 20 seconds, 72 °C for 20 seconds, and increasing incrementally from 55 °C to 95 °C temperature 0.5 °C min⁻¹.

Normalization and Statistical Analysis of Real-Time PCR Results

Gene expression results determined as Ct (Cycle Tresh-

Table 2. Homology analysis information of qRT-PCR amplified transcripts in NCBI database.

Genes	Length	Homology	Accession no.
MT-2	170 bp	<i>Solanum lycopersicum</i> type 2 metallothionein mRNA, partial cds	EU884310
GR-1	87 bp	<i>Solanum lycopersicum</i> glutathione reductase mRNA, partial cds	FJ265823
ACT	398 bp	<i>Solanum lycopersicum</i> ACT mRNA for actin, partial cds	AB199316.1

hold) value, ACT (actin) and control conditions used in the study were normalized by considering housekeeping gene (Livak and Schmittgen 2001). The obtained data were normalized according to the 2-ΔΔCt method of Livak and Schmittgen [37].

ANOVA, Tukey and Dunnett multiple comparison tests were performed to reveal differences between groups. The homogeneity of variances was determined with the statistical program (IBM SPSS Statistic-21) and Levene's test. The post-hoc Tukey HSD and Dunnett test were applied to the homogeneously distributed variables (also Dunnett's test to confirm the results) and the Dunnett T3 test was applied to the non-homogeneously distributed variables. P < 0.05 was considered to be statistically significant.

RESULTS AND DISCUSSION

It is one of the most important effects of heavy metal toxicity known to inhibit root and shoot development. The toxicity of heavy metals due to increased concentrations negatively affects the development of roots and shoots and seed germination in plants. Similarly, regression in root development of tomato plants used in the study was detected. As expected, these results are similar to previous studies [8,9,16,30].

Metallothionein binding proteins (MTs) protect plants from metal stress and toxicity. Numerous studies have shown that MTs are highly expressed in many plants exposed to heavy metal toxicity [7,8,27]. Cysteine residue has the ability to bind heavy metals both physiologically (such as zinc, copper, and selenium) and xenobiotically (such as cadmium, mercury, silver, and arsenic) via thiol groups. In addition, it has been reported that MTs have important roles in both metal chaperoning and scavenging of ROS [28]. Many studies have shown that arsenic, cadmium and copper stresses induce metallothionein expression and accumulation [26,27,29].

Glutathione reductase (GR) is an important enzyme in the ASH-GSH (Ascorbate-Glutathione) pathway in enzymatic antioxidant system in plants, as in many living things. It plays a critical role in the defense system against

ROS, which occurs as a result of stress factors, by maintaining the GSH level and acts as a substrate for glutathione-S-transferases. In many recent studies, it was stated that GR-1 expression increased against cadmium stress in various plants [7,9,31-35].

Considering the mRNA expression profiles of genes (MT-2 and GR-1) and actin (ACT) used as a housekeeping gene and control conditions of root and shoot samples of tomato plants with different concentrations of cadmium (Cd) stress applied by Real-time PCR (Light CyclerNano, Roche). Normalized according to the $2^{-\Delta\Delta Ct}$ method of Livak and Schmittgen [37]. In addition, the quantification and melting curve analysis of the transcripts are given in Figure 1. Normalized gene expression data were averaged and according to the results obtained, the changes in the concentration-dependent expression level of MT-2 and GR-1 genes occurring in different tissues of each tomato samples were shown on the graphs. For accuracy of results, MT-2, GR-1 and ACT transcript levels of all samples were measured in triplicate for different concentration of cadmium stress.

In this current study, different amounts of GR-1 accumulation were observed depending on varying concentration ranges in roots and shoots samples taken from tomato seedlings exposed to cadmium heavy metal stress. When the GR-1 expression data in both root and shoot parts were evaluated; The changes in the expression levels of the GR-1 gene, depending on the concentration, in the root samples of tomato seedlings subjected to cadmium stress are given in the Figure 2. Compared to the control group, the GR-1 gene expression level was approximately 5.9 and 7.8-fold, with the highest concentrations of 160 and 320 mg L⁻¹, and the lowest at 1280 mg L⁻¹ concentration, approximately 1.5-fold. GR-1 gene expression change in shoots; it was detected at the highest level with 80 mg L⁻¹ and 320 mg L⁻¹ concentrations, 8.8 and 11.9 fold, respectively. Similarly, fold change was observed as 7.0 fold at 160 mg L⁻¹ concentration. On the other hand, the lowest expression data is; it was detected at the concentration of 1280 mg L⁻¹ with approximately 0.9 fold (Figure 2).

Additionally, the GR-1 expression data in root and shoot samples were examined; an abruptly decrease was observed after the cadmium concentration of 160 mg L⁻¹ in the root and 320 mg L⁻¹ in the shoot, especially. This result decreased almost to the control group expression level with the increase of the cadmium concentration. This also shows that; it is the ineffectiveness of the resistance mechanism against cadmium stress in both roots and shoots after the specified concentrations. It was determined that the GR pathway was inhibited due to possible cellular damage and it could not provide protection against cadmium stress by using the stress recovery pathway [7,31-34].

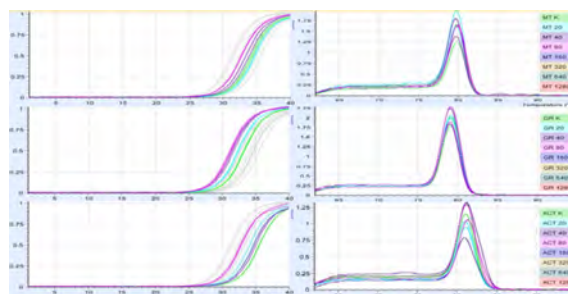


Figure 1. The quantification and melting curve analysis of the transcripts. The graphs on the left side shows transcript accumulation; right side shows the melting curve analysis of MT-2, GR-1 and Actin genes.

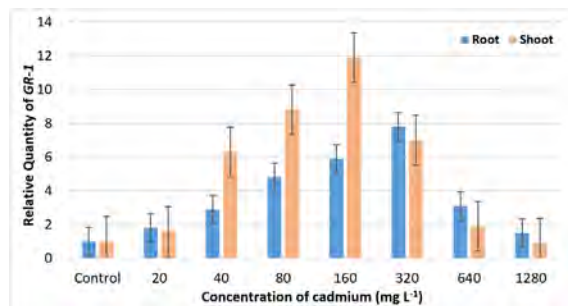


Figure 2. The changes in the expression levels of the Glutathione reductase-1 (GR-1) gene, depending on the concentration, in the root and shoot samples of tomato seedlings subjected to cadmium stress

On the other hand, metallothionein-2 (MT-2) gene expression data were examined, MT-2 results similar to GR-1 data were obtained. When the expression data of root and shoot samples of tomato seedlings under cadmium stress were evaluated; MT-2 gene expression level was found to be 3.4 and 4.4 fold in root samples at 80 and 160 mg L⁻¹ concentrations, respectively. After the concentration of 160 mg L⁻¹, there was a remarkable decrease in the expression of the MT-2 gene like GR-1. Similarly, 4.2 and 4.7 fold changes were detected in shoots at 80 and 160 mg L⁻¹ concentrations, respectively (Figure 3). It is cleared from the results obtained that the change in the expression of the metallothionein binding protein gene MT-2 can induce cadmium toxicity tolerance in tomato plant [7,29,32,33].

In addition support these results, the change in GR-1 and MT-2 expressions data in both root and shoot samples was found to be statistically significant ($P < 0.05$). Detailed

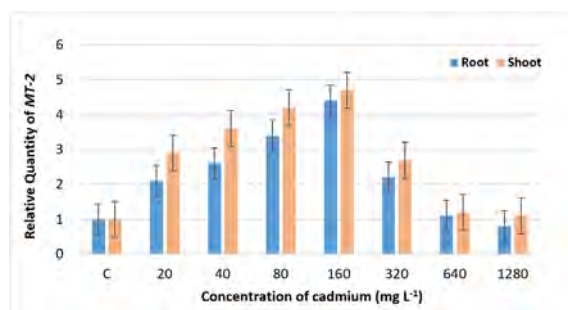


Figure 3. The changes in the expression levels of the metallothionein-2 (MT-2) gene, depending on the concentration, in the root and shoot samples of tomato seedlings subjected to cadmium stress

Table 3. Sequences and melting temperatures of primers used in qRT-PCR

	Genes	Concentrations						
		20 mg L ⁻¹	40 mg L ⁻¹	80 mg L ⁻¹	160 mg L ⁻¹	320 mg L ⁻¹	640 mg L ⁻¹	1280 mg L ⁻¹
root	GR-1	*	*	***	**	***	*	*
	MT-2	*	Ns	*	***	*	***	*
shoot	GR-1	*	*	**	**	*	*	*
	MT-2	*	*	**	*	*	Ns	*

* p<0,05, ** p<0,01, *** p<0,001, Ns: non significant

information on the statistical significance levels of GR-1 and MT-2 expressions data in root and shoot samples of tomato seedlings exposed to cadmium stress at different concentrations compared to the control group has been given in the Table 3.

The results obtained with the GR-1 and MT-2 genes and their activities in this current study support different studies in the literature [7-9,26,27,33]. Stress related genes such as GR-1 and MT-2 are used in different applications (especially phytoremediation) against various stress factors. It has been reported that the evaluation of the expression data of these genes is effective in determining the level of damage to the living thing by the pollution in question and determining the molecular biological limits of the defense mechanism [7,26,28-35]. According to Tombuloglu et al. (2012) the expression data of GR-1 and MT-2 genes, which are stress-related genes due to boron stress, were examined in tomato seedlings. While gene expression increased due to increasing concentration, a decrease was observed after certain concentrations [27]. Also, in our previous study (2019), tomato seedlings were exposed to varying concentrations of zinc heavy metal stress and the expression levels of the same genes were investigated. Although similar results were obtained, its toxic effect was revealed at higher concentrations (eg: 320 mg L⁻¹ - 640 mg L⁻¹) than cadmium toxicity, since zinc is a microelement. After these concentrations, sudden decreases were observed in the same way. The results of the present study also support these [7]. Finally, Wang et al., (2018) cloning and characterization of the glutathione reductase gene and Rono et al. (2021) showed that metallothionein-like gene groups were identified for cadmium detoxification and potential phytoremediation. Thus, it has been shown that there are different and new stress-related genes or clones as GR-1 and MT-2 [31,33].

CONCLUSIONS

In the present study, it was shown that the activation of MT-2 and GR-1 like protein transcripts under cadmium stress. These genes expression increased at first and then, the expression curve was showed a descending profile

due to inhibition of stress mechanisms which regulates the cellular homeostasis under high cadmium level. Due to the increased concentration of cadmium heavy metal, the change of these genes, which are known to be stress-related in plants, such as tomato, has shown that these genes play an important role in the mechanism of protection against heavy metal stress. Also, this study results have indicated that tomato has physiological traits associated with accumulation of cadmium. The early molecular response of hydroponically cultivated tomato plants might develop different strategies to cope with Cd toxicity by manipulating the expression level of stress-related genes. Furthermore, these results showed that the resistance mechanism could not cope with cadmium stress and toxicity due to possible cellular damage using the GR pathway. Finally, the data obtained from the study; showed that the change in the expression levels of these genes in the tomato plant could serve as an additional Cd-tolerance mechanism to deal with the toxic effect of cadmium.

ACKNOWLEDGEMENTS

The author gratefully acknowledge the financial support of this work by Amasya University Scientific Research Unit (FMB-BAP 20-0480). And also, the author acknowledges to Prof. Dr. Emine Sumer ARAS at Ankara University, Science Faculty, and Department of Biology for her valuable support.

CONFLICTS OF INTEREST

Author had no any financial or personal relationships with other individuals or organizations that might inappropriately influence this work during the submission process.

STATEMENT OF ETHICS

There is no need for an ethics committee decision for the studies in the article.

References

1. Peralta I, Spooner D. History, origin and early cultivation of tomato (*Solanaceae*) (2006).
2. FAO. Food and agriculture organization of The United Nations Rome (2019) ISBN 978-92-5-106215-9.
3. Hall JL. Cellular mechanisms for heavy metal detoxification and tolerance. *Journal of Experimental Botany* 53 (2002) 1-11.
4. Alirzayeva EG, Shirvani TS, Yazici MA, Alverdiyeva S, Shukurov ES, Ozturk L, Ali-Zade VM, Cakmak I. Heavy metal accumulation in *Artemisia* and foliaceous lichen species from the Azerbaijan flora. *Forest Snow and Landscape Research* 80 (2006) 339-348.
5. Miwa K, Kamiya T, Fujiwara T. Homeostasis of the structurally important micronutrients, B and Si. *Current Opinion in Plant Biology* 12 (2009) 307-311.
6. Kirbag F, Munzuroglu O. Toxic effects of cadmium (Cd^{2+}) on metabolism of sunflower (*Helianthus annuus* L.) seedlings. *Acta. Agriculture. Scand, Section B-Soil and Plant Science* 56 (2006) 224-229.
7. Bolukbasi E and Karakas M. Effect of zinc heavy metal on stress-related genes in tomato (*Solanum lycopersicum* L.) plants. *International Journal of Environment Agriculture and Biotechnology* 4 (2019) 1211-1216.
8. Cervilla LM, Blasco B, Rios J, Romero L, Ruiz J. Oxidative stress and antioxidants in tomato (*Solanum lycopersicum* L.) plants subjected to boron toxicity. *Annual Botany* 100 (2007) 747-756.
9. Chalapathi R, Reddy AR. Glutathione reductase: a putative redox regulatory system in plant cells. In: Khan, N.A. et al. (Eds.), *Sulfur assimilation and abiotic stress in plants*. Springer-Verlag, Berlin, Heidelberg (2008) 111-147.
10. Temel Y, Taysi MS. The Effect of Mercury Chloride and Boric Acid on Rat Erythrocyte Enzymes. *Biological Trace Element Research* 191 (2019) 177-182.
11. Temel Y, Kufrevioglu OI, Ciftci M. Investigation of the effects of purification and characterization of Turkey (*Meleagris gallopavo*) liver mitochondrial thioredoxin reductase enzyme and some metal ions on enzyme activity. *Turkish Journal of Chemistry* 41 (2017) 48-60.
12. Chomczynski P, Mackey K. Short technical reports. Modification of the TRI reagent procedure for isolation of RNA from polysaccharide- and proteoglycan-rich sources. *Biotechniques* 19 (1995) 942-945.
13. Conte C, Mutti I, Puglisi P, Ferrarini A, Regina GRG, Maestri E, Marmiroli N. DNA fingerprint analysis by PCR based method for monitoring the genotoxic effects of heavy metals pollution. *Chemosphere* 37 (1998) 2739-2749.
14. Temel Y, Bengu AS, Akkoyun HT, Akkoyun M, Ciftci M. Effect of astaxanthin and aluminum chloride on erythrocyte G6PD and 6PGD enzyme activities in vivo and on erythrocyte G6PD in vitro in rats. *Journal of biochemical and molecular toxicology*, 31 (2017) 1-5.
15. Del Razo LM, Quintanilla-Vega B, Brambila-Colombres E, Caldero' n-Aranda ES, Manno M, Albores A. Stress proteins induced by arsenic. *Toxicology and Applied Pharmacology* 177 (2001) 132-148.
16. Apel K, Hirt H. Reactive oxygen species: metabolism oxidative stress, and signal transduction. *Annual Review of Plant Biology* 55 (2004) 373-399.
17. DalCorso G, Farinati S, Maistri S, Furini A. How plants cope with cadmium: staking all on metabolism and gene expression. *Journal of International Plant Biology* 50 (2008) 1268-1280.
18. Waisberg MP, Joseph B, Beyersmann D. Molecular and cellular mechanisms of cadmium carcinogenesis. *Toxicology* 192 (2003) 95-117.
19. Liu W, Yang YS, Zhou QX, Xie LJ, Li PJ, Sun TH. Impact assessment of cadmium contamination on rice (*Oryza sativa* L.) seedlings at molecular and population levels using multiple biomarkers. *Chemosphere* 67 (2007) 1155-1163.
20. Mirouze M, Paszkowski J. Epigenetic contribution to stress adaptation in plants. *Current Opinion in Plant Biology* 14 (2011) 267-274.
21. Bolukbasi E, Aras ES. Determination of DNA methylation levels with CRED-RA technique in the genome of sunflower seedlings (*Helianthus annuus* L.) subjected to zinc stress. *International Journal of Environment, Agriculture and Biotechnology* 3 (2016) 438-444.
22. Goupila P, Souguira D, Ferjanib E, Faurec O, Hitmid A, Ledoigta G. Expression of stress-related genes in tomato plants exposed to arsenic and chromium in nutrient solution. *Journal of Plant Physiology* 166 (2009) 1446-1452.
23. Gill SS, Tuteja N. Reactive oxygen species and antioxidant machinery in abiotic stress tolerance in crop plants. *Plant Physiology and Biochemistry* 48 (2010) 909-930.
24. Gebretsadkan G. Evaluating the effect of integrated use of farm yard manure and urea on the socio-economic performance of tomato (*Lycopersicon esculentum* Mill) at Tselemti Woreda, North western Tigray, Ethiopia. *International Journal of Environment, Agriculture and Biotechnology* 3 (2018) 748-755.
25. Kosnett MJ. Heavy metal intoxication and chelators. In: katzung BG(ed) *Basic and clinical pharmacology*. 10th edn. McGraw-Hill, New York (2007) 945-957.
26. Wang L, Yang L, Yang F, Li X, Song Y, Wang X, Hu X. Involvements of H_2O_2 and metallothionein in NO-mediated tomato tolerance to copper toxicity. *The Journal of Plant Physiology* 167 (2010) 1298-1306.
27. Tombuloglu H, Semizoglu N, Sakcali S, Kecec G. Boron induced expression of some stress-related genes in tomato. *Chemosphere* 86 (2012) 433-438.
28. Temel Y, Taher SSM, Hamza MA, Shafeeq IH, Kocyigit UM, Ciftci M. Investigation of the inhibition effects of some metal ions on glutathione reductase enzyme from japanese quail (*Coturnix coturnix japonica*) liver. *Cumhuriyet Science Journal* 39 (2018) 679-687.
29. Ziller A, Fraissinet-Tachet L. Metallothionein diversity and distribution in the tree of life: a multifunctional protein. *Metallomics* 10 (2018) 1549-1559.
30. Temel Y, Bozkus T, Ciftci M. Glutasyon redüktaz (GR) enziminin japon bildircin (*Coturnix coturnix japonica*) eritrositlerinden saflaştırılması ve karakterizasyonu. *Journal of the Institute of Science and Technology* 7 (2017) 143-150.
31. Rono JK, Le Wang L, Wu XC, Cao HW, Zhao YN. Identification of a new function of metallothionein-like gene OsMT1e for cadmium detoxification and potential phytoremediation. *Chemosphere* 265 (2021) 129-136.
32. Bolukbasi E, Aras ES. Determination of physiological biochemical and molecular effects of zinc stress on the growth of sunflower seedlings (*Helianthus annuus* L.). *International Journal of Environment, Agriculture and Biotechnology* 3 (2018) 530-536.
33. Wang Q, Pu Y, Yang D, Yin X, He Z. Molecular cloning and characterization of the glutathione reductase gene from *Stipa purpurea*. *Biochemical and Biophysical Research Communications* 495 (2018) 1851-1857.
34. Creissen GP, Edwards EA, Mullineaux PM. Glutathione reductase and ascorbate peroxidase. In *Causes of photooxidative stress and amelioration of defense systems in plants* CRC press (2019) 343-364.

35. Hasanuzzaman M, Bhuyan MHM, Anee TI, Parvin K, Nahar K. Regulation of ascorbate-glutathione pathway in mitigating oxidative damage in plants under abiotic stress. *Antioxidants* 8 (2019) 380-384.
36. Rozen S, Skaletsky H. Primer-3 on the www for general users and for biologist programmers. *Methods in Molecular Biology* 132 (2000) 365-386.
37. Livak KJ, Schmittgen TD. Analysis of relative gene expression data using real-time quantitative PCR and the $2^{-\Delta\Delta CT}$ method. *Methods* 25 (2001) 402-408.

Foam-mat Drying of Carrot Juice and Thin Layer Modeling of Drying

Hulya Cakmak¹  Vasfiye Hazal Ozyurt² 

¹Hitit University, Department of Food Engineering, Corum, Turkey

²Mugla Sitki Kocman University, Department of Gastronomy and Culinary Arts, Mugla, Turkey

ABSTRACT

Drying of fruit and vegetables is critical step of processing which can be very destructive for nutrients and especially for bioactive compounds. However, novel drying methods like foam-mat drying helps to decrease the drying period and exposure to drying air therefore protect the bioactives against thermal degradation as well as improving final powder quality. The foam-mat drying of carrot juice and modeling of experimental drying data with the theoretical models has not yet been studied in the literature. In this study, the effects of foam-mat drying at 50, 60 and 70°C on the drying behavior of carrot juice with the addition of 15% egg albumen (EA) and 15% egg albumen+ 10% whey protein isolate (WPI) as foaming agents and thin-layer modeling of the foams at different thicknesses were evaluated. Compared to the control sample (only carrot juice), the drying time of the foamed carrot juice was reduced by 25% to 60% depending on the foam thickness and drying temperature. These results were consistent with the effective diffusion coefficients (D_{eff}), since the control sample had comparably low D_{eff} value than the 15% EA and 15% EA+10% WPI foams. Among the fitted mathematical models, Midilli *et al.* had better prediction capacity with the highest adjusted correlation coefficients, in addition to the lowest sum of squared error and root mean square error values for every formulation, foam thicknesses and drying temperatures compared to other theoretical models.

Keywords:

Carrot juice; Foam-mat drying; Modeling; Thin-layer

INTRODUCTION

Fresh fruits and vegetables are highly perishable because of their high moisture content and should be consumed without any deterioration if only stored properly or food preservation methods such as; freezing, canning, chemical treatments, or drying are employed for increasing their shelf life [1].

Drying is one of the oldest food preservation methods used because it increases the shelf-life of foodstuffs by reducing the water activity, therefore the dried products can be stored for later use. Besides, microbial activity that is causing the spoilage of the food is prevented, and at the same time, most of enzymes that is evoking chemical changes in the food cannot perform their functions due to moisture removal. Thus, dried foods can be stored for a longer period [2].

Drying methods using hot air with natural or forced convection are mostly preferred for drying foods. However, since the chosen method is effective on the

quality characteristics of the final product, drying methods such as; contact drying [3], convective drying [4], radiation drying [5], freeze-drying [6], osmotic drying [7] are used for drying of agricultural products like; vegetables, fruits, and cereals. Alternative drying methods are constantly being developed, since the quality of the final product is important. Foam-mat drying is a novel technique developed to increase the moisture transfer during the drying of liquid and semi-liquid foods. The foam-mat drying process, which is carried out by the addition of foaming agents and stabilizers, has come to the forefront due to its advantages such as shortening the drying time with hot air, and better preservation of the dried food quality, and many studies have been carried out on foam drying [8]. The drying of agricultural products using foam drying methods has been studied by many researchers. In these studies, vegetable and fruits such as; instant yam (*Dioscorea rotundata*) [9], banana [10], tomato pulp [11], blackcurrant pulp [12], papaya nectar [13], mango [14], muskmelon [15], yacon juice [16]

Article History:

Received: 2021/11/16

Accepted: 2021/12/22

Online: 2021/12/31

Correspondence to: Hulya Cakmak,
Hitit University, Food Engineering, 19030,
Corum, TURKEY
E-Mail: hulyacakmak@hitit.edu.tr
Phone: +90 364 227 45 36
Fax: +90 364 227 45 35

and crab apple juice [8] were dried by this method. Although there are a few studies about carrot powder production with foam-mat drying by incorporation of some other foaming agents like Tween 80, methylcellulose and egg white, these studies mostly focused on chemical composition of the powders or powder yield [17, 18]. Moreover, the foam-mat drying of carrot juice including different animal-based protein sources as foaming agents and the mathematical modeling of drying has not been studied yet. Therefore, the objective of this study was to determine the drying behavior of carrot juice by foam-mat drying method and mathematical modeling of the experimental drying data by exploring the presence of egg albumen (EA) and egg albumen + whey protein isolate (WPI) in the formulation together with the foam thickness at different drying temperatures.

MATERIALS AND METHODS

Fresh carrots and whole eggs were purchased from a local supermarket in Corum, Turkey. Whey protein isolate with 96% protein was supplied from local distributor of Hipro Iso whey (Bionet Tic. A.S., Istanbul).

Fresh carrot juice was extracted according to the previous study of Cakmak and Ozyurt [19]. The extracted juice were filled into the glass bottles and heat-treated at 95°C for 5 min [20] in a water bath (Wise Bath, WB22, Daihan Scientific, South Korea), and cooled to 4°C.

Production of Carrot Juice Foams

The most stable foam structure was obtained from the 15% EA+ 10% WPI foam formulation according to the previous study of the authors which was mixed at the highest speed with a hand-blender (Arzum Pasto AR-183, Turkey) for 8 min whipping time. In addition to this formulation, 15% EA including foams were prepared similarly to the given foaming conditions.

Thin Layer Drying of Carrot Juice Foams

15% EA and 15% EA+ 10% WPI foams together with control (carrot juice without foaming) were spread evenly on petri dishes (OD: 90 mm) at two different thicknesses, in order to equilibrate the mass on each petri dishes. For control, the samples were placed with the thickness of 2.5 and 3.2 mm, whereas 15% EA and 15% EA+ 10% WPI including foams the thickness was arranged as 5 and 6 mm. The samples were dried at 50, 60 and 70°C in a preheated built-in oven (Model no: NV60K7140BB, Samsung, Turkey) with upper-lower heating function at 0.9 m/s steady air velocity until constant weight was observed. Drying experiments performed at least five parallels and the mass of petri dishes were recorded with an analytical ba-

Table 1. Thin layer models fitted to experimental drying datas.

Model	Model eq.	Reference
Lewis	$MR = e^{(-kt)}$	[8], [21]
Page	$MR = e^{(-kt^n)}$	[8], [21]
Henderson & Pabis	$MR = ae^{(-kt)}$	[8], [21]
Logarithmic	$MR = ae^{(-kt)} + c$	[8], [21]
Two-term	$MR = ae^{(-k_1t)} + be^{(-k_2t)}$	[8], [21]
Midilli et al.	$MR = ae^{(-kt^n)} + bt$	[8], [21]
Modified Midilli et al.	$MR = e^{(-kt^n)} + bt$	[8], [21]

lance (Precisa Gravimetrics, XB220A, Switzerland) every 10 min for first half hour, and every 30 min until the constant weight was observed. The drying curves of the samples were obtained from the plot of drying rate (kg water/ hm²) versus free moisture content (kg water/ kg dry solid) with respect to the removed free water during aforementioned time intervals at constant surface area exposed during drying.

Mathematical Modeling of Foam-mat Drying

Fick's second law of diffusion was employed for evaluation of the moisture transfer from the control and carrot juice foam samples. The diffusion equation for an infinite slab at falling rate drying period is given in Eq.1;

$$MR = \frac{M - M_e}{M_0 - M_e} = \frac{8}{\pi^2} \sum_{n=0}^{\infty} \frac{1}{(2n+1)^2} \exp\left[-(2n+1)^2 \frac{\pi^2 D_{eff} t}{L^2}\right] \quad (1)$$

here MR shows the dimensionless moisture ratio, M_0 is initial moisture and M_e is the equilibrium moisture content. M represents the moisture at any time t , L is the thickness of the slab in m, and D_{eff} represents effective diffusion coefficient (m²/s).

The experimental drying data of the control and carrot juice foams were fitted to the thin layer models given in Table 1 by using Matlab R2016A (MathWorks Inc., USA). The goodness of model fit was evaluated with respect to the Adj-R² (adjusted correlation coefficient), SSE (sum of squared error) and RMSE (root mean square error) values.

RESULTS AND DISCUSSION

The drying rate curves of the samples are shown Fig. 1a, 1b and 1c for drying at 50, 60 and 70°C together with the lowest foam thicknesses (for control: 2.5 mm, for 15% EA and 15% EA + 10% WPI: 5 mm), respectively. It is seen that the control sample and 15% EA foam had both constant and falling rate period at all drying temperatures. In addition, it was observed that the 15% EA + 10% WPI

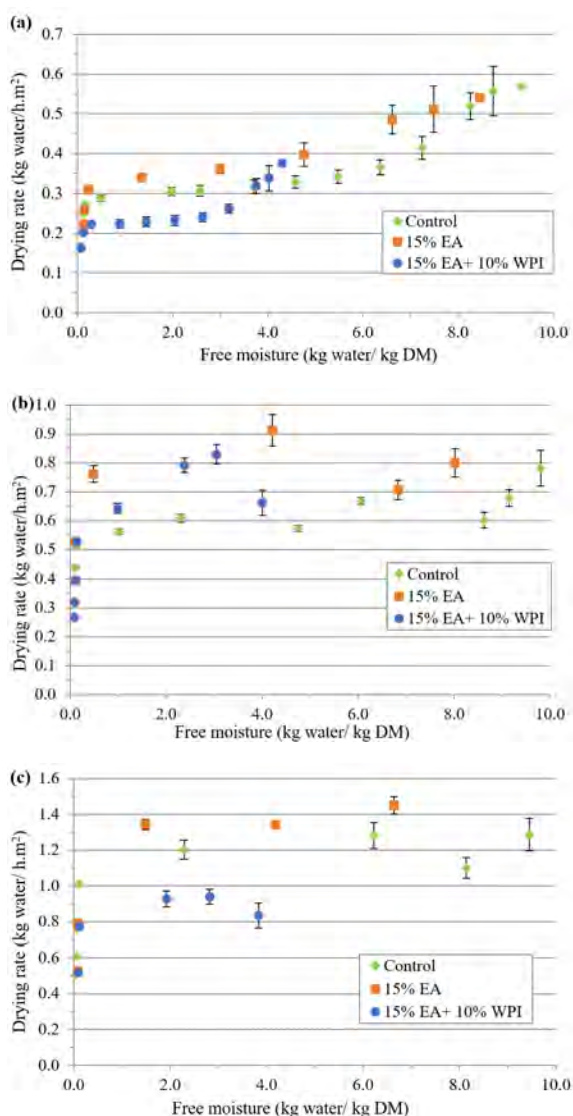


Figure 1. Drying rate curves of carrot juice (control), 15% EA and 15%EA+ 10% WPI foams at (a) 50°C, (b) 60°C and (c) 70°C, respectively.

sample had both constant and falling rate period only at 50°C, and only falling rate period at 60 and 70°C. Besides, the increase in drying temperature increased the drying rate by accelerating the moisture transfer at the elevated temperatures. The initial moisture content of control sample was reduced from 9.965 kg water/ kg DM to 0.125 kg water/ kg DM at 50°C, to 0.111 kg water/ kg DM at 60°C and to 0.047 kg water/ kg DM at 70°C for 2.5 mm thickness. Besides, the initial moisture content of 15% EA foam was reduced from 9.542 kg water/ kg DM to 0.151 kg water/ kg DM, 0.105 kg water/ kg DM, 0.078 kg water/ kg DM for drying at 50, 60 and 70°C, respectively.

Drying period of the samples reaching the constant weight was found dependent on the drying temperature. For 50°C, the drying period was observed between 360-480 min for control sample, whereas it was between 210-240 min for

15% EA foam and between 240-270 min for 15% EA+ 10% WPI at both thicknesses. Similarly, the drying period at 70°C lasted 150 min for the control sample; while the drying period of 15% EA sample was 90 min and 60 min for the 15% EA + 10% WPI sample at both thicknesses. As can be seen from these observations, the foam-mat drying method shortened the drying time by 25-60% depending on the drying temperature and the foam thickness (amount).

The effective diffusion coefficients are influenced by the drying temperature, although the foam viscosity may hinder the moisture transfer [22]. The D_{eff} of the control sample was found between 9.403×10^{-9} - 9.803×10^{-8} m²/s, for 15% EA it was between 1.421 - 6.262×10^{-7} m²/s and for 15% EA+ 10% WPI foam it was between 5.499×10^{-8} - 5.990×10^{-7} m²/s, respectively. In accordance with the drying period values, foam-mat drying improved the moisture diffusion compared to control sample due to increased water-air interface area due to foaming [8, 22, 23].

The results of regression analysis employed for finding the best thin layer model representing the foam-mat drying of carrot juice foams are given in Table 2, 3 and 4. The Adj-R² values of the tested mathematical models were found between 0.93-0.99 and very successful in terms of representing the experimental drying data of carrot juice and foams at any drying temperature and foam thickness. But the most successful model was determined as Midilli *et al.* with the highest Adj-R² together with the lowest SSE and RMSE values. The model constants of Midilli *et al.* model are also shown in Table 5.

Foam-mat drying offers several advantages like increasing the moisture transfer rate by increasing the air-water interface due to volume expansion via foaming. Thus, this method decreases the energy consumption, improves re-constitution capacities of produced powders thus product quality, as well as protecting the bioactive compounds against thermal degradation compared to the conventional drying methods by encapsulation like mechanism of the proteins [8], [24], [25], [26].

Similar to the present study, the foam-mat drying reduced the drying period of apple juice [24], mango puree [23], crab apple juice [8] and date puree [27].

The effective diffusion coefficients can be affected from the foam formulation and the drying temperature [23], and increasing the drying temperature increases the D_{eff} values because of faster moisture transfer from the material [26]. Chaux-Gutiérrez *et al.* [23] stated in their study that the D_{eff} values of foam-mat drying of mango pulp was found between 2.15 - 6.12×10^{-10} m²/s, whereas the D_{eff} values of lime juice foams 8.980×10^{-9} and 1.138×10^{-8} m²/s [22]. These values are in accordance with the D_{eff} values of carrot juice foams.

Table 2. Statistical results of tested models for drying at 50°C.

Sample- thickness	Model	Adj-R ²	SSE	RMSE
Control-2.5 mm	Lewis	0.9657	0.05653	0.06595
	Page	0.9794	0.03130	0.05107
	Henderson & Pabis	0.9642	0.05438	0.06732
	Logarithmic	0.9642	0.05438	0.06732
	Two-term	0.9570	0.05442	0.07377
	Midilli et al.	0.9846	0.02147	0.04418
	Modified Midilli et al.	0.9794	0.03130	0.05107
Control-3.2 mm	Lewis	0.9427	0.09119	0.08071
	Page	0.9692	0.04551	0.05916
	Henderson & Pabis	0.9421	0.08560	0.08115
	Logarithmic	0.9421	0.08560	0.08115
	Two-term	0.9316	0.08561	0.08822
	Midilli et al.	0.9819	0.02672	0.04534
	Modified Midilli et al.	0.9735	0.03917	0.05489
15% EA-5 mm	Lewis	0.9781	0.03021	0.05793
	Page	0.9888	0.01378	0.04150
	Henderson & Pabis	0.9780	0.02699	0.05808
	Logarithmic	0.9780	0.02699	0.05810
	Two-term	0.9706	0.02699	0.06707
	Midilli et al.	0.9888	0.01204	0.04147
	Modified Midilli et al.	0.9888	0.01378	0.04150
15% EA - 6 mm	Lewis	0.9781	0.03021	0.05790
	Page	0.9872	0.01564	0.04421
	Henderson & Pabis	0.9709	0.03570	0.06680
	Logarithmic	0.9780	0.02699	0.05808
	Two-term	0.9706	0.02699	0.06707
	Midilli et al.	0.9888	0.01204	0.04147
	Modified Midilli et al.	0.9888	0.01378	0.04150
15% EA + 10% WPI-5 mm	Lewis	0.9734	0.03667	0.06383
	Page	0.9888	0.01378	0.04150
	Henderson & Pabis	0.9717	0.03467	0.06583
	Logarithmic	0.9709	0.03570	0.06680
	Two-term	0.9706	0.02700	0.06709
	Midilli et al.	0.9888	0.01204	0.04147
	Modified Midilli et al.	0.9888	0.01378	0.04150
15% EA + 10% WPI-6 mm	Lewis	0.9737	0.03629	0.06350
	Page	0.9861	0.01704	0.04615
	Henderson & Pabis	0.9717	0.03467	0.06583
	Logarithmic	0.9734	0.03264	0.06387
	Two-term	0.9706	0.02699	0.06707
	Midilli et al.	0.9888	0.01204	0.04147
	Modified Midilli et al.	0.9888	0.01378	0.04150

Table 3. Statistical results of tested models for drying at 60°C.

Sample- thickness	Model	Adj-R ²	SSE	RMSE
Control-2.5 mm	Lewis	0.9583	0.05841	0.08056
	Page	0.9877	0.01534	0.04379
	Henderson & Pabis	0.9611	0.04850	0.07786
	Logarithmic	0.9611	0.04850	0.07786
	Two-term	0.9481	0.04850	0.08991
	Midilli et al.	0.9892	0.01183	0.04111
	Modified Midilli et al.	0.9877	0.01534	0.04379
Control-3.2 mm	Lewis	0.9476	0.08417	0.09174
	Page	0.9873	0.01834	0.04514
	Henderson & Pabis	0.9519	0.06954	0.08790
	Logarithmic	0.9519	0.06954	0.08790
	Two-term	0.9381	0.06955	0.09968
	Midilli et al.	0.9900	0.01279	0.03998
	Modified Midilli et al.	0.9873	0.01834	0.04514
15% EA-5 mm	Lewis	0.9516	0.05243	0.09347
	Page	0.9940	0.00498	0.03304
	Henderson & Pabis	0.9506	0.04465	0.09450
	Logarithmic	0.9438	0.05079	0.10080
	Two-term	0.9176	0.04465	0.12200
	Midilli et al.	0.9945	0.00437	0.03154
	Modified Midilli et al.	0.9945	0.00498	0.03154
15% EA - 6 mm	Lewis	0.9671	0.04077	0.07630
	Page	0.9981	0.00203	0.01840
	Henderson & Pabis	0.9616	0.04075	0.08241
	Logarithmic	0.9786	0.02272	0.06154
	Two-term	0.9711	0.03065	0.07150
	Midilli et al.	0.9983	0.00176	0.01717
	Modified Midilli et al.	0.9983	0.00177	0.01877
15% EA + 10% WPI-5 mm	Lewis	0.9806	0.02246	0.05664
	Page	0.9974	0.00260	0.02195
	Henderson & Pabis	0.9879	0.01200	0.04472
	Logarithmic	0.9860	0.01387	0.04809
	Two-term	0.9663	0.02231	0.07468
	Midilli et al.	0.9974	0.00241	0.02082
	Modified Midilli et al.	0.9970	0.00296	0.02219
15% EA + 10% WPI-6 mm	Lewis	0.9706	0.04013	0.07082
	Page	0.9973	0.00320	0.02153
	Henderson & Pabis	0.9726	0.03270	0.06835
	Logarithmic	0.9783	0.02589	0.06082
	Two-term	0.9697	0.02590	0.07197
	Midilli et al.	0.9975	0.00256	0.02071
	Modified Midilli et al.	0.9975	0.00300	0.02081

Table 4. Statistical results of tested models for drying at 70°C.

<i>Sample- thickness</i>	<i>Model</i>	<i>Adj-R²</i>	<i>SSE</i>	<i>RMSE</i>
<i>Control-2.5 mm</i>	<i>Lewis</i>	0.9660	0.04750	0.07705
	<i>Page</i>	0.9966	0.00421	0.02451
	<i>Henderson & Pabis</i>	0.9688	0.03815	0.07383
	<i>Logarithmic</i>	0.9688	0.03815	0.07383
	<i>Two-term</i>	0.9636	0.03815	0.07974
	<i>Midilli et al.</i>	0.9966	0.00365	0.02447
	<i>Modified Midilli et al.</i>	0.9966	0.00421	0.02451
<i>Control-3.2 mm</i>	<i>Lewis</i>	0.9556	0.06283	0.08862
	<i>Page</i>	0.9951	0.00609	0.02950
	<i>Henderson & Pabis</i>	0.9624	0.04648	0.08149
	<i>Logarithmic</i>	0.9624	0.04648	0.08149
	<i>Two-term</i>	0.9562	0.04648	0.08802
	<i>Midilli et al.</i>	0.9953	0.00503	0.02897
	<i>Modified Midilli et al.</i>	0.9951	0.00605	0.02940
<i>15% EA-5 mm</i>	<i>Lewis</i>	0.9720	0.02313	0.06802
	<i>Page</i>	0.9945	0.00365	0.03019
	<i>Henderson & Pabis</i>	0.9731	0.01782	0.06675
	<i>Logarithmic</i>	0.9731	0.01782	0.06675
	<i>Two-term</i>	0.9462	0.01782	0.09440
	<i>Midilli et al.</i>	0.9952	0.002371	0.02811
	<i>Modified Midilli et al.</i>	0.9950	0.003306	0.02875
<i>15% EA - 6 mm</i>	<i>Lewis</i>	0.9509	0.04271	0.09243
	<i>Page</i>	0.9905	0.00662	0.04067
	<i>Henderson & Pabis</i>	0.9385	0.04286	0.10350
	<i>Logarithmic</i>	0.9351	0.04523	0.10630
	<i>Two-term</i>	0.9457	0.03785	0.09727
	<i>Midilli et al.</i>	0.9915	0.00440	0.03840
	<i>Modified Midilli et al.</i>	0.9905	0.00662	0.04070
<i>15% EA + 10% WPI-5 mm</i>	<i>Lewis</i>	0.9491	0.04307	0.09357
	<i>Page</i>	0.9945	0.00377	0.03070
	<i>Henderson & Pabis</i>	0.9539	0.03171	0.08904
	<i>Logarithmic</i>	0.9438	0.03866	0.09831
	<i>Two-term</i>	0.9412	0.04044	0.10050
	<i>Midilli et al.</i>	0.9952	0.00330	0.02870
	<i>Modified Midilli et al.</i>	0.9947	0.00360	0.03010
<i>15% EA + 10% WPI-6 mm</i>	<i>Lewis</i>	0.9636	0.03122	0.07901
	<i>Page</i>	0.9963	0.00190	0.02506
	<i>Henderson & Pabis</i>	0.9539	0.03168	0.08900
	<i>Logarithmic</i>	0.9615	0.02644	0.08130
	<i>Two-term</i>	0.9505	0.03396	0.09214
	<i>Midilli et al.</i>	0.9966	0.00188	0.02400
	<i>Modified Midilli et al.</i>	0.9961	0.00270	0.02590

Table 5. Model constants of the best fitting theoretical model.

Temperature (°C)	Sample	Midilli <i>et al.</i> model constant
50	Control-2.5 mm	$a=0.932, b=2.338*10^{-14}, k=0.0003, n=1.556$
	Control-3.2 mm	$a=0.943, b=3.185*10^{-12}, k=0.0001, n=1.659$
60	Control-2.5 mm	$a=0.953, b=2.223*10^{-14}, k=0.0005, n=1.659$
	Control-3.2 mm	$a=0.947, b=4.233*10^{-10}, k=0.0002, n=1.859$
70	Control-2.5 mm	$a=0.978, b=1.943*10^{-12}, k=0.0021, n=1.626$
	Control-3.2 mm	$a=0.973, b=2.332*10^{-14}, k=0.0009, n=1.682$
50	15% EA-5 mm	$a=0.962, b=2.244*10^{-14}, k=0.0029, n=1.363$
	15% EA-6 mm	$a=0.962, b=2.309*10^{-14}, k=0.0028, n=1.363$
60	15% EA-5 mm	$a=0.977, b=1.189*10^{-9}, k=0.0014, n=1.874$
	15% EA-6 mm	$a=1.002, b=2.256*10^{-14}, k=0.0036, n=1.536$
70	15% EA-5 mm	$a=1.000, b=2.417*10^{-14}, k=0.0012, n=1.502$
	15% EA-6 mm	$a=0.999, b=4.348*10^{-14}, k=0.0006, n=2.203$
50	15% EA + 10% WPI-5 mm	$a=0.962, b=1.559*10^{-11}, k=0.0028, n=1.363$
	15% EA + 10% WPI-6 mm	$a=0.962, b=2.222*10^{-14}, k=0.0029, n=1.363$
60	15% EA + 10% WPI-5 mm	$a=0.999, b=2.245*10^{-14}, k=0.0069, n=1.354$
	15% EA + 10% WPI-6 mm	$a=0.994, b=2.221*10^{-14}, k=0.0036, n=1.444$
70	15% EA + 10% WPI-5 mm	$a=0.986, b=2.220*10^{-14}, k=0.0034, n=1.657$
	15% EA + 10% WPI-6 mm	$a=0.997, b=2.221*10^{-14}, k=0.0048, n=1.596$

Since carrot juice is a valuable source of carotenoids, the encapsulation of these bioactive compounds with wall materials including the proteins or stabilizers by foam-mat drying like this present study will promote longer stability of carotenoids [28]. Therefore, the efforts related with finding better drying conditions in terms of selecting different dryers such as non-thermal or hybrid dryers together with modifying the drying temperature and air velocity will help to provide an insight for further foam-mat drying of similar juices.

CONCLUSION

It has been determined that the foam-mat drying process shortens the drying time of carrot juice by 25-60% depending on the drying temperature and the foam thickness. These results in accordance with the effective diffusion coefficients, since the drying of foamed juices had higher D_{eff} values compared to the control sample.

Consequently, the compatibility of experimental drying data of carrot juice with the tested theoretical models was evaluated, and the adjusted correlation coefficients of the tested theoretical models varied between 0.93-0.99, which showed that the fitted models had a high ability to represent the drying behavior of the carrot juice, 15% EA and 15% EA+ 10% WPI foams. However, among these mo-

dels, regardless of the foam composition, drying temperature, or foam thicknesses, the best results were found with the Midilli *et al.* model. Future studies may focus on prediction of the drying data of different fruit juice foams by the same theoretical model.

ACKNOWLEDGEMENT

This work was supported by the Hitit University Scientific Research Commission through a research Grant No. MUH19001.18.002.

CONFLICT OF INTEREST

The authors declare that there is no conflict of interest.

AUTHOR CONTRIBUTION

Hülya Çakmak: Funding acquisition, Formal analysis, Investigation, Conceptualization, Methodology, Writing - original draft, Writing - review & editing. V. Hazal Özyurt: Formal analysis, Conceptualization, Investigation, Methodology, Writing - original draft, Writing - review & editing. Both authors read and approved the final manuscript.

References

1. Amit SK, Uddin MM, Rahman R, Islam SR, Khan MS. A review on mechanisms and commercial aspects of food preservation and processing. *Agriculture & Food Security* 6(1) (2017) 1-22.
2. Kumar C, Karim MA, Joardder MU. Intermittent drying of food products: A critical review. *Journal of Food Engineering* 121 (2014) 48-57.
3. Nindo CI, Tang J. Refractance window dehydration technology: a novel contact drying method. *Drying Technology* 25(1) (2007) 37-48.
4. Castro AM, Mayorga, EY, Moreno FL. Mathematical modelling of convective drying of fruits: A review. *Journal of Food Engineering* 223 (2018) 152-167.
5. Nathakaranakule A, Jaiboon P, Soponronnarit S. Far-infrared radiation assisted drying of longan fruit. *Journal of Food Engineering* 100(4) (2010) 662-668.
6. Duan X, Yang X, Ren G, Pang Y, Liu L, Liu Y. Technical aspects in freeze-drying of foods. *Drying Technology* 34(11) (2016) 1271-1285.
7. Pan YK, Zhao LJ, Zhang Y, Chen G, Mujumdar AS. Osmotic dehydration pretreatment in drying of fruits and vegetables. *Drying Technology* 21(6) (2003) 1101-1114.
8. Cakmak H. Evaluation of foam-mat drying behaviour of crab apple (*Malus floribunda*) fruit juice and powder quality. *Gıda* 45(3) (2020) 530-543.
9. Falade KO, Onyeoziri NF. Effects of cultivar and drying method on color, pasting and sensory attributes of instant yam (*Dioscorea rotundata*) flours. *Food and Bioprocess Technology* 5(3) (2012) 879-87.
10. Thuwapanichayanan R, Prachayawarakorn S, Soponronnarit S. Drying characteristics and quality of banana foam mat. *Journal of Food Engineering* 86(4) (2008) 573-583.
11. De Barros Fernandes RV, Queiroz F, Botrel DA, Rocha VV, Lima CF, Souza VR. Foam mat drying of tomato pulp. *Bioscience Journal Uberlandia* 29(4) (2013) 816-825.
12. Zheng XZ, Liu CH, Zhou H. Optimization of parameters for microwave-assisted foam mat drying of blackcurrant pulp. *Drying Technology* 29(2) (2011) 230-238.
13. Ibdapo OP, Erukainure OL. Quality characteristics of foam mat dried papaya (Homestead var.) nectar. *International Journal of Food Nutrition and Safety* 1(3) (2012) 127-136.
14. Kadam DM, Wilson RA, Chanha S, Grewal MK, Sharma M. Evaluation of physical and chemical properties of foam-mat dried mango (*Mangifera indica*) powder during storage. *Journal of Food Processing Preservation* 38 (2014) 1866-1874.
15. Asokapandian S, Venkatachalam S, Swamy GJ, Kuppasamy K. Optimization of foaming properties and foam mat drying of muskmelon using soy protein. *Journal of Food Process Engineering* 39(6) (2016) 692-701.
16. Franco TS, Perussello CA, Ellenderse LN, Masson ML. Effects of foam mat drying on physicochemical and microstructural properties of yacon juice powder. *LWT-Food Science Technology* 66 (2016) 503-513.
17. Kartini K, Krisnawan AH, Silvanus LC, Wijaya TP. Formulation of functional beverages from the combination of lime, tomato, and carrot using foam-mat drying method. *Pharmaciana* 9(2) (2019) 335-344.
18. Fardiyah Q, Rumhayati B, Khotimah YH. The effect of temperature and concentration of foaming agent to the β -carotene content in product derived from carrots. In IOP conference series: Materials Science and Engineering 299(1) (2018) 012008. IOP Publishing.
19. Cakmak H, Ozyurt VH. Foam stability of cloudy carrot juice: Effects of protein sources and foaming conditions. *The Annals of the University of Dunarea de Jos of Galati. Fascicle VI. Food Technology* 45(1) (2021) 38-51.
20. Demir N, Bahçeci KS, Acar J. The effect of processing method on the characteristics of carrot juice. *Journal of Food Quality* 30(5) (2007) 813-822.
21. Kucuk H, Midilli A, Kilic A, Dincer I. A review on thin-layer drying-curve equations. *Drying Technology*, 32(7) (2014) 757-773.
22. Dehghannya J, Pourahmad M, Ghanbarzadeh B, Ghaffari H. Influence of foam thickness on production of lime juice powder during foam-mat drying: experimental and numerical investigation. *Powder Technology* 328 (2018) 470-484.
23. Chaux-Gutiérrez AM, Santos AB, Granda-Restrepo DM, Mauro MA. Foam mat drying of mango: Effect of processing parameters on the drying kinetic and product quality. *Drying Technology* 35(5) (2017) 631-641.
24. Kudra T, Ratti C. Foam-mat drying: Energy and cost analyses. *Canadian Biosystems Engineering* 48(3) (2006) 27-32.
25. Hardy Z, Jideani VA. Foam-mat drying technology: A review. *Critical Reviews in Food Science and Nutrition* 57(12) (2017) 2560-2572.
26. Abbasi E, Azizpour M. Evaluation of physicochemical properties of foam mat dried sour cherry powder. *LWT-Food Science and Technology* 68 (2016) 105-110.
27. Seerangurayar T, Manickavasagan A, Al-Ismaili AM, Al-Mulla YA. Effect of carrier agents on flowability and microstructural properties of foam-mat freeze dried date powder. *Journal of Food Engineering* 215 (2017) 33-43.
28. Haas K, Dohnal T, Andreu P, Zehetner E, Kiesslich A, Volkert M, Fryer P, Jaeger H. Particle engineering for improved stability and handling properties of carrot concentrate powders using fluidized bed granulation and agglomeration. *Powder Technology* 370 (2020) 104-115.